

Multitaper Methods for Time-Frequency Spectrum Estimation and Unaliasing of Harmonic Frequencies

by

Azadeh Moghtaderi

A thesis submitted to the
Department of Mathematics and Statistics
in conformity with the requirements for
the degree of Doctor of Philosophy

Queen's University
Kingston, Ontario, Canada

January 2009

Copyright © Azadeh Moghtaderi, 2009

Abstract

This thesis is concerned with various aspects of stationary and nonstationary time series analysis. In the nonstationary case, we study estimation of the Wold-Cramér evolutionary spectrum, which is a time-dependent analogue of the spectrum of a stationary process. Existing estimators of the Wold-Cramér evolutionary spectrum suffer from several problems, including bias in boundary regions of the time-frequency plane, poor frequency resolution, and an inability to handle the presence of purely harmonic frequencies. We propose techniques to handle all three of these problems.

We propose a new estimator of the Wold-Cramér evolutionary spectrum (the BCMTFSE) which mitigates the first problem. Our estimator is based on an extrapolation of the Wold-Cramér evolutionary spectrum in time, using an estimate of its time derivative. We apply our estimator to a set of simulated nonstationary processes with known Wold-Cramér evolutionary spectra to demonstrate its performance.

We also propose an estimator of the Wold-Cramér evolutionary spectrum, valid for uniformly modulated processes (UMPs). This estimator mitigates the second problem, by exploiting the structure of UMPs to improve the frequency resolution of the BCMTFSE. We apply this estimator to a simulated UMP with known Wold-Cramér evolutionary spectrum.

To deal with the third problem, one can detect and remove purely harmonic frequencies before applying the BCMTFSE. Doing so requires a consideration of the aliasing problem. We propose a frequency-domain technique to detect and unalias aliased frequencies in bivariate time series, based on the observation that aliasing manifests as nonlinearity in the phase of the complex coherency between a stationary process and a time-delayed version of itself. To illustrate this “unaliasing” technique, we apply it to simulated data and a real-world example of solar noon flux data.

Acknowledgements

First and foremost, I would like to thank my supervisors Dr. Glen Takahara and Dr. David J. Thomson for their support, encouragement, and helpful advice during the completion of this thesis.

I would also like to thank the people who made my stay in Kingston enjoyable, in particular Amir, Bahman, Davood, Deb, Mohsen, Nazanin, Rebecca, Reza, Saeed, and Shahram.

Last but not least, I would like to thank Scott for all of his love, help and support, particularly during the completion of this thesis.

Statement of Originality

Except where precise references are provided, all results of this thesis are original.

Contents

Abstract	i
Acknowledgements	ii
Statement of Originality	iii
List of Tables	vii
List of Figures	viii
Chapter 1 Introduction	2
Chapter 2 Background and Literature Review	7
2.1 Time-Frequency Analysis	7
2.1.1 Short-Time Fourier Transforms and Spectrograms	8
2.1.2 Wigner-Ville Spectra	9
2.1.3 Evolutionary Spectra	10
2.1.4 Wold-Cramér Evolutionary Spectra	11
2.1.5 Harmonizable Processes and Loève Spectra	12
2.2 Aliasing	12
2.2.1 Change of Sampling Interval	14
2.2.2 Anti-Aliasing Filters	14
2.2.3 Unaliasing after Sampling	15

Chapter 3	Improved Time-Frequency Spectrum Estimation	16
3.1	Introduction	16
3.2	Evolutionary Spectra	18
3.2.1	Uniformly Modulated Processes	20
3.3	Wold-Cramér Evolutionary Spectra	21
3.4	High-Resolution Spectrograms	24
3.5	Nonstationary Quadratic-Inverse Theory	26
3.6	Sliding-Window High-Resolution Spectrograms	28
3.7	The Modified Time-Frequency Spectrum Estimator	29
3.7.1	Boundary Estimation of the Wold-Cramér Evolutionary Spectrum	32
3.8	Means and Variances of MTFSE and TDMTFSE	33
3.8.1	Expected Values of the MTFSE and TDMTFSE	33
3.8.2	Variances of the MTFSE and TDMTFSE	39
3.9	Simulated Processes	48
3.9.1	Example 1	48
3.9.2	Example 2	49
3.9.3	Example 3	54
3.9.4	Example 4	56
3.9.5	Comments on the Examples	61
3.10	Conclusion	61
Chapter 4	Diagnostic Plots for Uniformly Modulated Processes	63
4.1	Introduction	63
4.2	Diagnostic Plots for Detection of UMPs	64
4.3	Estimation of $\{C_t\}$ and $S_{\mathbf{Y}}$ using the Estimated TFS Matrix of a UMP	69
4.4	Frequency Resolution Improvement	71
4.5	Examples	72
4.5.1	Example 1	72

4.5.2	Example 2	77
4.5.3	Example 3	80
4.5.4	Example 4	82
4.5.5	Example 5	86
4.6	Conclusion	89
Chapter 5 Unfolding Aliases in Bivariate Time Series		90
5.1	Coherence, Time Delay, and Aliasing	92
5.2	Unaliasing Coherent Frequencies	101
5.3	Examples	109
5.3.1	Simulated Data Example	109
5.3.2	Solar Noon Flux Data	113
5.4	Conclusion	118
Chapter 6 Conclusion and Future Work		120
6.1	Conclusion	120
6.2	Future Work	121
6.2.1	Methodology	121
6.2.2	Data Analysis: Simulated and Real-World Data	122
Appendix A Prolate Spheroidal Wave Functions and Sequences		132
Appendix B Multiple-Window Spectrum Estimation		137
Appendix C Harmonic Analysis		141
Appendix D Coherence Analysis		147

List of Tables

5.1	True aliased frequencies and true phase calculation of complex coherency	111
5.2	Estimated unaliased frequencies for a simulated data.	112
5.3	Estimated unaliased frequencies for solar noon flux data.	117

List of Figures

3.1	Sequences A_l for $l \in \{0, 1, 2, 3\}$	27
3.2	Comparison of the HRS, SWHRS, BCMTFSE, and the time-frequency spectrum for Example 1.	50
3.3	Comparison of the HRS, SWHRS, BCMTFSE, and the time-frequency spectrum at $f = 0.0483$ for Example 1.	51
3.4	The time-frequency spectrum and the BCMTFSE for Example 1.	52
3.5	Comparison of the theoretical mean of the MTFSE, the BCMTFSE and the time-frequency spectrum for Example 1.	53
3.6	Comparison of the HRS, SWHRS, BCMTFSE, and the time-frequency spectrum at $f = 0.0483$ and $t = 300$ for Example 2.	54
3.7	The time-frequency spectrum and the BCMTFSE for Example 2.	55
3.8	Comparison of the HRS, SWHRS, BCMTFSE, and the time-frequency spectrum at $f = 0.0483$ and $t = 300$ for Example 3.	56
3.9	The time-frequency spectrum and the BCMTFSE for Example 3.	57
3.10	Comparison of the HRS, SWHRS, BCMTFSE, and the time-frequency spectrum at $f = 0.0483$ and $t = 300$ for Example 4.	59
3.11	The time-frequency spectrum and the BCMTFSE for Example 4.	60
4.1	Singular values of the theoretical TFS matrix for Example 1.	73
4.2	Singular values of the estimated TFS matrix for Example 1.	74
4.3	Singular values of the estimated LTFS matrix for Example 1.	75

4.4	The first left eigenvector of the estimated TFS matrix for Example 1.	76
4.5	Singular values of the theoretical TFS matrix for Example 2.	77
4.6	Singular values of the estimated TFS matrix for Example 2.	78
4.7	Singular values of the estimated LTFS matrix for Example 2.	78
4.8	The first left eigenvector of the estimated TFS matrix for Example 2.	79
4.9	Singular values of the theoretical TFS matrix for Example 3.	80
4.10	Singular values of the estimated TFS matrix for Example 3.	81
4.11	Singular values of the estimated LTFS matrix for Example 3.	81
4.12	The first left eigenvector of the estimated TFS matrix for Example 3.	82
4.13	Singular values of the theoretical TFS matrix for Example 4.	83
4.14	Singular values of the estimated TFS matrix for Example 4.	84
4.15	Singular values of the estimated LTFS matrix for Example 4.	84
4.16	The first and second left eigenvectors of the estimated TFS Matrix for Example 4.	85
4.17	Comparison of the BCMTFSE, ITFSE and the time-frequency spec- trum for Example 5.	88
5.1	Illustration of the folding process of the phase line	97
5.2	Illustration of the shifting process of the phase line and aliased pairs into a 360 degree phase band	100
5.3	Phase-frequency plot and folding of the phase line for the solar noon flux data from Learmonth and Sagamore Hill stations.	115

List of Acronyms

BCMTFSE Boundary-Corrected Modified Time-Frequency Spectrum Estimate

EP Evolutionary Periodogram

HRS High-Resolution Spectrogram

ITFSE Improved Time-Frequency Spectrum Estimator

LTFS Log Time-Frequency Spectrum matrix

MSC Magnitude-Squared Coherence

MTFSE Modified Time-Frequency Spectrum Estimator

NSQI Nonstationary Quadratic-Inverse

SNR Signal-to-Noise Ratio

SVD Singular Value Decomposition

SWHRS Sliding-Window High-Resolution Spectrogram

TDTFSE Time-Derivative of the Time-Frequency Spectrum Estimator

TFS Time-Frequency Spectrum matrix

UMP Uniformly Modulated Process

Chapter 1

Introduction

A common assumption in the spectral analysis of time series data is that a time series has been generated as a realization of a *stationary* process. Loosely speaking, a stationary process is one whose statistical properties are time-invariant. In particular, the first- and second-order statistics of a stationary process are time-invariant. However, many time series which are of important practical interest cannot be reasonably assumed to have been generated by a stationary process. For example, time series which appear in radar, sonar, speech, seismology, helioseismology, climatology, and geophysics are known to exhibit sudden and sporadic behaviour; this type of behaviour cannot reasonably be captured by stationary models. These kinds of processes (and indeed any processes which deviate from stationarity) are termed *nonstationary* processes. Briefly, a nonstationary process is one whose statistical properties change over time, *e.g.*, its mean, variance, covariance function, and higher-order moments may change as time evolves. Spectral analysis plays an important role in the analysis of stationary time series, particularly those arising in practical applications. This is largely due to the fact that the spectrum of a stationary process has a clear physical interpretation as a distribution of power over frequency. The theory of spectral analysis for stationary processes can be extended to nonstationary ones by “spectral”

descriptions of nonstationary processes which are typically functions of both time and frequency.

The problem of generalizing the notion of spectral analysis of stationary processes to nonstationary ones has been widely studied. However, in contrast to the stationary case, there is no natural notion of the “spectrum” of a nonstationary process. Several candidates have been proposed in the literature as nonstationary analogues of the stationary spectrum. One approach is to describe, in some sense, how the frequency content of a nonstationary process changes with time. This leads to the notion of *time-frequency spectra*. The most important time-frequency spectra, at least from our point of view, are the *Wigner-Ville spectrum* (see [Wigner 1932] or [Ville 1948]), the *evolutionary spectrum* [Priestley 1965] and the *Wold-Cramér evolutionary spectrum* (see [Mélard 1975] or [Tjøstheim 1976]). An alternative approach is to describe a nonstationary process by correlation between two distinct frequencies; this idea has led to the development of the dual-frequency spectrum (see [Loève 1946]).

Estimators for the above time-frequency spectra are summarized as follows. The *Wigner-Ville distribution* is an estimator of the Wigner-Ville spectrum [Flandrin 1999]. The *short-time Fourier transform*, or *spectrogram* (see [Cohen 1995]), can be used to estimate the evolutionary spectrum (see [Priestley 1965] or [Detka et al. 1993]). The *evolutionary periodogram* [Kayhan et al. 1994] is an estimator of the Wold-Cramér evolutionary spectrum. The high-resolution spectrogram introduced by Thomson [1990] is an estimator of the Wold-Cramér evolutionary spectrum, which in fact constitutes a special case of Kayhan’s evolutionary periodogram.

Available estimators of the various time-frequency spectra suffer from three key drawbacks. The first is that many estimators are based on a “sliding window” approach, or premultiply the data by sequences which tend to zero at their endpoints. This results in time-frequency spectrum estimates, which are only valid in restricted domains, typically away from the time boundaries of the time-frequency plane. The

second drawback, common to all time-frequency spectrum estimates is the well-known *uncertainty principle* [Cohen 1995]. The uncertainty principle says, roughly speaking, that there exists a fundamental trade-off between frequency resolution (the ability to discern closely-spaced frequency content) and time resolution (the ability to discern the times at which frequency content changes) of a time-frequency spectrum estimate. The third drawback is that all available estimates of the time-frequency spectra described above presuppose that the time-frequency spectrum is a continuous function of frequency. For this to occur, it is necessary that the underlying process does not possess any (purely harmonic frequencies) “line components”, since line components manifest as discontinuities.

To deal with the first drawback, we introduce a new estimator of Wold-Cramér evolutionary spectra, called the *modified time-frequency spectrum estimator*, or MTFSE. The MTFSE can be considered as a “sliding window” modification of the high-resolution spectrogram. We also introduce an estimator of the time derivative of Wold-Cramér evolutionary spectra, called the *time-derivative of the time-frequency spectrum estimator*, or TDTFSE. The MTFSE and TDTFSE estimate Wold-Cramér evolutionary spectra and their time derivatives, respectively, away from the time boundaries of the time-frequency plane. However, assuming that the Wold-Cramér evolutionary spectrum is (approximately) locally linear at each fixed frequency, we propose a modification of the MTFSE so that the Wold-Cramér evolutionary spectrum can be estimated near the time boundaries. We call this modified MTFSE the *boundary-corrected modified time-frequency spectrum estimator*, or BCMTFSE.

To deal with the second drawback, we show that if a process belongs to the class of *uniformly modulated* processes [Priestley 1965], then it is possible to estimate its Wold-Cramér evolutionary spectrum via a modification of the BCMTFSE with “good” time and frequency resolutions. This is possible for the following reasons. The Wold-Cramér evolutionary spectrum of a uniformly modulated process can be

written as a product of a purely time-dependent function known as its *modulation* and a purely frequency-dependent function which is the spectrum of a stationary process. With this in mind, we show that under a certain normalizing condition, the BCMTFSE can be used to estimate the modulation of a uniformly modulated process. The estimate of the modulation can then be used to improve the estimate of the stationary spectrum by improving its frequency resolution. We modify the BCMTFSE by multiplying the estimated modulation by the new estimate of the stationary spectrum to obtain a new estimator of Wold-Cramér evolutionary spectra. We call this estimator the *improved time-frequency spectrum estimator*, or ITFSE. Since ITFSE is derived under the assumption that the process of interest, say \mathbf{X} , is a uniformly modulated process, we introduce a heuristic graphical technique that uses the number of clearly separated singular values of the BCMTFSE (viewed as a rectangular matrix) to draw conclusions about whether \mathbf{X} is indeed a uniformly modulated process.

In most real-world applications of time series analysis, it is realistic to assume that the process of interest is comprised of a finite number of line components added to a nonstationary process having a continuous time-frequency spectrum. As a result, in order to deal with the third drawback, one must find ways to detect and remove line components from a given data set before applying any time-frequency estimator to it. The F -test for periodicity [Thomson 1982] can be used to detect line components. The main difficulty associated with using the F -test is that, due to sampling, one cannot avoid the problem of aliasing [Priestley 1981]. As a result of aliasing, line components whose frequencies lie outside the Nyquist band are “folded back” inside the Nyquist band and cannot be distinguished from line components whose frequencies lie inside the Nyquist band. We propose a graphical technique which is based on a coherence estimate [Thomson and Chave 1991] between a process and a time-delayed version of itself perturbed by stationary noise. Because of aliasing effects, the phase of the

coherence estimate departs from the linear trend which is expected since there is a time delay between the two processes. We show that knowledge of the time delay and the phase of the coherence estimate can be used to identify and unalias aliased line components.

This thesis is structured as follows. In Chapter 2, we review background material related to time-frequency analysis and the aliasing problem. In Chapter 3, we introduce the MTFSE and BCMTFSE to estimate Wold-Cramér evolutionary spectra. We derive expressions for the expected values and variances of these estimators and demonstrate their performance on simulated processes. In Chapter 4, we first introduce a heuristic graphical technique that can help one draw conclusions about the class to which a given nonstationary process belongs to. We also introduce the ITFSE, and demonstrate the performances of the graphical technique and the ITFSE on simulated processes. In Chapter 5, we introduce a graphical technique to unalias aliased line components. We demonstrate the performance of this technique on a simulated process and on a real-world example (17 years of solar daily noon flux data). In Chapter 6, we make some closing remarks and describe future avenues of research. Background material on prolate spheroidal wave functions and sequences, multitaper spectrum estimation, harmonic analysis, and coherence analysis is provided in Appendices A, B, C, and D, respectively.

Chapter 2

Background and Literature Review

2.1 Time-Frequency Analysis

One of the main goals of time-frequency analysis has been a description of the distribution of a given stochastic signal's energy as a joint function of time and frequency [Gabor 1946]. Such a distribution is commonly referred to as a *time-frequency distribution* of the signal. It is generally accepted that, ideally speaking, such a distribution should yield the correct time and frequency marginal densities, or marginals, and further that it be everywhere nonnegative to have a “proper” interpretation as a joint density function [Pitton 1997].

A significant contribution to the field of time-frequency analysis was made by [Cohen 1966], who gave a general unifying formulation for obtaining all time-frequency distributions known as the *Cohen's class* of distributions. Explicit in this approach is the selection of a kernel which determines the properties of the distribution. The choice of kernel in Cohen's class of distributions can be functionally dependent or independent of the signal. The problem with the distributions defined in Cohen's class is that, regardless of the choice of kernel, a distribution in Cohen's class cannot be everywhere nonnegative and yield the correct marginals simultaneously [Cohen

1995]. Most of the commonly used distributions introduced in Cohen’s class (see Table 9.1 on p.138 of [Cohen 1995]) have signal-independent kernels. These kernels yield distributions that are said to be “bilinear.” It is shown in [Cohen 1995] that bilinear distributions cannot be everywhere nonnegative, but do have the correct marginals. Therefore, to obtain everywhere nonnegative time-frequency distributions with the correct marginals, it is necessary to consider signal-dependent kernels [Pitton 1997]. Using signal-dependent kernels, Cohen and Posch [1985] gave a general form to all time-frequency distributions known as the *Cohen-Posch class* of distributions which have the correct marginals while being nonnegative.

In the following subsections, we give a brief overview of various approaches to the definition of a time-frequency distribution. In particular, we introduce two important distributions in Cohen’s class. First, a time-frequency distribution which has a signal-dependent kernel, known as the spectrogram, and second, a distribution based on a signal-independent kernel, known as the Wigner distribution. We also introduce other time-frequency distributions, including the evolutionary spectrum and the Wold-Cramér evolutionary spectrum; these distributions are not necessarily elements of the Cohen or Cohen-Posch classes. We also briefly review the Loève spectrum, which is a distribution valid for the class of harmonizable processes. For such processes, the Loève spectrum provides a type of distribution for nonstationary processes called the dual-frequency distribution.

2.1.1 Short-Time Fourier Transforms and Spectrograms

Let $\mathbf{X}_c \triangleq \{X(t)\}_{t \in \mathbb{R}}$ be a continuous-time real-valued nonstationary process. The short-time Fourier transform (STFT) is the most widely-used technique for studying nonstationary processes. The intuitive idea is that for a realization of \mathbf{X}_c denoted by $X(t)$, one splits the realization into smaller segments and computes the Fourier transform in each time segment [Cohen 1995]. The spectrogram of \mathbf{X}_c is a time-

frequency distribution; defined as

$$S_{\mathbf{X}}^G(t, f) \triangleq \left| \int_{\mathbb{R}} X(\tau) h(\tau - t) e^{-i2\pi f\tau} d\tau \right|^2, \quad \forall t, f \in \mathbb{R},$$

where h is a real-valued function of $t \in \mathbb{R}$ referred to as a *window function*. The spectrogram is a time-frequency distribution belonging to the Cohen's class. This distribution is nonnegative but it does not have the correct marginals [Cohen 1995].

The spectrogram is a useful procedure; however it should be mentioned that it is very empirical in the sense that it depends in an essential way on the choice of window function h . A common choice of the window function is a rectangular window. A rectangular window provides “good” frequency resolution but the spectrogram in this case suffers from Gibbs ripple [Hamming 1989]. To overcome Gibbs ripple, it is necessary to use a window function for the purpose of smoothing the spectrogram [Tukey and Hamming 1984]. However, the use of such window functions reduces the frequency resolution of the spectrogram depending on the smoothness of the window [Harris 1978].

2.1.2 Wigner-Ville Spectra

Let $\mathbf{X}_c \triangleq \{X(t)\}_{t \in \mathbb{R}}$ be a continuous-time complex-valued zero-mean nonstationary process with finite variance. The *Wigner-Ville spectrum* of \mathbf{X}_c , introduced by Wigner [1932] and Ville [1948], and denoted by $\mathbf{W}_{\mathbf{X}_c}$, is defined by

$$\mathbf{W}_{\mathbf{X}_c}(t, f) \triangleq \int_{\mathbb{R}} \mathbb{E} \left\{ X \left(t + \frac{\tau}{2} \right) \overline{X \left(t - \frac{\tau}{2} \right)} \right\} e^{-i2\pi f\tau} d\tau, \quad \forall t, f \in \mathbb{R},$$

where \mathbf{E} denotes the expectation operator. The Wigner-Ville spectrum is the expected value of

$$W_{\mathbf{X}_c}(t, f) = \int_{\mathbb{R}} X\left(t + \frac{\tau}{2}\right) \overline{X\left(t - \frac{\tau}{2}\right)} e^{-i2\pi f\tau} d\tau, \quad \forall t, f \in \mathbb{R},$$

which is known as the *Wigner-Ville distribution* or the *Wigner distribution* of \mathbf{X}_c [Flandrin 1999].

The Wigner distribution is a bilinear time-frequency distribution belonging to Cohen's class. The Wigner distribution yields the correct marginal densities of time and frequency [Cohen 1995], and is real-valued. However, it can take negative values, and therefore cannot be regarded as a "proper" distribution (see [Cohen 1995] or [Cohen and Posch 1985] for details).

2.1.3 Evolutionary Spectra

Let $\mathbf{X}_c \triangleq \{X(t)\}_{t \in \mathbb{R}}$ be a continuous-time complex-valued zero-mean nonstationary process with finite variance. Following [Priestley 1965], if \mathbf{X}_c can be represented in the form

$$X(t) = \int_{\mathbb{R}} M(t, f) e^{i2\pi ft} dZ_{\mathbf{X}_c}(f), \quad \forall t \in \mathbb{R},$$

where $\{Z_{\mathbf{X}_c}(f)\}_{f \in \mathbb{R}}$ is a complex-valued orthogonal-increment process associated with \mathbf{X}_c and the function M is "slowly varying," then \mathbf{X}_c is called an *oscillatory process*.

The *evolutionary spectrum* of \mathbf{X}_c introduced by Priestley [1965], is the function defined by

$$S_{\mathbf{X}_c}^E(t, f) \triangleq |M(t, f)|^2 S_{\mathbf{X}_c}(f), \quad \forall t, f \in \mathbb{R},$$

where $S_{\mathbf{X}_c}(f) df = \mathbf{E}\{|dZ_{\mathbf{X}_c}(f)|^2\}$.

The evolutionary spectrum generalizes the notion of a spectral density function to the class of oscillatory processes. In contrast with the (time-invariant) stationary case, the evolutionary spectrum describes the local power-frequency distribution of an oscillatory process at each time instant.

The evolutionary spectrum is a nonnegative time-frequency distribution but does not belong to the Cohen-Posch class since it does not yield the correct marginal densities of time and frequency [Pitton et al. 1993]. However, it is shown in [Pitton et al. 1993] that under certain types of normalization conditions on M , the evolutionary spectrum can be looked at as a member of the Cohen-Posch class.

2.1.4 Wold-Cramér Evolutionary Spectra

Let $\mathbf{X} \triangleq \{X_t\}_{t \in \mathbb{Z}}$ be a discrete-time real-valued nonstationary process. Cramér [1961] showed that if \mathbf{X} is nondeterministic, it has a “one-sided” linear representation of the form

$$X_t = \sum_{n=-\infty}^t h_{\mathbf{X}}(t, n) \varepsilon_n, \quad \forall t \in \mathbb{Z},$$

where the $h_{\mathbf{X}}$ are real-valued coefficients and $\{\varepsilon_t\}_{t \in \mathbb{Z}}$ is a stationary zero-mean unit-variance white noise process. This representation of \mathbf{X} is in fact an extension of the Wold decomposition [Wold 1954] in the stationary case; as a result, it is sometimes referred to as the Wold-Cramér decomposition of \mathbf{X} [Priestley 1988].

Assuming that \mathbf{X} has a Wold-Cramér decomposition, Mélard [1975] and Tjøstheim [1976] independently introduced a time-frequency spectrum for \mathbf{X} called the *Wold-Cramér evolutionary spectrum* [Mélard and Schutter 1989], defined by

$$S_{\mathbf{X}}^W(t, f) \triangleq \left| \sum_{n=-\infty}^t h_{\mathbf{X}}(t, n) e^{-i2\pi f(t-n)} \right|^2, \quad \forall f \in \mathbb{R}, \forall t \in \mathbb{Z}.$$

The Wold-Cramér evolutionary spectrum is a nonnegative time-frequency distribution that yields the correct marginal densities of time and frequency [Pitton 1997]. As a result, it is a member of the Cohen-Posch class.

2.1.5 Harmonizable Processes and Loève Spectra

Let $\mathbf{X}_c \triangleq \{X(t)\}_{t \in \mathbb{R}}$ be a continuous-time complex-valued zero-mean nonstationary process. Then \mathbf{X}_c is said to be *harmonizable* [Loève 1946] if it has a *spectral representation* of the form

$$X(t) = \int_{\mathbb{R}} e^{i2\pi ft} dZ_{\mathbf{X}_c}(f), \quad \forall t \in \mathbb{R},$$

where $\{Z_{\mathbf{X}_c}(f)\}_{f \in \mathbb{R}}$ is a complex-valued process possibly having nonorthogonal increments [Martin 1982]. As a result, $\mathbb{E}\{dZ_{\mathbf{X}_c}(f) \overline{dZ_{\mathbf{X}_c}(f')}\} = S_{\mathbf{X}_c, L}(f, f') df df'$ for all $f, f' \in \mathbb{R}$; The function $S_{\mathbf{X}_c, L}$ is known as the *Loève spectrum* or *dual-frequency spectrum* of \mathbf{X}_c . The covariance function of \mathbf{X}_c is then given by

$$R_{\mathbf{X}_c}(t, t') = \mathbb{E}\{X(t) \overline{X(t')}\} = \int_{\mathbb{R}} \int_{\mathbb{R}} e^{i2\pi(tf - t'f')} S_{\mathbf{X}_c, L}(f, f') df df', \quad \forall t, t' \in \mathbb{R}.$$

The Loève spectrum describes a nonstationary process' deviation from stationarity by quantifying the “correlation” between frequencies $f, f' \in \mathbb{R}$.

2.2 Aliasing

Let $\mathbf{X}_c \triangleq \{X(t)\}_{t \in \mathbb{R}}$ be a continuous-time real-valued zero-mean stationary process. We assume that \mathbf{X}_c is stationary, so it has a Cramér or spectral representation (see Appendix B) of the form

$$X(t) = \int_{\mathbb{R}} e^{i2\pi ft} dZ_{\mathbf{X}_c}(f), \quad \forall t \in \mathbb{R},$$

where $\{Z_{\mathbf{X}_c}(f)\}_{f \in \mathbb{R}}$ is a complex-valued orthogonal-increment process associated with \mathbf{X}_c satisfying $S_{\mathbf{X}_c}(f) df = \mathbf{E}\{|dZ_{\mathbf{X}_c}(f)|^2\}$, where $S_{\mathbf{X}_c}$ is the spectrum of \mathbf{X}_c .

Now define a discrete-time real-valued zero-mean stationary process $\mathbf{X} \triangleq \{X_t\}_{t \in \mathbb{Z}}$ by setting $X_t \triangleq X(t\Delta T)$ for each $t \in \mathbb{Z}$, where the non-negative real number ΔT is the *sampling interval*. Using the spectral representation of \mathbf{X}_c and the relationship between \mathbf{X} and \mathbf{X}_c , we obtain

$$\begin{aligned}
X_t &= \int_{\mathbb{R}} e^{i2\pi ft\Delta T} dZ_{\mathbf{X}_c}(f) \\
&= \sum_{k=-\infty}^{\infty} \int_{\frac{2k-1}{2\Delta T}}^{\frac{2k+1}{2\Delta T}} e^{i2\pi ft\Delta T} dZ_{\mathbf{X}_c}(f) \\
&= \sum_{k=-\infty}^{\infty} \int_{\frac{-1}{2\Delta T}}^{\frac{1}{2\Delta T}} e^{i2\pi(f + \frac{k}{\Delta T})t\Delta T} dZ_{\mathbf{X}_c}\left(f + \frac{k}{\Delta T}\right) \\
&= \int_{\frac{-1}{2\Delta T}}^{\frac{1}{2\Delta T}} e^{i2\pi ft\Delta T} \sum_{k=-\infty}^{\infty} dZ_{\mathbf{X}_c}\left(f + \frac{k}{\Delta T}\right) e^{i2\pi kt} \\
&= \int_{-\mathcal{F}_n}^{\mathcal{F}_n} e^{i2\pi ft\Delta T} dZ_{\mathbf{X}}(f), \quad \forall t, k \in \mathbb{Z},
\end{aligned}$$

where $\mathcal{F}_n \triangleq \frac{1}{2\Delta T}$ is the *Nyquist frequency*, and since $t, k \in \mathbb{Z}$, we have $e^{i2\pi kt} = 1$ and as a result

$$dZ_{\mathbf{X}}(f) \triangleq \sum_{k=-\infty}^{\infty} dZ_{\mathbf{X}_c}\left(f + \frac{k}{\Delta T}\right), \quad \forall f \in [-\mathcal{F}_n, \mathcal{F}_n].$$

It can be shown that $\{Z_{\mathbf{X}}(f)\}_{f \in \mathbb{R}}$ is an orthogonal-increment process associated with \mathbf{X} satisfying $S_{\mathbf{X}}(f) df = \mathbf{E}\{|dZ_{\mathbf{X}}(f)|^2\}$, where $S_{\mathbf{X}}$ is the spectrum of \mathbf{X} [Priestley 1981]. For example the orthogonal increments property of $\{Z_{\mathbf{X}}(f)\}_{f \in \mathbb{R}}$ follows from the fact that

$$\mathbf{E}\left\{dZ_{\mathbf{X}}(f) \overline{dZ_{\mathbf{X}}(f')}\right\} = \sum_{k=-\infty}^{\infty} \sum_{l=-\infty}^{\infty} \mathbf{E}\left\{dZ_{\mathbf{X}_c}\left(f + \frac{k}{\Delta T}\right) \overline{dZ_{\mathbf{X}_c}\left(f' + \frac{l}{\Delta T}\right)}\right\} = 0, \quad \forall f \neq f'.$$

As a result, we have

$$S_{\mathbf{X}}(f) df = \sum_{k=-\infty}^{\infty} \mathbb{E} \left\{ \left| dZ_{\mathbf{X}_c} \left(f + \frac{k}{\Delta T} \right) \right|^2 \right\} = \sum_{k=-\infty}^{\infty} S_{\mathbf{X}_c} \left(f + \frac{k}{\Delta T} \right) df, \quad \forall f \in [-\mathcal{F}_n, \mathcal{F}_n].$$

Hence at each frequency f , $S_{\mathbf{X}}(f)$ is a sum of contributions from $S_{\mathbf{X}_c}$ at a countably infinite number of frequencies $f, f \pm \frac{1}{\Delta T}, f \pm \frac{2}{\Delta T}, f \pm \frac{3}{\Delta T}, \dots$. This phenomenon is called *aliasing*, and the frequency $f \in [-\mathcal{F}_n, \mathcal{F}_n]$ is said to be *aliased* with each of the frequencies $f \pm \frac{1}{\Delta T}, f \pm \frac{2}{\Delta T}, f \pm \frac{3}{\Delta T}, \dots$. The latter frequencies are called the *aliases* of f [Priestley 1981].

In the remainder of this section, we briefly describe several methods to deal with aliasing.

2.2.1 Change of Sampling Interval

It is impossible to recover $S_{\mathbf{X}_c}$ from $S_{\mathbf{X}}$, unless $S_{\mathbf{X}}$ is identically zero outside of $[-\mathcal{F}_n, \mathcal{F}_n]$. In general, if $S_{\mathbf{X}_c}$ is “band-limited,” meaning that there exists a frequency f_0 known as the *cutoff frequency* such that $S_{\mathbf{X}_c}(f) = 0$ when $|f| > f_0$, then we can always choose ΔT sufficiently small so that $\Delta T \leq \frac{1}{2f_0}$ or in other words $f_0 \leq \mathcal{F}_n$. In a more realistic scenario, $S_{\mathbf{X}_c}$ is not zero outside of $[-\mathcal{F}_n, \mathcal{F}_n]$, but, under the assumption that $S_{\mathbf{X}_c}(f)$ tends to zero as $|f| \rightarrow \infty$, we can then hope to reduce the aliasing effect by selecting ΔT sufficiently small so that $S_{\mathbf{X}_c}$ is negligible outside of $[-\mathcal{F}_n, \mathcal{F}_n]$ [Priestley 1981].

2.2.2 Anti-Aliasing Filters

In practice, it is sometimes possible to determine the frequency limit beyond which $S_{\mathbf{X}_c}$ is negligible from a knowledge of the frequency range of the recording mechanism. Alternatively, if we know that we are interested in recovering $S_{\mathbf{X}_c}$ only over a restricted range, say for $|f| \leq f_0$, then we can pass a given realization of \mathbf{X}_c through a band-

pass filter to effectively remove all frequencies with $|f| > f_0$. As a result, for $f_0 \leq \mathcal{F}_n$, $\Delta T \leq \frac{1}{2f_0}$ and therefore for a selected ΔT the realization of \mathbf{X}_c can be sampled. Such a band-pass filter is known as an *anti-aliasing filter*.

A wide range of anti-aliasing filters have been used in applications such as digital photography [Pritchard 1971], [Pritchard 1973], computer graphics [Crow 1977], [Catmull 1978], [Crow 1981], and digital audio [Farhad and Mirzakuchaki 2008], [Malekpour et al. 2008], [Klepser et al. 2003].

2.2.3 Unaliasing after Sampling

Suppose that one is given a realization of \mathbf{X}_c , and that one has no knowledge about the frequencies for which $S_{\mathbf{X}_c}$ is nonzero. In this case, the cutoff frequency f_0 is not known, and applying an anti-aliasing filter may remove essential frequency content from the realization. As an alternative, one can attempt to detect the aliased frequencies by some other means, and then to unalias them.

Rader [1977] introduced a technique to recover periodic waveforms using a so called minimum-variation procedure. Sanderson et al. [1992] points out that the method introduced by Rader [1977] allows considerable generality in the waveform, but it is not very well-adapted to real-time processing. Sanderson et al. [1992] therefore introduced a new technique that used two signals, one being a time-delayed of the other, and used the phase shift in the periodic signal to eliminate the aliasing effect.

Chapter 3

Time-Frequency Spectrum Estimation with Improved Boundary Performance

3.1 Introduction

A common assumption in time series analysis is that the time series under study is a realization of a stationary stochastic process. However, as mentioned in Chapter 1 many time series of important practical interest, such as those arising in the physical sciences are known to exhibit “sporadic” behaviour [Thomson 2000]; these are features which cannot be captured by stationary models. Therefore, nonstationarity should be considered if one is to carry out realistic modeling and analysis of these and other types of time series.

The evolutionary spectrum, introduced in Priestley [1965], is a time-dependent analogue of the spectrum of a stationary process, valid for a class of nonstationary processes known as *oscillatory processes* (see Section 2.1.3). Loosely speaking, the evolutionary spectrum describes the local power-frequency distribution at each instant

of time, which preserves the physical interpretation of the spectrum of a stationary process as a power-frequency distribution. On the other hand, the Wold-Cramér evolutionary spectrum, introduced by Mélard [1975] and Tjøstheim [1976], is a different time-dependent analogue of the spectrum of a stationary process which is valid for all nonstationary processes [Flandrin 1999]. Briefly, any nonstationary process can be represented as the output of a causal linear time-varying filter with white noise input. Using this fact, the Wold-Cramér evolutionary spectrum of a nonstationary process is defined to be the squared magnitude of the generalized transfer function of the filter.

Following the introduction of the Wold-Cramér evolutionary spectrum, several techniques have been proposed to estimate it. The evolutionary periodogram estimator, developed in [Kayhan et al. 1994], is an estimator of the Wold-Cramér evolutionary spectrum. Independently, Thomson [1998] introduced the high-resolution spectrogram, which is essentially the same as the evolutionary periodogram estimator with discrete prolate spheroidal sequences (see Appendix A) chosen as the orthogonal basis.

All available estimators of the Wold-Cramér evolutionary spectrum suffer from inherent problems with time and frequency resolution [Kayhan et al. 1994]. Furthermore, due to tapering effects, all available estimators suffer from “bias” at the boundaries of the time-frequency plane. In this chapter, we develop an estimator of the Wold-Cramér evolutionary spectrum for which this “boundary behaviour” is improved, using an estimate of the “time derivative” of the Wold-Cramér evolutionary spectrum. We demonstrate the applicability of our estimator to several simulated nonstationary processes including uniformly modulated processes, which form a subclass of the class of oscillatory processes [Priestley 1988].

This chapter is structured as follows. In Section 3.2, we review some background material regarding the theory of evolutionary spectra, and the theory of uniformly

modulated processes. In Section 3.3, we review background material on the Wold-Cramér evolutionary spectrum. In Section 3.4, we review an established estimator of the Wold-Cramér evolutionary spectrum. In Section 3.5, we review a method that approximates the Wold-Cramér evolutionary spectrum with a linear expansion. In Section 3.6, we develop an estimator of the Wold-Cramér evolutionary spectrum with improved time resolution. In Section 3.7, we introduce a method to smooth the estimator from Section 3.6, and extrapolate the Wold-Cramér evolutionary spectrum near the time boundaries of the time-frequency plane. In Section 3.8, we derive the means and variances of the estimator from Section 3.7. In Section 3.9, we demonstrate the performance of BCMTFSE on several simulated nonstationary processes.

3.2 Evolutionary Spectra

Let $\mathbf{X} \triangleq \{X_t\}_{t \in \mathbb{Z}}$ be a discrete-time complex-valued stochastic process, with zero mean and finite variance, *i.e.*,

$$\mathbb{E}\{X_t\} = 0 \quad \text{and} \quad \mathbb{E}\{|X_t|^2\} < \infty, \quad \forall t \in \mathbb{Z}.$$

We assume that \mathbf{X} is such that there exists a family $\mathcal{F}_{\mathbf{X}} \triangleq \{\Phi_t : [-1/2, 1/2] \rightarrow \mathbb{C}\}_{t \in \mathbb{Z}}$ of complex-valued measurable functions and a nonnegative function $S_{\mathbf{X}} : [-1/2, 1/2] \rightarrow \mathbb{R}$, such that for all $t, s \in \mathbb{Z}$, the covariance function $R_{\mathbf{X}}$ of \mathbf{X} can be written as

$$R_{\mathbf{X}}(t, s) \triangleq \mathbb{E}\{X_t \overline{X_s}\} = \int_{-1/2}^{1/2} \Phi_t(f) \overline{\Phi_s(f)} S_{\mathbf{X}}(f) \, df, \quad (3.1)$$

where the overline denotes complex conjugation. Since \mathbf{X}_t has finite variance for each $t \in \mathbb{Z}$, Φ_t must be square-integrable with respect to $S_{\mathbf{X}}$ for each $t \in \mathbb{Z}$, since

$$\text{Var}\{X_t\} \triangleq R_{\mathbf{X}}(t, t) = \int_{-1/2}^{1/2} |\Phi_t(f)|^2 S_{\mathbf{X}}(f) df < \infty, \quad \forall t \in \mathbb{Z}. \quad (3.2)$$

Since the covariance function $R_{\mathbf{X}}$ can be written in the form shown in Eq. (3.1), by the general orthogonal expansion theorem [Priestley 1981], \mathbf{X} admits a representation of the form

$$X_t = \int_{-1/2}^{1/2} \Phi_t(f) dZ_{\mathbf{X}}(f), \quad \forall t \in \mathbb{Z}, \quad (3.3)$$

where $\{Z_{\mathbf{X}}(f)\}_{f \in [-1/2, 1/2]}$ is a complex-valued orthogonal-increment process associated with \mathbf{X} satisfying

$$\mathbb{E}\{|dZ_{\mathbf{X}}(f)|^2\} = S_{\mathbf{X}}(f) df, \quad \forall f \in [-1/2, 1/2].$$

Now suppose that for each fixed $f_0 \in [-1/2, 1/2]$, $t \mapsto \Phi_t(f_0)$ has a generalized Fourier transform whose modulus is maximized at the frequency $\theta(f_0) \in [-1/2, 1/2]$. In this case, the function $(t, f) \mapsto \Phi_t(f)$ can be represented in an amplitude-modulated complex exponential form,

$$\Phi_t(f) = M_t(f) e^{i2\pi\theta(f)t}, \quad (3.4)$$

where the *modulating function* M is such that for each fixed $f_0 \in [-1/2, 1/2]$, $t \mapsto M_t(f_0)$ has a generalized Fourier transform whose modulus is maximized at zero frequency. (For this reason M is sometimes referred to as a “slowly varying” function in t .)

If the function $(t, f) \mapsto \Phi_t(f)$ can be written in the form shown in Eq. (3.4), it is

called an *oscillatory* function, and \mathbf{X} is called an *oscillatory* process [Priestley 1965].

If \mathbf{X} is oscillatory, it follows that \mathbf{X} can be represented as

$$X_t = \int_{-1/2}^{1/2} M_t(f) e^{i2\pi ft} dZ_{\mathbf{X}}(f), \quad \forall t \in \mathbb{Z}. \quad (3.5)$$

Substituting Eq. (3.4) into Eq. (3.2) gives

$$\text{Var}\{X_t\} = R_{\mathbf{X}}(t, t) = \int_{-1/2}^{1/2} |M_t(f)|^2 S_{\mathbf{X}}(f) df < \infty, \quad \forall t \in \mathbb{Z}.$$

Motivated by the above equation, Priestley [1965] defined the *evolutionary spectrum* of \mathbf{X} at each $t \in \mathbb{Z}$ with respect to the family $\mathcal{F}_{\mathbf{X}} = \{\Phi_t : f \mapsto M_t(f) e^{i2\pi ft}\}_{t \in \mathbb{Z}}$ to be the function $S_{\mathbf{X}} : \mathbb{Z} \times [-1/2, 1/2] \rightarrow \mathbb{R}$ defined by

$$S_{\mathbf{X}}^E(t, f) \triangleq |M_t(f)|^2 S_{\mathbf{X}}(f), \quad \forall t \in \mathbb{Z}, \forall f \in [-1/2, 1/2].$$

3.2.1 Uniformly Modulated Processes

Let $\mathbf{X} \triangleq \{X_t\}_{t \in \mathbb{Z}}$ be an oscillatory process. We say that \mathbf{X} is a *uniformly modulated process* (UMP) if there exists a zero-mean stationary process $\mathbf{Y} \triangleq \{Y_t\}_{t \in \mathbb{Z}}$ and a nonnegative sequence $\{C_t\}_{t \in \mathbb{Z}} \subset \mathbb{R}$ such that

1. $\{C_t\}$ has a generalized Fourier transform whose modulus is maximized at zero frequency; and
2. $X_t = C_t Y_t, \quad \forall t \in \mathbb{Z}.$

Since \mathbf{Y} is stationary, by the spectral representation theorem (see Appendix B), we can write

$$Y_t = \int_{-1/2}^{1/2} e^{i2\pi ft} dZ_{\mathbf{Y}}(f), \quad \forall t \in \mathbb{Z}, \quad (3.6)$$

where $\{Z_{\mathbf{Y}}(f)\}_{f \in [-1/2, 1/2]}$ is a complex-valued orthogonal-increment process associated with \mathbf{Y} satisfying

$$\mathbb{E}\{|dZ_{\mathbf{Y}}(f)|^2\} = S_{\mathbf{Y}}(f) df, \quad \forall f \in [-1/2, 1/2]. \quad (3.7)$$

Substituting Eq. (3.6) into $X_t = C_t Y_t$ yields

$$X_t = \int_{-1/2}^{1/2} C_t e^{i2\pi ft} dZ_{\mathbf{Y}}(f), \quad \forall t \in \mathbb{Z}. \quad (3.8)$$

The evolutionary spectrum of \mathbf{X} with respect to the family $\mathcal{F}_{\mathbf{X}, U} \triangleq \{\Phi_t : f \mapsto C_t e^{i2\pi ft}\}_{t \in \mathbb{Z}}$ is then given by

$$S_{\mathbf{X}}^E(t, f) = C_t^2 S_{\mathbf{Y}}(f), \quad \forall t \in \mathbb{Z}, \forall f \in [-1/2, 1/2]. \quad (3.9)$$

3.3 Wold-Cramér Evolutionary Spectra

Let $\mathbf{X} \triangleq \{X_t\}_{t \in \mathbb{Z}}$ be a discrete-time real-valued zero-mean nonstationary process. According to the Wold-Cramér decomposition, \mathbf{X} can be represented as the output of a causal linear time-varying filter [Mélard and Schutter 1989] with impulse response $h_{\mathbf{X}}$,

$$X_t = \sum_{n=-\infty}^t h_{\mathbf{X}}(t, n) \varepsilon_n, \quad \forall t \in \mathbb{Z}, \quad (3.10)$$

where $\mathbf{E} \triangleq \{\varepsilon_t\}_{t \in \mathbb{Z}}$ is a stationary zero-mean, unit-variance white noise process. By the spectral representation theorem, we can write

$$\varepsilon_t = \int_{-1/2}^{1/2} e^{i2\pi ft} dZ_{\mathbf{E}}(f), \quad \forall t \in \mathbb{Z}, \quad (3.11)$$

where $\{Z_{\mathbf{E}}(f)\}_{f \in [-1/2, 1/2]}$ is an orthogonal-increment process associated with \mathbf{E} satisfying

$$\mathbf{E}\{|dZ_{\mathbf{E}}(f)|^2\} = df.$$

Substituting Eq. (3.11) into Eq. (3.10) yields

$$X_t = \int_{-1/2}^{1/2} H_t(f) e^{i2\pi ft} dZ_{\mathbf{E}}(f), \quad \forall t \in \mathbb{Z}, \quad (3.12)$$

where H_t is Zadeh's generalized transfer function [Zadeh 1950], defined for each $t \in \mathbb{Z}$ by

$$H_t(f) \triangleq \sum_{n=-\infty}^t h_{\mathbf{X}}(t, n) e^{-i2\pi f(t-n)}, \quad \forall f \in [-1/2, 1/2]. \quad (3.13)$$

From Eq. (3.12), it can be seen that

$$\text{Var}\{X_t\} = \mathbf{E}\{|X_t|^2\} = \int_{-1/2}^{1/2} |H_t(f)|^2 df$$

for each $t \in \mathbb{Z}$. The *Wold-Cramér evolutionary spectrum* of \mathbf{X} , introduced independently by Mélard [1975] and Tjøstheim [1976], is defined by

$$S_{\mathbf{X}}^W(t, f) \triangleq |H_t(f)|^2 = \left| \sum_{n=-\infty}^t h_{\mathbf{X}}(t, n) e^{-i2\pi f(t-n)} \right|^2 \quad (3.14)$$

for each $t \in \mathbb{Z}$ and $f \in [-1/2, 1/2]$.

The key differences between the Wold-Cramér evolutionary spectrum and the evolutionary spectrum are the following:

- The Wold-Cramér evolutionary spectrum is unique, whereas the evolutionary spectrum may not be unique, depending on the possible choices of families

of oscillatory functions (see [Mélard and Schutter 1989] or [Priestley 1988] for details).

- If one restricts the functions H_t from Eq. (3.13) to belong to the class of oscillatory functions (see Section 3.2), the Wold-Cramér evolutionary spectrum $S_{\mathbf{X}}^W$ is the evolutionary spectrum of \mathbf{X} induced by the Wold-Cramér decomposition of \mathbf{X} (again, see [Mélard and Schutter 1989] or [Priestley 1988] for details).

We note that if \mathbf{X} is a (discrete-time) UMP, the time-varying impulse response $h_{\mathbf{X}}$ from Eq. (3.10) can be written in the form

$$h_{\mathbf{X}}(t, n) = C_t h_{\mathbf{Y}}(t - n), \quad (3.15)$$

where $h_{\mathbf{Y}}$ is the time-invariant impulse response associated with the stationary process \mathbf{Y} . Substituting Eq. (3.15) into Eq. (3.14), the Wold-Cramér evolutionary spectrum of \mathbf{X} is

$$\begin{aligned} S_{\mathbf{X}}^W(t, f) &= \left| \sum_{n=-\infty}^t h_{\mathbf{X}}(t, n) e^{-i2\pi f(t-n)} \right|^2 \\ &= \left| \sum_{n=-\infty}^t C_t h_{\mathbf{Y}}(t - n) e^{-i2\pi f(t-n)} \right|^2 \\ &= C_t^2 \left| \sum_{n=-\infty}^t h_{\mathbf{Y}}(t - n) e^{-i2\pi f(t-n)} \right|^2 \\ &= C_t^2 S_{\mathbf{Y}}(f), \quad \forall t \in \mathbb{Z}, f \in \mathbb{R}, \end{aligned}$$

which is the same as the evolutionary spectrum from Eq. (3.9).

3.4 High-Resolution Spectrograms

Let $\mathbf{X} \triangleq \{X_t\}_{t \in \mathbb{Z}}$ be a discrete-time real-valued zero-mean nonstationary process. The spectral representation theorem are valid only for stationary processes. In the nonstationary case, if \mathbf{X} has a representation of the form

$$X_t = \int_{-1/2}^{1/2} e^{i2\pi ft} dZ_{\mathbf{X}}(f), \quad \forall t \in \mathbb{Z}, \quad (3.16)$$

where $\{Z_{\mathbf{X}}(f)\}_{f \in [-1/2, 1/2]}$ is a complex-valued process (possibly with nonorthogonal increments) associated to \mathbf{X} , then \mathbf{X} is said to be (discrete-time) *harmonizable*. The class of harmonizable processes was introduced by Loève [1946]. The *dual-frequency spectrum* of a discrete-time harmonizable process \mathbf{X} , denoted by $S_{\mathbf{X},L}$, is defined by the equation $E\{dZ_{\mathbf{X}}(f) \overline{dZ_{\mathbf{X}}(f')}\} = S_{\mathbf{X},L}(f, f') df df'$ for all $f, f' \in [-1/2, 1/2]$ (see Section 2.1.5).

Assuming that \mathbf{X} is harmonizable, we can estimate its time-frequency spectrum (see [Martin 1982] or [Scharf et al. 1998]) as follows. Let X_0, X_1, \dots, X_{N-1} be a realization of \mathbf{X} , Thomson [1998] proposed an estimate of $dZ_{\mathbf{X}}$ from Eq. (3.16) in the frequency band $(f - W, f + W)$, where $W \ll 1/2$ is the *analysis bandwidth* (see Appendix B for details on why estimating $dZ_{\mathbf{X}}$ is important):

$$\widehat{dZ_{\mathbf{X}}}(f \ominus \xi) \triangleq \sum_{k=0}^{K-1} \frac{V_k(N, W; \xi)}{\lambda_k(N, W)} \frac{y_k(f)}{\lambda_k(N, W)}, \quad (3.17)$$

where $f \ominus \xi$ denotes $f - \xi$ with the understanding that ξ is restricted to $(-W, W)$, $K \leq \lfloor 2NW \rfloor$, y_k is the k th eigencoefficient (Appendix B, Eq. (B.7)), $V_k(N, W; \cdot)$ is the k th Slepian function (Appendix A, Eq. (A.12)), and $\lambda_k(N, W)$ is the k th eigenvalue of the (uncentered) Dirichlet kernel (Appendix A, Eq. (A.12)).

Thomson [1990] defined a complex demodulate of \mathbf{X} at a fixed frequency $f \in \mathbb{R}$

by Fourier transforming $\widehat{dZ_{\mathbf{X}}}$ inside the frequency band $(-W, W)$,

$$m_{\mathbf{X}}(t; f) \triangleq \int_{-W}^W \widehat{dZ_{\mathbf{X}}}(f \ominus \xi) e^{-i2\pi\xi t} d\xi, \quad \forall t \in \mathbb{Z}. \quad (3.18)$$

Substituting Eq. (3.17) into Eq. (3.18) and making use of Eq. (A.18) in Appendix A and Eq. (B.7) in Appendix B, we have

$$\begin{aligned} m_{\mathbf{X}}(t; f) &= \sum_{k=0}^{K-1} \nu_t^{(k)}(N, W) y_k(f) \\ &= \sum_{k=0}^{K-1} \nu_t^{(k)}(N, W) \sum_{n=0}^{N-1} X_n \nu_n^{(k)}(N, W) e^{-i2\pi f n}, \end{aligned} \quad (3.19)$$

where $\{\nu_t^{(k)}(N, W)\}_{t=0}^{N-1}$ is the k th DPSS (see Appendix A).

According to Thomson [1990], the squared amplitude $|m_{\mathbf{X}}(t; f)|^2$ represents the distribution of power at time t and frequency f . Following [Thomson 1990], an estimate of the time-dependent spectrum of \mathbf{X} , referred to as the *high-resolution spectrogram* (HRS), is given by

$$\widehat{S_{\mathbf{X}}^H}(t, f) \triangleq \frac{N}{K} \left| \sum_{k=0}^{K-1} \nu_t^{(k)}(N, W) \sum_{n=0}^{N-1} X_n \nu_n^{(k)}(N, W) e^{-i2\pi f n} \right|^2, \quad \forall t \in \mathbb{Z}, \forall f \in \mathbb{R}. \quad (3.20)$$

Independently, Kayhan et al. [1994] suggested a technique to estimate the Wold-Cramér evolutionary spectrum of \mathbf{X} shown in Eq. (3.14). The estimator is known as the *evolutionary periodogram* (EP), and is defined by

$$\widehat{S_{\mathbf{X}}^W}(t, f) \triangleq \frac{N}{M} \left| \sum_{m=0}^{M-1} \beta_t^{(m)} \sum_{n=0}^{N-1} X_n \beta_n^{(m)} e^{-i2\pi f n} \right|^2, \quad \forall t \in \mathbb{Z}, \forall f \in \mathbb{R}, \quad (3.21)$$

where $M \leq N$, and $\{\beta_t^{(0)}\}_{t=0}^{N-1}$, $\{\beta_t^{(1)}\}_{t=0}^{N-1}$, \dots , $\{\beta_t^{(M-1)}\}_{t=0}^{N-1}$ are a set of orthonormal data tapers ¹.

¹The terms data taper, window, window function are synonymous.

The innovation of the HRS, then, lies essentially in the choice of the DPSS as data tapers. To estimate the Wold-Cramér evolutionary spectrum, we primarily use the HRS because the DPSS $\nu_t^{(0)}, \dots, \nu_t^{(K-1)}$ form a set of pairwise orthonormal data tapers which are optimally concentrated in frequency in the interval $(-W, W)$ (see Appendix A). In the remainder of this thesis, we refer to the Wold-Cramér evolutionary spectrum of \mathbf{X} as the *time-frequency spectrum* of \mathbf{X} , and we denote it by $S_{\mathbf{X}}$.

There are drawbacks to the HRS estimator: First, it is unnecessarily restrictive to assume that K is not a function of time and frequency. Indeed, for a fixed pair (t, f) , K should be chosen to reflect the degree to which $S_{\mathbf{X}}$ varies in t and f . Second, since the DPSSs tend to zero as $t \rightarrow 0$ and $t \rightarrow N - 1$, $\widehat{S}_{\mathbf{X}}^H(t, f)$ tends to zero as $(t, f) \rightarrow (0, f)$ and $(t, f) \rightarrow (N - 1, f)$, for each fixed $f \in [-1/2, 1/2]$.

3.5 Nonstationary Quadratic-Inverse Theory

Let $\mathbf{X} = \{X_t\}_{t \in \mathbb{Z}}$ be a discrete-time zero-mean real-valued nonstationary process. Let X_0, X_1, \dots, X_{N-1} be a realization of \mathbf{X} . The *nonstationary quadratic-inverse* (NSQI) theory, developed by Thomson [1993], is based on a linear approximation of the time-frequency spectrum of \mathbf{X} of the form

$$S_{\mathbf{X}}(t, f) \approx \sum_{l=0}^L a_l(f) A_l(t), \quad \forall t \in \mathbb{Z}, \forall f \in [-1/2, 1/2]. \quad (3.22)$$

Here the $a_l : [-1/2, 1/2] \rightarrow \mathbb{R}$, $l \in \{0, 1, \dots, L\}$, are unknown functions which we call *expansion coefficients*. The sequences $\{A_l(t)\}_{t \in \mathbb{Z}}$, $l \in \{0, 1, \dots, L\}$ are the solutions of the algebraic eigenvalue equation

$$\alpha_l A_l(t) = N \sum_{m=0}^{N-1} \left[\frac{\sin 2\pi W(t-m)}{\pi(t-m)} \right]^2 A_l(m), \quad (3.23)$$

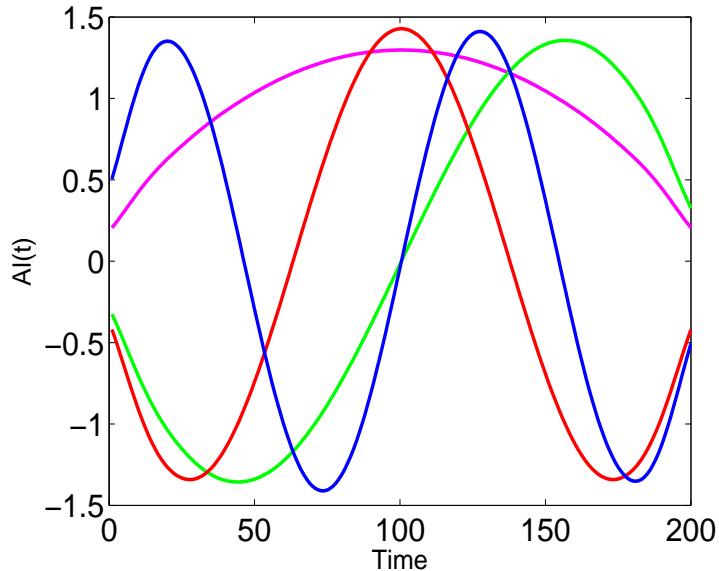


Figure 3.1: **Sequences** A_l for $l \in \{0, 1, 2, 3\}$. Sequences $A_l(t)$ with $N = 200$ and $W = 1/40$; $l = 0$ (magenta line), $l = 1$ (green line), $l = 2$ (red line) and $l = 3$ (blue line).

extended to be zero for $t < 0$ and $t > N$. (Note that the A_l depend in an essential way on the choice of analysis bandwidth W , although the notation does not reflect this.) In the following, we will write the sequences $\{A_l(t)\}_{t=0}^{N-1} \subset \mathbb{R}$, $l \in \{0, 1, \dots, L\}$, simply as A_l . The A_l satisfy the orthogonality property

$$\sum_{t=0}^{N-1} A_j(t)A_k(t) = N\delta_{j,k}, \quad (3.24)$$

where $\delta_{j,k}$ denotes the Kronecker delta. It is known that the eigenvalues α_l satisfy $\alpha_l \approx \max(2NW - l/2, 0)$ for each $l \in \{0, 1, \dots, \lfloor 4NW \rfloor\}$ [Thomson 1993]. The sequences A_l for $l \in \{0, 1, 2, 3\}$ are shown in Figure 3.1 with parameters $N = 200$ and $W = 1/40$.

From Eq. (3.22), we see that if one has an estimate of the time-frequency spectrum of \mathbf{X} available, then one can estimate the expansion coefficients a_l , for example using

the HRS estimator, Thomson [1993] proposed the estimators

$$\widehat{a}_l(f) \triangleq \frac{K}{N\alpha_l} \sum_{t=0}^{N-1} \widehat{S}_{\mathbf{X}}^H(t, f) A_l(t), \quad \forall f \in [-1/2, 1/2], \quad (3.25)$$

where $\widehat{S}_{\mathbf{X}}^H$ follows the form shown in Eq. (3.20).

3.6 Sliding-Window High-Resolution Spectrograms

As mentioned in Section 3.4, one of the drawbacks of using the HRS is that, if for a fixed frequency, the time-frequency spectrum varies rapidly with time, the number K of data tapers must be increased to capture this rapid variation. However, as K increases, the frequency resolution of the HRS decreases. Assume now that the time-frequency spectrum at frequency f varies slowly over a small time interval. In this case, in order to estimate the time-frequency spectrum in that particular time interval, a small K is sufficient to capture the time variation of the spectrum and the HRS would have a better frequency resolution comparing with when we use large K in the same time interval. To estimate the time-frequency spectrum in a small time interval, one can use the *sliding-window high-resolution spectrogram* (SWHRS) (The SWHRS was briefly explained in [Haykin and Thomson 1998]), defined as follows.

Let $\mathbf{X} \triangleq \{X_t\}_{t \in \mathbb{Z}}$ be a discrete-time zero-mean real-valued Gaussian nonstationary process. Let X_0, X_1, \dots, X_{N-1} be a realization of \mathbf{X} . Take the overlapping time blocks of length $B \ll N$, where the length of the overlap is arbitrary in general but in this thesis is taken to be $B - 1$. The blocks are indexed by the *base time* $b \in \{0, 1, \dots, N - B\}$. The SWHRS is defined by

$$\widehat{S}_{\mathbf{X}, b}(t, f) \triangleq \frac{B}{K} \left| \sum_{k=0}^{K-1} \nu_{t-b}^{(k)}(B, W) \sum_{n=0}^{B-1} X_{n+b}^{(b)} \nu_n^{(k)}(B, W) e^{-i2\pi f n} \right|^2, \quad (3.26)$$

where $t \in \{b, b+1, \dots, b+B-1\}$, and W , K , and the $\{\nu_t^{(k)}(B, W)\}_{t=0}^{B-1}$ are as in Section 3.4.

Due to the blocking, for each fixed f , the SWHRS produces more than one estimate of $S_{\mathbf{X}}(t, f)$ (one for each block in which t appears). One approach to deal with having many estimates of $S_{\mathbf{X}}(t, f)$ is to estimate $S_{\mathbf{X}}$ at only the “middle” time point of each block b , denoted by $t_b \triangleq b + \lceil \frac{B}{2} \rceil$. Thus, for $t \in \{\lceil \frac{B}{2} \rceil, \lceil \frac{B}{2} \rceil + 1, \dots, (N-1) - \lceil \frac{B}{2} \rceil\}$, the time-frequency spectrum at (t, f) is estimated by $\widehat{S}_{\mathbf{X}, b}(t_b, f)$, using block $b = t - \lceil \frac{B}{2} \rceil$. The SWHRS estimate at other pairs (t, f) , *i.e.*, pairs (t, f) having $t < \lceil \frac{B}{2} \rceil$ or $t > N - 1 - \lceil \frac{B}{2} \rceil$, which we refer to as pairs lying in the *time boundary regions* of the time-frequency plane, are considered to be unavailable and must be estimated by other means. In the next section, we consider a modification of the SWHRS at all (t, f) pairs having $t \in \{b, b+1, \dots, B+b-1\}$, and use it to estimate the time-frequency spectrum at pairs (t, f) lying in the time boundary regions.

3.7 The Modified Time-Frequency Spectrum Estimator

In this section, we develop a technique to estimate the time-frequency spectrum at (t, f) pairs lying in the time boundary regions of the time-frequency plane, using the SWHRS estimator. The technique we propose smooths the SWHRS estimate at all (t, f) pairs having $t \in \{b, b+1, \dots, B+b-1\}$ where B is as in Section 3.6, as well as estimating the time-frequency spectrum at pairs (t, f) lying in the time boundary regions.

Let $\mathbf{X} \triangleq \{X_t\}_{t \in \mathbb{Z}}$ be a discrete-time zero-mean real-valued Gaussian nonstationary process. Let $S_{\mathbf{X}, b}$ denote the time-frequency spectrum of \mathbf{X} in the b th block, *i.e.*, $S_{\mathbf{X}, b}(t, f) = S_{\mathbf{X}}(t, f)$ with t restricted so that $t \in \{b, b+1, \dots, b+B-1\}$ and $f \in [-1/2, 1/2]$. Assume that, at each fixed frequency f , $t \mapsto S_{\mathbf{X}, b}(t, f)$ can be well

approximated by the first two terms of its Taylor series expansion around the middle time point t_b :

$$S_{\mathbf{X},b}(t, f) \approx S_{\mathbf{X},b}(t_b, f) + S_{\mathbf{X},b}^{(1)}(t_b, f)(t - t_b), \quad (3.27)$$

where $S_{\mathbf{X},b}^{(1)}(t_b, f)$ denotes the time derivative² of $S_{\mathbf{X},b}$ evaluated at (t_b, f) .

Recall from Section 3.5 that we assumed the time-frequency spectrum of \mathbf{X} has the approximate expansion shown in Eq. (3.22). Here we assume that a similar expansion holds for each $S_{\mathbf{X},b}$, *i.e.*, we assume that for each block b ,

$$S_{\mathbf{X},b}(t, f) \approx \sum_{l=0}^{L_b} a_{l,b}(f) A_l(t - b), \quad (3.28)$$

where $a_{l,b}$ are the expansion coefficients in block b (see Section 3.5). Using the two representations of the time-frequency spectrum from Eqs. (3.27) and (3.28), we have for each block b

$$\sum_{l=0}^{L_b} a_{l,b}(f) A_l(t - b) \approx S_{\mathbf{X},b}(t_b, f) + S_{\mathbf{X},b}^{(1)}(t_b, f)(t - t_b).$$

Multiplying both sides of the above equation by $A_m(t - b)$ and summing over t in a block, we get

$$\sum_{t=b}^{b+B-1} A_m(t - b) \sum_{l=0}^{L_b} a_{l,b}(f) A_l(t - b) \approx \sum_{t=b}^{b+B-1} A_m(t - b) \left[S_{\mathbf{X},b}(t_b, f) + S_{\mathbf{X},b}^{(1)}(t_b, f)(t - t_b) \right].$$

Changing the order of the sum gives

$$\sum_{l=0}^{L_b} a_{l,b}(f) \sum_{t=b}^{b+B-1} A_m(t - b) A_l(t - b) \approx \sum_{t=b}^{b+B-1} A_m(t - b) \left[S_{\mathbf{X},b}(t_b, f) + S_{\mathbf{X},b}^{(1)}(t_b, f)(t - t_b) \right].$$

²We assume that \mathbf{X} arises from discrete sampling of a continuous-time process \mathbf{X}_c (see Appendix B), such that the time derivative of the time-frequency spectrum of \mathbf{X}_c exists. The *time derivative of the time-frequency spectrum of \mathbf{X}* is taken to mean an appropriate discrete sampling of the time-derivative of the time-frequency spectrum of \mathbf{X}_c .

Using the orthogonality property of the sequences A_l from Eq. (3.24), we obtain

$$B \cdot a_{l,b}(f) \approx S_{\mathbf{X},b}(t_b, f) \sum_{t=b}^{b+B-1} A_l(t-b) + S_{\mathbf{X},b}^{(1)}(t_b, f) \sum_{t=b}^{b+B-1} A_l(t-b)(t-t_b). \quad (3.29)$$

For $l = 0$, we obtain

$$B \cdot a_{0,b}(f) \approx S_{\mathbf{X},b}(t_b, f) \sum_{t=b}^{b+B-1} A_0(t-b) + S_{\mathbf{X},b}^{(1)}(t_b, f) \sum_{t=b}^{b+B-1} A_0(t-b)(t-t_b).$$

Since A_0 in each block is an even function of t , we have $\sum_{t=b}^{b+B-1} A_0(t-b)(t-t_b) = 0$ and therefore

$$S_{\mathbf{X},b}(t_b, f) \approx \frac{B a_{0,b}(f)}{\sum_{t=b}^{b+B-1} A_0(t-b)}. \quad (3.30)$$

Similarly, for $l = 1$, we obtain

$$B \cdot a_{1,b}(f) \approx S_{\mathbf{X},b}(t_b, f) \sum_{t=b}^{b+B-1} A_1(t-b) + S_{\mathbf{X},b}^{(1)}(t_b, f) \sum_{t=b}^{b+B-1} A_1(t-b)(t-t_b).$$

Since A_1 in each block is an odd function of t , we have $\sum_{t=b}^{b+B-1} A_1(t-b) = 0$ and therefore

$$S_{\mathbf{X},b}^{(1)}(t_b, f) \approx \frac{B a_{1,b}(f)}{\sum_{t=b}^{b+B-1} A_1(t-b)(t-t_b)}. \quad (3.31)$$

Now let X_0, X_1, \dots, X_{N-1} be a realization of \mathbf{X} . Block this sample and compute $\widehat{S_{\mathbf{X},b}}$ in each block, as explained in Section 3.6. The coefficients $a_{0,b}$ and $a_{1,b}$ can be estimated, as in Section 3.5, using the SWHRS estimate: For $l = 0, 1$,

$$\widehat{a}_{l,b}(f) = \frac{K}{B\alpha_l} \sum_{t=b}^{b+B-1} \widehat{S_{\mathbf{X},b}}(t, f) A_l(t-b).$$

Plugging these estimates into Eqs. (3.30) and (3.31) yields estimators of $S_{\mathbf{X},b}$ and

$S_{\mathbf{X},b}^{(1)}$ at the middle time point t_b . Explicitly, we define

$$\widehat{S_{\mathbf{X},b,M}}(t_b, f) \triangleq \frac{\frac{K}{\alpha_0} \sum_{t=b}^{b+B-1} \widehat{S_{\mathbf{X},b}}(t, f) A_0(t-b)}{\sum_{t=b}^{b+B-1} A_0(t-b)} \quad (3.32)$$

$$\widehat{S_{\mathbf{X},b,T}^{(1)}}(t_b, f) \triangleq \frac{\frac{K}{\alpha_1} \sum_{t=b}^{b+B-1} \widehat{S_{\mathbf{X},b}}(t, f) A_1(t-b)}{\sum_{t=b}^{b+B-1} A_1(t-b)(t-t_b)}. \quad (3.33)$$

We call the estimator $\widehat{S_{\mathbf{X},b,M}}$ the *modified time-frequency spectrum estimator* (MTFSE), and we call the estimator $\widehat{S_{\mathbf{X},b,T}^{(1)}}$ the *time-derivative of the time-frequency spectrum estimator* (TDTFSE).

3.7.1 Estimation of the Wold-Cramér Evolutionary Spectrum Near the Time Boundaries of the Time-Frequency Plane

As a result of blocking, the MTFSE and TDTFSE, defined in Eqs. (3.32) and (3.33), respectively, can be evaluated only at $t_b \in [\lceil \frac{B}{2} \rceil, (N-1) - \lceil \frac{B}{2} \rceil]$. In other words, the MTFSE and TDTFSE estimates are not available at times prior to the middle time point of the first block, t_0 , and after the middle time point of the last block, t_{N-B+1} . In this subsection, we describe a technique to estimate the time-frequency spectrum at (t, f) pairs lying in the time boundary regions.

Using the blockwise Taylor series expansion of the time-frequency spectrum of \mathbf{X} from Eq. (3.27), $S_{\mathbf{X}}$ can be estimated h units of time ahead by

$$\widehat{S_{\mathbf{X},b,P}}(t_b \pm h, f) \triangleq \widehat{S_{\mathbf{X},b,M}}(t_b, f) \pm h \widehat{S_{\mathbf{X},b,T}^{(1)}}(t_b, f), \quad (3.34)$$

where $h \in \{1, 2, \dots, \lceil \frac{B}{2} \rceil\}$. The final estimate of $S_{\mathbf{X}}(t, f)$ is then taken to be $\widehat{S_{\mathbf{X},b,M}}(t, f)$ from Eq. (3.32) for $t \in [\lceil \frac{B}{2} \rceil, (N-1) - \lceil \frac{B}{2} \rceil]$ and $\widehat{S_{\mathbf{X},b,P}}(t, f)$ from Eq. (3.34) for $t \in \{0, 1, \dots, \lceil \frac{B}{2} \rceil - 1\} \cup \{N - \lceil \frac{B}{2} \rceil, \dots, N - 1\}$. We refer to this “combined estimator” as the *boundary-corrected modified time-frequency spectrum estimate* (BCMTFSE).

In Section 3.9, we demonstrate the performance of the BCMTFSE in estimating the time-frequency spectra of simulated processes.

3.8 Means and Variances of MTFSE and TDMTFSE

In this section, we calculate the means and variances of the MTFSE and TDMTFSE. As special cases, we derive expressions for the means and variances of the estimates when \mathbf{X} is assumed to be a UMP or a stationary process. We also examine the means and variances of the estimates when \mathbf{X} is assumed to be a white noise process.

3.8.1 Expected Values of the MTFSE and TDMTFSE

Let $\mathbf{X} \triangleq \{X_t\}_{t \in \mathbb{Z}}$ be a discrete-time zero-mean real-valued Gaussian nonstationary process. Let X_0, X_1, \dots, X_{N-1} be a realization of \mathbf{X} . Taking the expected value of the MTFSE and TDMTFSE from Eqs. (3.32) and (3.33), for $b \in \{0, 1, 2, \dots, N - B\}$ and $f \in [-1/2, 1/2]$ we have

$$\mathbb{E}\{\widehat{S_{\mathbf{X},b,M}}(t_b, f)\} = \frac{K}{\alpha_0 \sum_{t=b}^{b+B-1} A_0(t-b)} \sum_{t=b}^{b+B-1} A_0(t-b) \mathbb{E}\{\widehat{S_{\mathbf{X},b}}(t, f)\}. \quad (3.35)$$

$$\mathbb{E}\{\widehat{S_{\mathbf{X},b,T}^{(1)}}(t_b, f)\} = \frac{K}{\alpha_1 \sum_{t=b}^{b+B-1} A_1(t-b)(t-t_b)} \sum_{t=b}^{b+B-1} A_1(t-b) \mathbb{E}\{\widehat{S_{\mathbf{X},b}}(t, f)\}, \quad (3.36)$$

where K is as in Section 3.4. It is clear from the above two equations that in order to determine the expected values of the MTFSE and TDMTFSE, we first must calculate the expected value of $\widehat{S_{\mathbf{X},b}}$. We have

$$\mathbb{E}\{\widehat{S_{\mathbf{X},b}}(t, f)\} = \mathbb{E} \left\{ \frac{B}{K} \left| \sum_{k=0}^{K-1} \nu_{t-b}^{(k)}(B, W) y_k^{(b)}(f) \right|^2 \right\}, \quad (3.37)$$

where W is as in Section 3.4 and

$$y_k^{(b)}(f) \triangleq \sum_{n=0}^{B-1} X_{n+b}^{(b)} \nu_n^{(k)}(B, W) e^{-i2\pi f n} \quad (3.38)$$

is the k th eigencoefficient for the b th block, where $b \in \{0, 1, \dots, N - B\}$. Following Eq. (3.37) we have

$$\mathbb{E}\{\widehat{S_{\mathbf{X}, b}}(t, f)\} = \frac{B}{K} \sum_{j, k=0}^{K-1} \nu_{t-b}^{(k)}(B, W) \nu_{t-b}^{(j)}(B, W) \mathbb{E}\left\{y_k^{(b)}(f) \overline{y_j^{(b)}(f)}\right\}. \quad (3.39)$$

Assume \mathbf{X} (not necessarily oscillatory) can be represented as in Eq. (3.3), *i.e.*,

$$X_t = \int_{-1/2}^{1/2} \Phi_t(f) dZ_{\mathbf{X}}(f), \quad \forall t \in \mathbb{Z}, \quad (3.40)$$

where $\{Z_{\mathbf{X}}(f)\}_{f \in [-1/2, 1/2]}$ is a complex-valued orthogonal-increment process associated with \mathbf{X} satisfying $\mathbb{E}\{dZ_{\mathbf{X}}(f) \overline{dZ_{\mathbf{X}}(f')}\} = S_{\mathbf{X}}(f) \delta(f - f') df$, where δ denotes the Dirac delta function. The family of functions $\{\Phi_t : [-1/2, 1/2] \rightarrow \mathbb{C}\}_{t \in \mathbb{Z}}$ are square-integrable with respect to $S_{\mathbf{X}}$ (see Section 3.2).

Substituting the expression for \mathbf{X} from Eq. (3.40) into Eq. (3.38) gives

$$\begin{aligned} y_k^{(b)}(f) &= \sum_{n=0}^{B-1} \int_{-1/2}^{1/2} \Phi_{n+b}(\eta) dZ_{\mathbf{X}}(\eta) \nu_n^{(k)}(B, W) e^{-i2\pi f n} \\ &= \int_{-1/2}^{1/2} dZ_{\mathbf{X}}(\eta) \sum_{n=0}^{B-1} \Phi_{n+b}(\eta) \nu_n^{(k)}(B, W) e^{-i2\pi f n}. \end{aligned} \quad (3.41)$$

As a result,

$$\begin{aligned} \mathbb{E}\left\{y_k^{(b)}(f) \overline{y_j^{(b)}(f)}\right\} &= \int_{-1/2}^{1/2} \int_{-1/2}^{1/2} \sum_{n, n'=0}^{B-1} \Phi_{n+b}(\eta) \overline{\Phi_{n'+b}(\eta')} \nu_n^{(k)} \nu_{n'}^{(j)} e^{-i2\pi f(n-n')} \mathbb{E}\{dZ_{\mathbf{X}}(\eta) \overline{dZ_{\mathbf{X}}(\eta')}\} \\ &= \int_{-1/2}^{1/2} S_{\mathbf{X}}(\eta) \sum_{n, n'=0}^{B-1} \Phi_{n+b}(\eta) \overline{\Phi_{n'+b}(\eta')} \nu_n^{(k)} \nu_{n'}^{(j)} e^{-i2\pi f(n-n')} d\eta, \end{aligned} \quad (3.42)$$

where we have written $\nu_n^{(k)} \equiv \nu_n^{(k)}(B, W)$ for brevity. Substituting Eq. (3.42) into Eq. (3.39) gives

$$\begin{aligned} \mathbb{E}\{\widehat{S_{\mathbf{X},b}}(t, f)\} &= \frac{B}{K} \sum_{j,k=0}^{K-1} \nu_{t-b}^{(k)} \nu_{t-b}^{(j)} \int_{-1/2}^{1/2} S_{\mathbf{X}}(\eta) \sum_{n,n'=0}^{B-1} \Phi_{n+b}(\eta) \overline{\Phi_{n'+b}(\eta)} \nu_n^{(k)} \nu_{n'}^{(j)} e^{-i2\pi f(n-n')} d\eta \\ &= \frac{B}{K} \int_{-1/2}^{1/2} S_{\mathbf{X}}(\eta) \left| \sum_{n=0}^{B-1} \Phi_{n+b}(\eta) e^{-i2\pi f n} \sum_{k=0}^{K-1} \nu_{t-b}^{(k)} \nu_n^{(k)} \right|^2 d\eta. \end{aligned} \quad (3.43)$$

Substituting Eq. (3.43) into Eq. (3.35), we obtain

$$\mathbb{E}\{\widehat{S_{\mathbf{X},b,M}}(t_b, f)\} = Q_0 \int_{-1/2}^{1/2} S_{\mathbf{X}}(\eta) \left[\sum_{t=b}^{b+B-1} A_0(t-b) \left| \sum_{n=0}^{B-1} \Phi_{n+b}(\eta) e^{-i2\pi f n} \sum_{k=0}^{K-1} \nu_{t-b}^{(k)} \nu_n^{(k)} \right|^2 \right] d\eta, \quad (3.44)$$

where

$$Q_0 \triangleq \frac{B}{\alpha_0 \sum_{t=b}^{b+B-1} A_0(t-b)}. \quad (3.45)$$

Similarly, substituting Eq. (3.43) into Eq. (3.36), we obtain

$$\mathbb{E}\{\widehat{S_{\mathbf{X},b,T}^{(1)}}(t_b, f)\} = Q_1 \int_{-1/2}^{1/2} S_{\mathbf{X}}(\eta) \left[\sum_{t=b}^{b+B-1} A_1(t-b) \left| \sum_{n=0}^{B-1} \Phi_{n+b}(\eta) e^{-i2\pi f n} \sum_{k=0}^{K-1} \nu_{t-b}^{(k)} \nu_n^{(k)} \right|^2 \right] d\eta, \quad (3.46)$$

where

$$Q_1 \triangleq \frac{B}{\alpha_1 \sum_{t=b}^{b+B-1} A_1(t-b)(t-t_b)}. \quad (3.47)$$

Uniformly modulated processes

Assume that $\mathbf{X} \triangleq \{X_t\}_{t \in \mathbb{Z}}$ is a UMP so that $X_t = C_t Y_t$ for all $t \in \mathbb{Z}$, where $\{C_t\}_{t \in \mathbb{Z}} \subset \mathbb{R}$ is a nonnegative sequence and $\mathbf{Y} \triangleq \{Y_t\}_{t \in \mathbb{Z}}$ is a zero-mean stationary process (as

described in Section 3.2) with spectrum $S_{\mathbf{Y}}$. In this case, $\Phi_t(f) = C_t e^{i2\pi ft}$ (see Section 3.2.1) can be substituted into Eqs. (3.44) and (3.46) to obtain

$$\mathbb{E}\{\widehat{S_{\mathbf{X},b,M}}(t_b, f)\} = Q_0 \int_{-1/2}^{1/2} S_{\mathbf{Y}}(\eta) \left[\sum_{t=b}^{b+B-1} A_0(t-b) \left| \sum_{n=0}^{B-1} C_{n+b} e^{-i2\pi(f-\eta)n} \sum_{k=0}^{K-1} \nu_{t-b}^{(k)} \nu_n^{(k)} \right|^2 \right] d\eta \quad (3.48)$$

and

$$\mathbb{E}\{\widehat{S_{\mathbf{X},b,T}^{(1)}}(t_b, f)\} = Q_1 \int_{-1/2}^{1/2} S_{\mathbf{Y}}(\eta) \left[\sum_{t=b}^{b+B-1} A_1(t-b) \left| \sum_{n=0}^{B-1} C_{n+b} e^{-i2\pi(f-\eta)n} \sum_{k=0}^{K-1} \nu_{t-b}^{(k)} \nu_n^{(k)} \right|^2 \right] d\eta, \quad (3.49)$$

where Q_0 and Q_1 are as in Eqs. (3.45) and (3.47) respectively. We note that Eq. (3.48) is computed for Example 1 in Section 3.9.1 where $\{C_t\}_{t \in \mathbb{Z}}$ is known.

Stationary processes

Assume now that \mathbf{X} is stationary, so that $\Phi_t(f) = e^{i2\pi ft}$ [Priestley 1981]. Starting with Eq. (3.43), we have

$$\begin{aligned} \mathbb{E}\{\widehat{S_{\mathbf{X},b}}(t, f)\} &= \frac{B}{K} \sum_{j,k=0}^{K-1} \nu_{t-b}^{(k)} \nu_{t-b}^{(j)} \int_{-1/2}^{1/2} S_{\mathbf{X}}(\eta) \sum_{n,n'=0}^{B-1} e^{i2\pi\eta(n+b)} e^{-i2\pi\eta(n'+b)} \nu_n^{(k)} \nu_{n'}^{(j)} e^{-i2\pi f(n-n')} d\eta \\ &= \frac{B}{K} \sum_{j,k=0}^{K-1} \nu_{t-b}^{(k)} \nu_{t-b}^{(j)} \int_{-1/2}^{1/2} S_{\mathbf{X}}(\eta) \sum_{n=0}^{B-1} \nu_n^{(k)} e^{-i2\pi n(f-\eta)} \sum_{n'=0}^{B-1} \nu_{n'}^{(j)} e^{i2\pi n'(f-\eta)} d\eta \\ &= \frac{B}{K} \sum_{j,k=0}^{K-1} \nu_{t-b}^{(k)} \nu_{t-b}^{(j)} \int_{-1/2}^{1/2} S_{\mathbf{X}}(\eta) V_k(f-\eta) \overline{V_j(f-\eta)} d\eta \\ &= \frac{B}{K} \int_{-1/2}^{1/2} S_{\mathbf{X}}(\eta) \sum_{k=0}^{K-1} \nu_{t-b}^{(k)} V_k(f-\eta) \sum_{j=0}^{K-1} \nu_{t-b}^{(j)} \overline{V_j(f-\eta)} d\eta \\ &= \frac{B}{K} \int_{-1/2}^{1/2} S_{\mathbf{X}}(\eta) \left| \sum_{k=0}^{K-1} \nu_{t-b}^{(k)} V_k(f-\eta) \right|^2 d\eta. \end{aligned} \quad (3.50)$$

In the above, we have used the fact that (see Appendix A)

$$V_k(f) \equiv V_k(B, W; f) = \sum_{t=0}^{B-1} \nu_t^{(k)} e^{-i2\pi ft}.$$

Following Eqs. (3.35) and (3.36) and for Q_0 and Q_1 following Eqs. (3.45) and (3.47) we have

$$\mathbb{E}\{\widehat{S_{\mathbf{X},b,M}}(t_b, f)\} = Q_0 \int_{-1/2}^{1/2} S_{\mathbf{X}}(\eta) \left[\sum_{t=b}^{b+B-1} A_0(t-b) \left| \sum_{k=0}^{K-1} \nu_{t-b}^{(k)} V_k(f-\eta) \right|^2 \right] d\eta. \quad (3.51)$$

and

$$\mathbb{E}\{\widehat{S_{\mathbf{X},b,T}^{(1)}}(t_b, f)\} = Q_1 \int_{-1/2}^{1/2} S_{\mathbf{X}}(\eta) \left[\sum_{t=b}^{b+B-1} A_1(t-b) \left| \sum_{k=0}^{K-1} \nu_{t-b}^{(k)} V_k(f-\eta) \right|^2 \right] d\eta. \quad (3.52)$$

White noise processes

Assume now that \mathbf{X} is a white noise process with variance $\sigma_{\mathbf{X}}^2$. As a result, recalling Eq. (3.51) and using the fact that $S_{\mathbf{X}} \equiv \sigma_{\mathbf{X}}^2$, we get

$$\begin{aligned} \mathbb{E}\{\widehat{S_{\mathbf{X},b,M}}(t_b, f)\} &= Q_0 \sigma_{\mathbf{X}}^2 \int_{-1/2}^{1/2} \sum_{t=b}^{b+B-1} A_0(t-b) \sum_{k,j=0}^{K-1} \nu_{t-b}^{(k)} \nu_{t-b}^{(j)} V_k(f-\eta) \overline{V_j(f-\eta)} d\eta \\ &= Q_0 \sigma_{\mathbf{X}}^2 \sum_{t=b}^{b+B-1} A_0(t-b) \sum_{k,j=0}^{K-1} \nu_{t-b}^{(k)} \nu_{t-b}^{(j)} \int_{-1/2}^{1/2} V_k(f-\eta) \overline{V_j(f-\eta)} d\eta. \end{aligned}$$

Using the orthogonality property of the function V_k (Eq. (A.13) in Appendix A), we have

$$\mathbb{E}\{\widehat{S_{\mathbf{X},b,M}}(t_b, f)\} = Q_0 \sigma_{\mathbf{X}}^2 \sum_{t=b}^{b+B-1} A_0(t-b) \sum_{k=0}^{K-1} \nu_{t-b}^{(k)} \nu_{t-b}^{(k)}. \quad (3.53)$$

Further, using the following property of the DPSS (see the appendix in [Thomson 1990]),

$$\sum_{k=0}^{N-1} \lambda_k(N, W) \nu_n^{(k)}(N, W) \nu_m^{(k)}(N, W) = \frac{\sin 2\pi W(n-m)}{\pi(n-m)}.$$

Recall from Appendix A that the first $\lfloor 2NW \rfloor - 1$ eigenvalues $\lambda_k(N, W)$ are approximately one. If we assume $K = \lfloor 2NW \rfloor$, we have

$$\sum_{k=0}^{K-1} \nu_n^{(k)}(N, W) \nu_m^{(k)}(N, W) \approx \frac{\sin 2\pi W(n-m)}{\pi(n-m)}. \quad (3.54)$$

Note that when $n = m$, the sum in Eq. (3.54) is approximately $2W$ by l'Hôpital's rule. Using this approximation in Eq. (3.53), we have

$$\begin{aligned} \mathbb{E}\{\widehat{S_{\mathbf{X},b,M}}(t_b, f)\} &\approx Q_0 \sigma_{\mathbf{X}}^2 2W \sum_{t=b}^{b+B-1} A_0(t-b) \\ &= \frac{B \sigma_{\mathbf{X}}^2 2W \sum_{t=b}^{b+B-1} A_0(t-b)}{\alpha_0 \sum_{t=b}^{b+B-1} A_0(t-b)} \\ &= \frac{B \sigma_{\mathbf{X}}^2 2W}{\alpha_0}. \end{aligned}$$

Since $\alpha_0 \approx 2BW$ (see Section 3.5), we obtain $\mathbb{E}\{\widehat{S_{\mathbf{X},b,M}}(t_b, f)\} \approx \sigma_{\mathbf{X}}^2$, which shows that the MTFSE is approximately unbiased when \mathbf{X} is a white noise process.

Similarly, recalling Eq. (3.52) and using the fact that $S_{\mathbf{X}} \equiv \sigma_{\mathbf{X}}^2$ we get

$$\begin{aligned}
\mathbb{E}\{\widehat{S_{\mathbf{X},b,T}^{(1)}}(t_b, f)\} &= Q_1 \sigma_{\mathbf{X}}^2 \int_{-1/2}^{1/2} \sum_{t=b}^{b+B-1} A_1(t-b) \sum_{k,j=0}^{K-1} \nu_{t-b}^{(k)} \nu_{t-b}^{(j)} V_k(f-\eta) \overline{V_j(f-\eta)} d\eta \\
&= Q_1 \sigma_{\mathbf{X}}^2 \sum_{t=b}^{b+B-1} A_1(t-b) \sum_{k,j=0}^{K-1} \nu_{t-b}^{(k)} \nu_{t-b}^{(j)} \int_{-1/2}^{1/2} V_k(f-\eta) \overline{V_j(f-\eta)} d\eta \\
&= Q_1 \sigma_{\mathbf{X}}^2 \sum_{t=b}^{b+B-1} A_1(t-b) \sum_{k=0}^{K-1} \nu_{t-b}^{(k)} \nu_{t-b}^{(k)} \\
&\approx Q_1 \sigma_{\mathbf{X}}^2 2W \sum_{t=b}^{b+B-1} A_1(t-b).
\end{aligned}$$

Since A_1 is an odd function of t , $\sum_{t=0}^{B-1} A_1(t) = 0$, and therefore we have $\mathbb{E}\{\widehat{S_{\mathbf{X},b,T}^{(1)}}(t_b, f)\} = 0$. This result validates $\widehat{S_{\mathbf{X},b,T}^{(1)}}$ as an estimator of the time-derivative of the time-frequency spectrum, since the time-frequency spectrum of white noise is constant in t .

3.8.2 Variances of the MTFSE and TDMTFSE

Let $\mathbf{X} \triangleq \{X_t\}_{t \in \mathbb{Z}}$ be a discrete-time zero-mean real-valued Gaussian nonstationary process having representation of the form shown in Eq. (3.40), and let X_0, X_1, \dots, X_{N-1} be a realization of \mathbf{X} . Taking the variances of the MTFSE and the TDMTFSE from Eqs. (3.32) and (3.33) respectively, and for $b \in \{0, 1, \dots, N-B\}$ and $f \in [-1/2, 1/2]$, we have

$$\begin{aligned}
\text{Var}\{\widehat{S_{\mathbf{X},b,M}}(t_b, f)\} &= \mathbb{E}\left\{\left|\widehat{S_{\mathbf{X},b,M}}(t_b, f)\right|^2\right\} - \left|\mathbb{E}\left\{\widehat{S_{\mathbf{X},b,M}}(t_b, f)\right\}\right|^2 \\
&= Q_3 \sum_{t,t'=b}^{b+B-1} A_0(t-b) A_0(t'-b) \text{Cov}\{\widehat{S_{\mathbf{X},b}}(t, f), \widehat{S_{\mathbf{X},b}}(t', f)\},
\end{aligned} \tag{3.55}$$

and

$$\begin{aligned} \text{Var} \left\{ \widehat{S_{\mathbf{X},b,T}^{(1)}}(t_b, f) \right\} &= \mathbb{E} \left\{ \left| \widehat{S_{\mathbf{X},b,T}^{(1)}}(t_b, f) \right|^2 \right\} - \left| \mathbb{E} \left\{ \widehat{S_{\mathbf{X},b,T}^{(1)}}(t_b, f) \right\} \right|^2 \\ &= Q_4 \sum_{t,t'=b}^{b+B-1} A_1(t-b)A_1(t'-b) \text{Cov} \{ \widehat{S_{\mathbf{X},b}(t, f)}, \widehat{S_{\mathbf{X},b}(t', f)} \}. \end{aligned} \quad (3.56)$$

In the above,

$$\text{Cov} \left\{ \widehat{S_{\mathbf{X},b}(t, f)}, \widehat{S_{\mathbf{X},b}(t', f)} \right\} = \mathbb{E} \left\{ \widehat{S_{\mathbf{X},b}(t, f)} \widehat{S_{\mathbf{X},b}(t', f)} \right\} - \mathbb{E} \left\{ \widehat{S_{\mathbf{X},b}(t, f)} \right\} \mathbb{E} \left\{ \widehat{S_{\mathbf{X},b}(t', f)} \right\}, \quad (3.57)$$

as usual, and we have defined

$$Q_3 \triangleq \left(\frac{K}{\alpha_0 \sum_{t=b}^{b+B-1} A_0(t-b)} \right)^2 \quad \text{and} \quad Q_4 \triangleq \left(\frac{K}{\alpha_1 \sum_{t=b}^{b+B-1} A_1(t-b)(t-t_b)} \right)^2.$$

In order to calculate the variances of the MTFSE and TDMTFSE, we obviously have to calculate the covariance functions in Eq. (3.57). To calculate the first part of Eq. (3.57) we recall Eq. (3.37); and for $t, t' \in \{b, b+1, \dots, B+b-1\}$ and $f \in [-1/2, 1/2]$ we obtain

$$\mathbb{E} \left\{ \widehat{S_{\mathbf{X},b}(t, f)} \widehat{S_{\mathbf{X},b}(t', f)} \right\} = \frac{B^2}{K^2} \sum_{k,j,k',j'=0}^{K-1} \nu_{t-b}^{(k)} \nu_{t-b}^{(j)} \nu_{t'-b}^{(k')} \nu_{t'-b}^{(j')} \mathbb{E} \left\{ \overline{y_j^{(b)}(f)} y_k^{(b)}(f) y_{j'}^{(b)}(f) \overline{y_{k'}^{(b)}(f)} \right\}.$$

Since \mathbf{X} is assumed to be Gaussian, for $j, k, j', k' \in \{0, 1, \dots, K-1\}$ [Miller 1974] we have

$$\begin{aligned} \mathbb{E} \left\{ \overline{y_j^{(b)}(f)} y_k^{(b)}(f) y_{j'}^{(b)}(f) \overline{y_{k'}^{(b)}(f)} \right\} &= \mathbb{E} \left\{ y_k^{(b)}(f) \overline{y_j^{(b)}(f)} \right\} \mathbb{E} \left\{ y_{j'}^{(b)}(f) \overline{y_{k'}^{(b)}(f)} \right\} \\ &\quad + \mathbb{E} \left\{ \overline{y_j^{(b)}(f)} y_{j'}^{(b)}(f) \right\} \mathbb{E} \left\{ y_k^{(b)}(f) \overline{y_{k'}^{(b)}(f)} \right\}, \end{aligned}$$

and therefore

$$\begin{aligned} \mathbb{E} \left\{ \widehat{S}_{\mathbf{X},b}(t, f) \widehat{S}_{\mathbf{X},b}(t', f) \right\} &= \frac{B^2}{K^2} \sum_{k,j,k',j'=0}^{K-1} \nu_{t-b}^{(k)} \nu_{t-b}^{(j)} \nu_{t'-b}^{(k')} \nu_{t'-b}^{(j')} \mathbb{E} \left\{ y_k^{(b)}(f) \overline{y_j^{(b)}(f)} \right\} \mathbb{E} \left\{ y_{j'}^{(b)}(f) \overline{y_{k'}^{(b)}(f)} \right\} \\ &+ \frac{B^2}{K^2} \sum_{k,j,k',j'=0}^{K-1} \nu_{t-b}^{(k)} \nu_{t-b}^{(j)} \nu_{t'-b}^{(k')} \nu_{t'-b}^{(j')} \mathbb{E} \left\{ \overline{y_j^{(b)}(f)} y_{j'}^{(b)}(f) \right\} \mathbb{E} \left\{ y_k^{(b)}(f) \overline{y_{k'}^{(b)}(f)} \right\}. \end{aligned} \quad (3.58)$$

To calculate the second part of Eq. (3.57), we recall Eq. (3.37) and obtain

$$\begin{aligned} \mathbb{E} \{ \widehat{S}_{\mathbf{X},b}(t, f) \} \mathbb{E} \{ \widehat{S}_{\mathbf{X},b}(t', f) \} &= \frac{B^2}{K^2} \sum_{k,j,k',j'=0}^{K-1} \nu_{t-b}^{(k)} \nu_{t-b}^{(j)} \nu_{t'-b}^{(k')} \nu_{t'-b}^{(j')} \\ &\times \mathbb{E} \left\{ y_k^{(b)}(f) \overline{y_j^{(b)}(f)} \right\} \mathbb{E} \left\{ y_{j'}^{(b)}(f) \overline{y_{k'}^{(b)}(f)} \right\}. \end{aligned} \quad (3.59)$$

Substituting Eqs. (3.58) and (3.59) into Eq. (3.57) gives

$$\begin{aligned} \text{Cov} \left\{ \widehat{S}_{\mathbf{X},b}(t, f), \widehat{S}_{\mathbf{X},b}(t', f) \right\} &= \frac{B^2}{K^2} \sum_{k,j,k',j'=0}^{K-1} \nu_{t-b}^{(k)} \nu_{t-b}^{(j)} \nu_{t'-b}^{(k')} \nu_{t'-b}^{(j')} \\ &\times \mathbb{E} \left\{ y_{j'}^{(b)}(f) \overline{y_j^{(b)}(f)} \right\} \mathbb{E} \left\{ y_k^{(b)}(f) \overline{y_{k'}^{(b)}(f)} \right\}. \end{aligned} \quad (3.60)$$

Using the representation of \mathbf{X} from Eq. (3.40) and recalling Eq. (3.38) and for $\eta, \eta', \gamma, \gamma' \in [-1/2, 1/2]$, we have

$$\begin{aligned} \mathbb{E} \left\{ y_{j'}^{(b)}(f) \overline{y_j^{(b)}(f)} \right\} &= \int_{-1/2}^{1/2} \int_{-1/2}^{1/2} \sum_{n,n'=0}^{B-1} \Phi_{n+b}(\eta) \overline{\Phi_{n'+b}(\eta')} \nu_n^{(j')} \nu_{n'}^{(j)} e^{-i2\pi f(n-n')} \mathbb{E} \{ dZ_{\mathbf{X}}(\eta) \overline{dZ_{\mathbf{X}}(\eta')} \} \\ &= \int_{-1/2}^{1/2} S_{\mathbf{X}}(\eta) \sum_{n,n'=0}^{B-1} \Phi_{n+b}(\eta) \overline{\Phi_{n'+b}(\eta')} \nu_n^{(j')} \nu_{n'}^{(j)} e^{-i2\pi f(n-n')} d\eta. \end{aligned} \quad (3.61)$$

Similarly,

$$\begin{aligned}
\mathbb{E} \left\{ y_k^{(b)}(f) \overline{y_{k'}^{(b)}(f)} \right\} &= \int_{-1/2}^{1/2} \int_{-1/2}^{1/2} \sum_{l, l'=0}^{B-1} \Phi_{l+b}(\gamma) \overline{\Phi_{l'+b}(\gamma')} \nu_l^{(k)} \nu_{l'}^{(k')} e^{-i2\pi f(l-l')} \mathbb{E} \{ dZ_{\mathbf{X}}(\gamma) \overline{dZ_{\mathbf{X}}(\gamma')} \} \\
&= \int_{-1/2}^{1/2} S_{\mathbf{X}}(\gamma) \sum_{l, l'=0}^{B-1} \Phi_{l+b}(\gamma) \overline{\Phi_{l'+b}(\gamma')} \nu_l^{(k)} \nu_{l'}^{(k')} e^{-i2\pi f(l-l')} d\gamma. \quad (3.62)
\end{aligned}$$

Substituting Eqs. (3.61) and (3.62) into Eq. (3.60) gives

$$\begin{aligned}
\text{Cov} \left\{ \widehat{S_{\mathbf{X},b}}(t, f), \widehat{S_{\mathbf{X},b}}(t', f) \right\} &= \frac{B^2}{K^2} \int_{-1/2}^{1/2} \int_{-1/2}^{1/2} S_{\mathbf{X}}(\eta) S_{\mathbf{X}}(\gamma) \Gamma_1^{(b)}(\eta, f, t') \Gamma_2^{(b)}(\eta, f, t) \\
&\quad \times \Gamma_3^{(b)}(\gamma, f, t) \Gamma_4^{(b)}(\gamma, f, t') d\eta d\gamma, \quad (3.63)
\end{aligned}$$

where

$$\begin{aligned}
\Gamma_1^{(b)}(\eta, f, t') &\triangleq \sum_{n=0}^{B-1} \Phi_{n+b}(\eta) e^{-i2\pi f n} \sum_{j'=0}^{K-1} \nu_n^{(j')} \nu_{t'-b}^{(j')}, \\
\Gamma_2^{(b)}(\eta, f, t) &\triangleq \sum_{n'=0}^{B-1} \overline{\Phi_{n'+b}(\eta)} e^{i2\pi f n'} \sum_{j=0}^{K-1} \nu_{n'}^{(j)} \nu_{t-b}^{(j)}, \\
\Gamma_3^{(b)}(\gamma, f, t) &\triangleq \sum_{l=0}^{B-1} \Phi_{l+b}(\gamma) e^{-i2\pi f l} \sum_{k=0}^{K-1} \nu_l^{(k)} \nu_{t-b}^{(k)}, \quad \text{and} \\
\Gamma_4^{(b)}(\gamma, f, t') &\triangleq \sum_{l'=0}^{B-1} \overline{\Phi_{l'+b}(\gamma)} e^{i2\pi f l'} \sum_{k'=0}^{K-1} \nu_{l'}^{(k')} \nu_{t'-b}^{(k')},
\end{aligned}$$

Substituting Eq. (3.63) into Eq. (3.55) gives

$$\begin{aligned}
\text{Var} \left\{ \widehat{S_{\mathbf{X},b,M}}(t_b, f) \right\} &= \left(\frac{B}{\alpha_0 \sum_{t=b}^{b+B-1} A_0(t-b)} \right)^2 \\
&\quad \times \int_{-1/2}^{1/2} \int_{-1/2}^{1/2} S_{\mathbf{X}}(\eta) S_{\mathbf{X}}(\gamma) \Gamma^{(b)}(\eta, \gamma, f) d\eta d\gamma, \quad (3.64)
\end{aligned}$$

where we have defined

$$\Gamma^{(b)}(\eta, \gamma, f) \triangleq \sum_{t, t'=b}^{b+B-1} A_0(t-b)A_0(t'-b)\Gamma_1^{(b)}(\eta, f, t')\Gamma_2^{(b)}(\eta, f, t)\Gamma_3^{(b)}(\gamma, f, t)\Gamma_4^{(b)}(\gamma, f, t'). \quad (3.65)$$

Similarly, substituting Eq. (3.63) into Eq. (3.56) gives

$$\begin{aligned} \text{Var} \left\{ \widehat{S_{\mathbf{X}, b, T}^{(1)}}(t_b, f) \right\} &= \left(\frac{B}{\alpha_1 \sum_{t=b}^{b+B-1} A_1(t-b)(t-t_b)} \right)^2 \\ &\times \int_{-1/2}^{1/2} \int_{-1/2}^{1/2} S_{\mathbf{X}}(\eta)S_{\mathbf{X}}(\gamma)\Theta^{(b)}(\eta, \gamma, f) \, d\eta \, d\gamma, \end{aligned} \quad (3.66)$$

where we have defined

$$\Theta^{(b)}(\eta, \gamma, f) \triangleq \sum_{t, t'=b}^{b+B-1} A_1(t-b)A_1(t'-b)\Gamma_1^{(b)}(\eta, f, t')\Gamma_2^{(b)}(\eta, f, t)\Gamma_3^{(b)}(\gamma, f, t)\Gamma_4^{(b)}(\gamma, f, t'). \quad (3.67)$$

Uniformly modulated processes

Assume that \mathbf{X} is a UMP, so that $X_t = C_t Y_t$ for all $t \in \mathbb{Z}$, where $\{C_t\}_{t \in \mathbb{Z}} \subset \mathbb{R}$ (as described in Section 3.2) is a nonnegative sequence and $\mathbf{Y} = \{Y_t\}_{t \in \mathbb{Z}}$ is a zero-mean stationary process with spectrum $S_{\mathbf{Y}}$. In this case, $\Phi_t(f) = C_t e^{i2\pi f t}$ (see Section 3.2.1) can be substituted into Eqs. (3.64) and (3.66) to get

$$\begin{aligned} \text{Var} \left\{ \widehat{S_{\mathbf{X}, b, M}}(t_b, f) \right\} &= \left(\frac{B}{\alpha_0 \sum_{t=b}^{b+B-1} A_0(t-b)} \right)^2 \\ &\times \int_{-1/2}^{1/2} \int_{-1/2}^{1/2} S_{\mathbf{Y}}(\eta)S_{\mathbf{Y}}(\gamma)\Gamma^{(b)}(\eta, \gamma, f) \, d\eta \, d\gamma, \end{aligned}$$

and

$$\begin{aligned} \text{Var} \left\{ \widehat{S_{\mathbf{X},b,T}^{(1)}}(t_b, f) \right\} &= \left(\frac{B}{\alpha_1 \sum_{t=b}^{b+B-1} A_1(t-b)(t-t_b)} \right)^2 \\ &\times \int_{-1/2}^{1/2} \int_{-1/2}^{1/2} S_{\mathbf{Y}}(\eta) S_{\mathbf{Y}}(\gamma) \Theta^{(b)}(\eta, \gamma, f) d\eta d\gamma, \end{aligned}$$

where $\Gamma^{(b)}(\eta, \gamma, f)$ and $\Theta^{(b)}(\eta, \gamma, f)$ are as in Eqs. (3.65) and (3.67), respectively. To calculate $\Gamma^{(b)}(\eta, \gamma, f)$ and $\Theta^{(b)}(\eta, \gamma, f)$ for a UMP it remains to compute

$$\begin{aligned} \Gamma_1^{(b)}(\eta, f, t') &= \sum_{n=0}^{B-1} C_{n+b} e^{-i2\pi(f-\eta)n} \sum_{j'=0}^{K-1} \nu_n^{(j')} \nu_{t'-b}^{(j')}, \\ \Gamma_2^{(b)}(\eta, f, t) &= \sum_{n'=0}^{B-1} C_{n'+b} e^{i2\pi(f-\eta)n'} \sum_{j=0}^{K-1} \nu_{n'}^{(j)} \nu_{t-b}^{(j)}, \\ \Gamma_3^{(b)}(\gamma, f, t) &= \sum_{l=0}^{B-1} C_{l+b} e^{-i2\pi(f-\gamma)l} \sum_{k=0}^{K-1} \nu_l^{(k)} \nu_{t-b}^{(k)}, \quad \text{and} \\ \Gamma_4^{(b)}(\gamma, f, t') &= \sum_{l'=0}^{B-1} C_{l'+b} e^{i2\pi(f-\gamma)l'} \sum_{k'=0}^{K-1} \nu_{l'}^{(k')} \nu_{t'-b}^{(k')}. \end{aligned}$$

Stationary processes

Assuming that \mathbf{X} is stationary, the variances of the MTFSE and TDMTFSE follow Eqs. (3.64) and (3.66), respectively. In this case $\Phi_t(f) = e^{i2\pi ft}$ and from the definitions of $\Gamma_1^{(b)}$, $\Gamma_2^{(b)}$, $\Gamma_3^{(b)}$, and $\Gamma_4^{(b)}$ in Eqs. (3.65) and (3.67) we see that

$$\begin{aligned} \Gamma_1^{(b)}(\eta, f, t') &= \sum_{n=0}^{B-1} e^{-i2\pi(f-\eta)n} \sum_{j'=0}^{K-1} \nu_n^{(j')} \nu_{t'-b}^{(j')} \\ &= \sum_{j'=0}^{K-1} \nu_{t'-b}^{(j')} \sum_{n=0}^{B-1} \nu_n^{(j')} e^{-i2\pi(f-\eta)n} \\ &= \sum_{j'=0}^{K-1} \nu_{t'-b}^{(j')} V_{j'}(f-\eta), \end{aligned} \tag{3.68}$$

$$\begin{aligned}
\Gamma_2^{(b)}(\eta, f, t) &= \sum_{n'=0}^{B-1} e^{i2\pi(f-\eta)n'} \sum_{j=0}^{K-1} \nu_{n'}^{(j)} \nu_{t-b}^{(j)} \\
&= \sum_{j=0}^{K-1} \nu_{t-b}^{(j)} \sum_{n'=0}^{B-1} \nu_{n'}^{(j)} e^{i2\pi(f-\eta)n'} \\
&= \sum_{j=0}^{K-1} \nu_{t-b}^{(j)} \overline{V_j(f-\eta)},
\end{aligned} \tag{3.69}$$

$$\begin{aligned}
\Gamma_3^{(b)}(\gamma, f, t) &= \sum_{l=0}^{B-1} e^{-i2\pi(f-\gamma)l} \sum_{k=0}^{K-1} \nu_l^{(k)} \nu_{t-b}^{(k)} \\
&= \sum_{k=0}^{K-1} \nu_{t-b}^{(k)} \sum_{l=0}^{B-1} \nu_l^{(k)} e^{-i2\pi(f-\gamma)l} \\
&= \sum_{k=0}^{K-1} \nu_{t-b}^{(k)} V_k(f-\gamma),
\end{aligned} \tag{3.70}$$

and

$$\begin{aligned}
\Gamma_4^{(b)}(\gamma, f, t') &= \sum_{l'=0}^{B-1} e^{i2\pi(f-\gamma)l'} \sum_{k'=0}^{K-1} \nu_{l'}^{(k')} \nu_{t'-b}^{(k')} \\
&= \sum_{k'=0}^{K-1} \nu_{t'-b}^{(k')} \sum_{l'=0}^{B-1} \nu_{l'}^{(k')} e^{i2\pi(f-\gamma)l'} \\
&= \sum_{k'=0}^{K-1} \nu_{t'-b}^{(k')} \overline{V_{k'}(f-\gamma)}.
\end{aligned} \tag{3.71}$$

White noise processes

Assume now that \mathbf{X} is a white noise process with variance $\sigma_{\mathbf{X}}^2$. Recalling Eq. (3.64) and using the fact that $S_{\mathbf{X}} \equiv \sigma_{\mathbf{X}}^2$, we have

$$\text{Var} \left\{ \widehat{S_{\mathbf{X},b,M}}(t_b, f) \right\} = \left(\frac{B\sigma_{\mathbf{X}}^2}{\alpha_0 \sum_{t=b}^{b+B-1} A_0(t-b)} \right)^2 \int_{-1/2}^{1/2} \int_{-1/2}^{1/2} \Gamma^{(b)}(\eta, \gamma, f) d\eta d\gamma. \tag{3.72}$$

Recalling Eq. (3.65) and using Eqs.(3.68), (3.69), (3.70), and (3.71) from the stationary case, we have

$$\begin{aligned} \int_{-1/2}^{1/2} \int_{-1/2}^{1/2} \Gamma^{(b)}(\eta, \gamma, f) d\eta d\gamma &= \sum_{t,t'=b}^{b+B-1} A_0(t-b)A_0(t'-b) \\ &\times \sum_{k,j,k',j'=0}^{K-1} \nu_{t-b}^{(k)} \nu_{t-b}^{(j)} \nu_{t'-b}^{(k')} \nu_{t'-b}^{(j')} \delta_{k,k'} \delta_{j,j'}, \end{aligned}$$

where we have used the fact that

$$\begin{aligned} \int_{-1/2}^{1/2} V_k(f-\gamma) \overline{V_{k'}(f-\gamma)} d\gamma &= \delta_{k,k'} \\ \int_{-1/2}^{1/2} V_{j'}(f-\eta) \overline{V_j(f-\eta)} d\eta &= \delta_{j,j'}. \end{aligned}$$

As a result, we have

$$\begin{aligned} \int_{-1/2}^{1/2} \int_{-1/2}^{1/2} \Gamma^{(b)}(\eta, \gamma, f) d\eta d\gamma &= \sum_{t,t'=b}^{b+B-1} A_0(t-b)A_0(t'-b) \sum_{k,j=0}^{K-1} \nu_{t-b}^{(k)} \nu_{t-b}^{(j)} \nu_{t'-b}^{(k)} \nu_{t'-b}^{(j)} \\ &= \sum_{t,t'=b}^{b+B-1} A_0(t-b)A_0(t'-b) \sum_{k=0}^{K-1} \nu_{t-b}^{(k)} \nu_{t'-b}^{(k)} \sum_{j=0}^{K-1} \nu_{t-b}^{(j)} \nu_{t'-b}^{(j)}. \end{aligned}$$

Using the approximation from Eq. (3.54),

$$\begin{aligned} \int_{-1/2}^{1/2} \int_{-1/2}^{1/2} \Gamma^{(b)}(\eta, \gamma, f) d\eta d\gamma &\approx \sum_{t,t'=b}^{b+B-1} A_0(t-b)A_0(t'-b) \left[\frac{\sin(2\pi W(t-t'))}{\pi(t-t')} \right]^2 \\ &= \sum_{t=b}^{b+B-1} A_0(t-b) \sum_{t'=b}^{b+B-1} A_0(t'-b) \left[\frac{\sin(2\pi W(t-t'))}{\pi(t-t')} \right]^2. \end{aligned}$$

Recalling Eqs. (3.23) and (3.24) from Section 3.5, we have

$$\int_{-1/2}^{1/2} \int_{-1/2}^{1/2} \Gamma^{(b)}(\eta, \gamma, f) d\eta d\gamma \approx \sum_{t=b}^{b+B-1} A_0(t-b) \left(\frac{\alpha_0}{B} A_0(t-b) \right) = \frac{\alpha_0}{B} B = \alpha_0.$$

As a result, substituting the above into Eq. (3.72) we get

$$\text{Var} \left\{ \widehat{S_{\mathbf{X},b,M}}(t_b, f) \right\} \approx \left(\frac{B\sigma_{\mathbf{X}}^2}{\alpha_0 \sum_{t=b}^{b+B-1} A_0(t-b)} \right)^2 \alpha_0 = \frac{B^2\sigma_{\mathbf{X}}^4}{\alpha_0 \left[\sum_{t=b}^{b+B-1} A_0(t-b) \right]^2}.$$

Note that since A_0 is approximately constant for $t \in \{0, 1, \dots, B-1\}$, $\sum_{t=b}^{b+B-1} A_0(t-b) = O(B)$ and since $\alpha_0 \approx 2BW$, $\text{Var} \left\{ \widehat{S_{\mathbf{X},b,M}}(t_b, f) \right\} = O(B^{-1})$. In other words, as the block size B increases, the variance of the time-frequency spectrum estimate will decrease.

To calculate the variance of the TDMTFSE, using Eq. (3.66) and the fact that $S_{\mathbf{X}} \equiv \sigma_{\mathbf{X}}^2$, we have

$$\text{Var} \left\{ \widehat{S_{\mathbf{X},b,T}^{(1)}}(t_b, f) \right\} = \left(\frac{B\sigma_{\mathbf{X}}^2}{\alpha_1 \sum_{t=b}^{b+B-1} A_1(t)(t-t_b)} \right)^2 \int_{-1/2}^{1/2} \int_{-1/2}^{1/2} \Theta^{(b)}(\eta, \gamma, f) d\eta d\gamma, \quad (3.73)$$

where

$$\int_{-1/2}^{1/2} \int_{-1/2}^{1/2} \Theta^{(b)}(\eta, \gamma, f) d\eta d\gamma = \sum_{t,t'=b}^{b+B-1} A_1(t-b)A_1(t'-b) \sum_{k,j,k',j'=0}^{K-1} \nu_t^{(k)} \nu_{t'}^{(j)} \nu_{t'}^{(k')} \nu_t^{(j')} \delta_{k,k'} \delta_{j,j'}.$$

Similar to the calculation of the variance of the MTFSE, we have

$$\begin{aligned} \int_{-1/2}^{1/2} \int_{-1/2}^{1/2} \Theta^{(b)}(\eta, \gamma, f) d\eta d\gamma &= \sum_{t,t'=b}^{b+B-1} A_1(t-b)A_1(t'-b) \sum_{k=0}^{K-1} \nu_t^{(k)} \nu_{t'}^{(k)} \sum_j \nu_t^{(j)} \nu_{t'}^{(j)} \\ &\approx \sum_{t,t'=b}^{b+B-1} A_1(t-b)A_1(t'-b) \left[\frac{\sin(2\pi W(t-t'))}{\pi(t-t')} \right]^2 \\ &= \sum_{t=b}^{b+B-1} A_1(t-b) \sum_{t'=b}^{b+B-1} A_1(t'-b) \left[\frac{\sin(2\pi W(t-t'))}{\pi(t-t')} \right]^2 \\ &= \sum_{t=b}^{b+B-1} A_1(t-b) \left(\frac{\alpha_1}{B} A_1(t-b) \right) = \frac{\alpha_1}{B} B = \alpha_1. \end{aligned}$$

Substituting the above into Eq. (3.73), we get

$$\text{Var} \left\{ \widehat{S_{\mathbf{X},b,T}^{(1)}}(t_b, f) \right\} \approx \left(\frac{B\sigma_{\mathbf{X}}^2}{\alpha_1 \sum_{t=b}^{b+B-1} A_1(t-b)(t-t_b)} \right)^2 \alpha_1 = \frac{B^2\sigma_{\mathbf{X}}^4}{\alpha_1 \left[\sum_{t=b}^{b+B-1} A_1(t-b)(t-t_b) \right]^2}.$$

Note that since A_1 is approximately linear for $t \in \{0, 1, \dots, B-1\}$, according to the orthogonality property from Eq. (3.24), $\sum_{t=b}^{b+B-1} A_1(t-b)(t-t_b) = O(B)$. Since $\alpha_1 \approx 2BW - 1/2$, $\text{Var} \left\{ \widehat{S_{\mathbf{X},b,T}^{(1)}}(t_b, f) \right\} = O(B^{-1})$. In other words, as the block size B increases, the variance of the time derivative of the time-frequency spectrum estimate will decrease.

3.9 Simulated Processes

In this section, we introduce four examples of nonstationary processes, three of which are UMPs and one which is not. We simulate realizations of each of these four examples and estimate their time-frequency spectra using the HRS, SWHRS, and BCMTFSE and provide a graphical comparison of the three estimators.

3.9.1 Example 1

Following an example from [Priestley 1965], let $\mathbf{X} \triangleq \{X_t\}_{t \in \mathbb{Z}}$ be a discrete-time UMP of the form

$$X_t = e^{\frac{-(t-500)^2}{2(200)^2}} Y_t, \quad \forall t \in \mathbb{Z}, \quad (3.74)$$

where $\mathbf{Y} = \{Y_t\}_{t \in \mathbb{Z}}$ is the second-order autoregressive process

$$Y_t = 0.8Y_{t-1} - 0.4Y_{t-2} + \varepsilon_t, \quad \forall t \in \mathbb{Z}. \quad (3.75)$$

Here $\{\varepsilon_t\}_{t \in \mathbb{Z}}$ is a stationary white noise process with variance 10^4 . The spectrum of \mathbf{Y} [Percival and Walden 1993] is therefore given by

$$S_{\mathbf{Y}}(f) = \frac{10^4}{1 - 2.24 \cos(2\pi f) + 1.6 \cos^2(2\pi f)}, \quad \forall f \in [-1/2, 1/2]. \quad (3.76)$$

The time-frequency spectrum of \mathbf{X} (see Section 3.3) is given by

$$S_{\mathbf{X}}(t, f) = \left(e^{\frac{-(t-500)^2}{2(200)^2}} \right)^2 S_{\mathbf{Y}}(f), \quad \forall t \in \mathbb{Z}, \forall f \in [-1/2, 1/2]. \quad (3.77)$$

We generate 100 realizations of \mathbf{X} of length $N = 1000$. To each realization, we apply the HRS estimator, SWHRS estimator and BCMTFSE to estimate the time-frequency spectrum of \mathbf{X} for a block size of $B = 100$, $K = 7$, and $W = 0.04$. For each method of estimation, the final time-frequency spectrum estimates were taken to be the averages of the estimates over all 100 realizations, over 20 realizations, over 10 realizations, and finally over a single realization.

Figures 3.2 and 3.3 compare the time-frequency spectrum of \mathbf{X} and the estimates produced by the HRS estimator, SWHRS estimator, and BCMTFSE at $t = 300$ and $f = 0.0483$, respectively. Figure 3.4 shows the time-frequency spectrum of \mathbf{X} and its estimation using the BCMTFSE. Figure 3.5 compares the theoretical mean of the MTFSE from Eq. (3.48) with the time-frequency spectrum of \mathbf{X} and the BCMTFSE estimate when it is the average of the estimates over 100 realizations.

3.9.2 Example 2

Let $\mathbf{X} \triangleq \{X_t\}_{t \in \mathbb{Z}}$ be a discrete-time UMP of the form

$$X_t = \sqrt{1 + \frac{t}{T}} Y_t, \quad \forall t \in \mathbb{Z}, \quad (3.78)$$

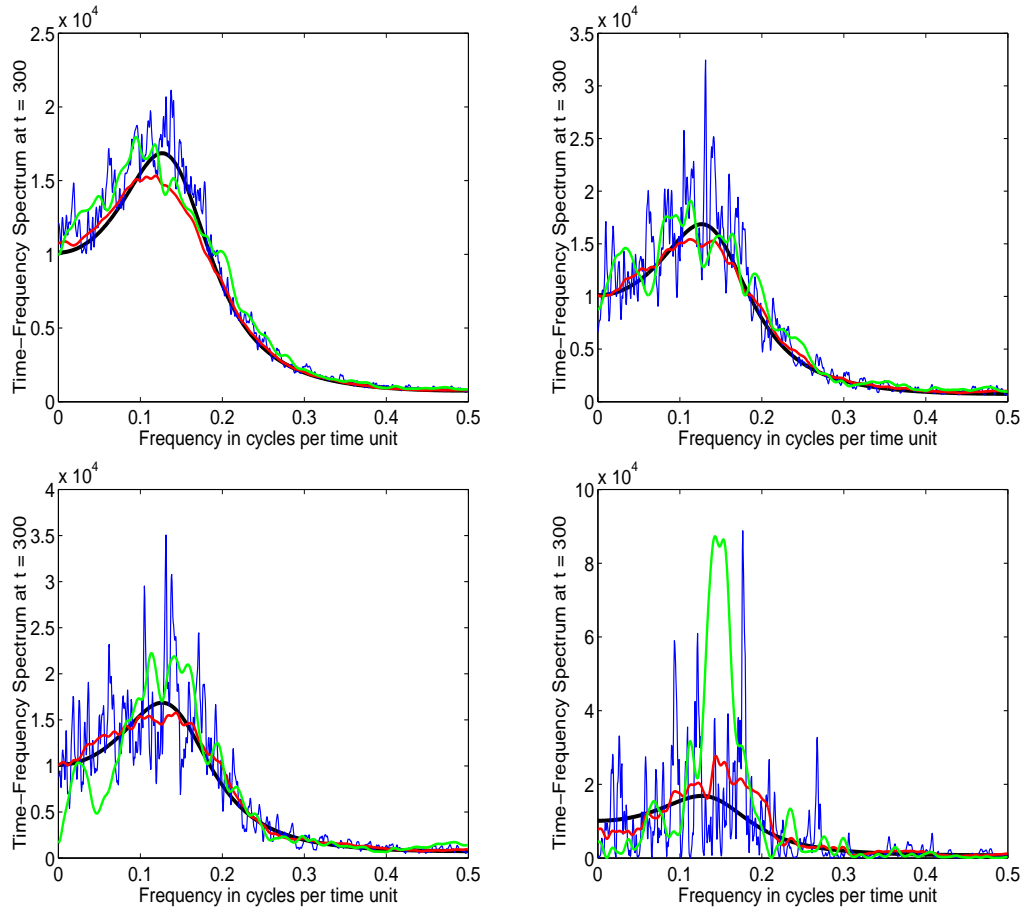


Figure 3.2: **Comparison of the HRS, SWHRS, BCMTFSE, and the time-frequency spectrum for Example 1.** The time-frequency spectrum of \mathbf{X} (black line), HRS estimate (blue line), SWHRS estimate (green line), and BCMTFSE (red line) at $t = 300$ for Example 1. The relevant parameters are $B = 100$, $W = 0.04$, and $K = 7$. The estimates are averaged over 100 (top left), 20 (top right), 10 (bottom left) and 1 (bottom right) realization(s).

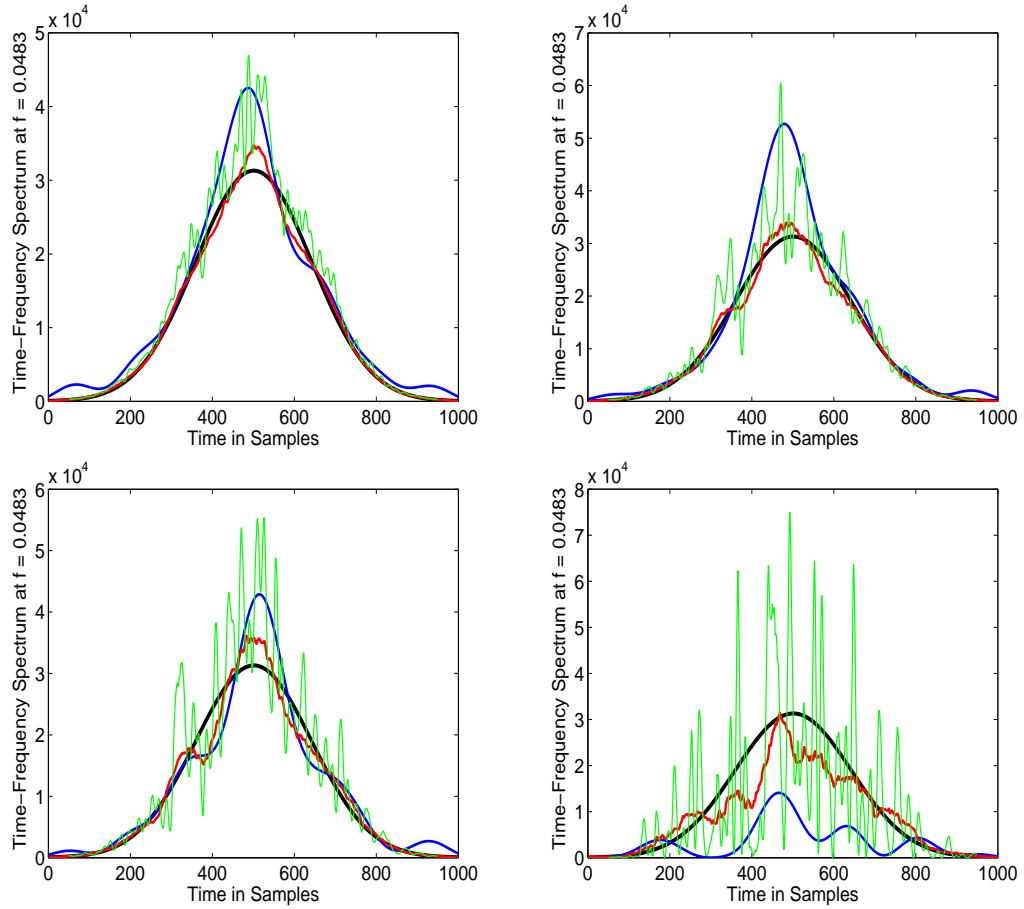


Figure 3.3: **Comparison of the HRS, SWHRS, BCMTFSE, and the time-frequency spectrum at $f = 0.0483$ for Example 1.** The time-frequency spectrum of \mathbf{X} (black line), HRS estimate (blue line), SWHRS estimate (green line), and BCMTFSE (red line) at $f = 0.0483$ for Example 1. The relevant parameters are $B = 100$, $W = 0.04$, and $K = 7$. The estimates are averaged over 100 (top left), 20 (top right), 10 (bottom left) and 1 (bottom right) realization(s), respectively. The SWHRS estimate is not defined in the boundary regions.

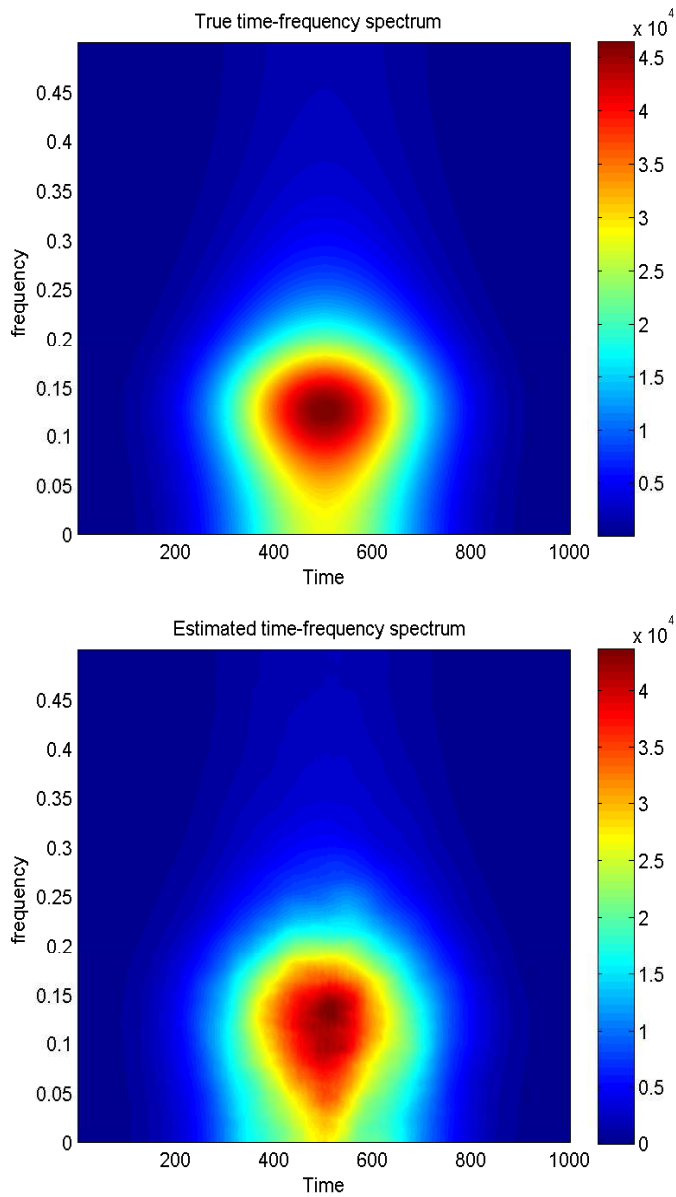


Figure 3.4: **The time-frequency spectrum and the BCMTFSE for Example 1.** The time-frequency spectrum of \mathbf{X} from Eq. (3.77) when $t \in \{0, 1, \dots, N - 1\}$, and $N = 1000$ (top) and estimated time-frequency spectrum using BCMTFSE with a block size of $B = 100$, $W = 0.04$ and $K = 7$ (bottom) for Example 1. The estimate in the bottom figure is the result of averaging over 100 realizations of \mathbf{X} .

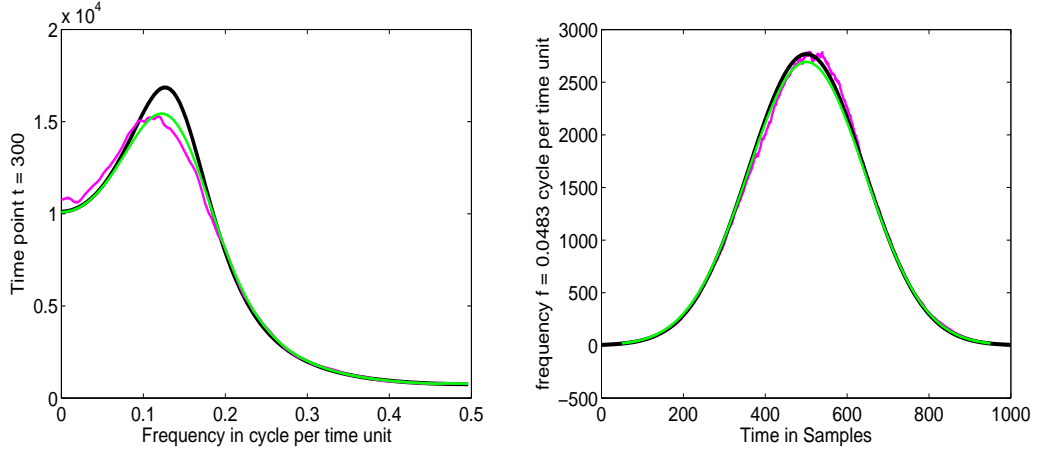


Figure 3.5: **Comparison of the theoretical mean of the MTFSE, the BCMTFSE and the time-frequency spectrum for Example 1.** Theoretical mean of MTFSE from Eq. (3.48) (green line), the time-frequency spectrum (black line), and estimated time-frequency spectrum using the BCMTFSE (magenta line) in Example 1. Here $B = 100$, $W = 0.04$, and $K = 7$. Note that the theoretical mean of the MTFSE is not defined in the boundary regions.

where $T = 200$ and $\mathbf{Y} \triangleq \{Y_t\}_{t \in \mathbb{Z}}$ is the second-order autoregressive process from Eq. (3.75). The time-frequency spectrum of \mathbf{X} (see Section 3.3) is given by

$$S_{\mathbf{X}}(t, f) = \left(1 + \frac{t}{T}\right) S_{\mathbf{Y}}(f), \quad \forall t \in \mathbb{Z}, f \in [-1/2, 1/2], \quad (3.79)$$

where $S_{\mathbf{Y}}$ is as in Eq. (3.76).

We generate 100 realizations of \mathbf{X} of length $N = 1000$. To each realization, we apply the HRS estimator, SWHRS estimator and BCMTFSE to estimate the time-frequency spectrum of \mathbf{X} for a block size of $B = 200$, $K = 7$, and $W = 0.02$. For each method of estimation, the final time-frequency spectrum estimate was taken to be the average of the estimates over all 100 realizations.

Figure 3.6 compares the time-frequency spectrum of \mathbf{X} and all the estimates produced by the HRS estimator, SWHRS estimator, and BCMTFSE at $f = 0.0483$ and $t = 300$. Figure 3.7 shows the time-frequency spectrum and its estimation using the BCMTFSE.

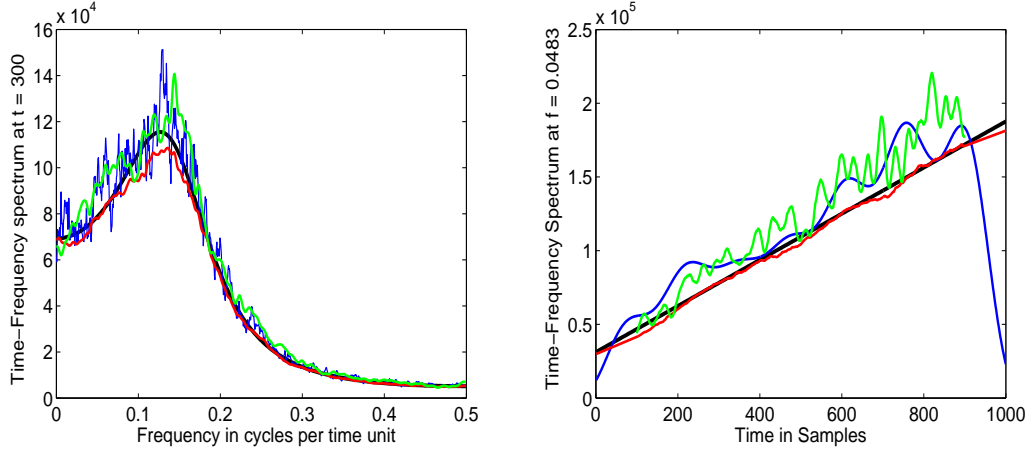


Figure 3.6: **Comparison of the HRS, SWHRS, BCMTFSE, and the time-frequency spectrum at $f = 0.0483$ and $t = 300$ for Example 2.** The time-frequency spectrum of \mathbf{X} (black line), HRS estimate (blue line), SWHRS estimate (green line), BCMTFSE (red line) at $f = 0.0483$ (right), and $t = 300$ (left) for Example 2. The relevant parameters are $B = 200$, $W = 0.02$, and $K = 7$. The estimates are averaged over 100 realizations. Note that in the right-hand plot, the SWHRS estimate is not defined in the boundary regions.

3.9.3 Example 3

Let $\mathbf{X} \triangleq \{X_t\}_{t \in \mathbb{Z}}$ be a discrete-time UMP of the form

$$X_t = \cos(2\pi f_s t) Y_t, \quad t \in \mathbb{Z}, \quad (3.80)$$

where $f_s = 0.001$ is fixed, and $\mathbf{Y} = \{Y_t\}_{t \in \mathbb{Z}}$ is the second-order autoregressive process from Eq. (3.75). The time-frequency spectrum of \mathbf{X} is given by

$$S_{\mathbf{X}}(t, f) = \cos^2(2\pi f_s t) S_{\mathbf{Y}}(f), \quad \forall t \in \mathbb{Z}, f \in [-1/2, 1/2], \quad (3.81)$$

where $S_{\mathbf{Y}}$ is as in Eq. (3.76).

We generate 100 realizations of \mathbf{X} of length $N = 1000$. To each realization, we apply the HRS estimator, SWHRS estimator and BCMTFSE to estimate the time-frequency spectrum of \mathbf{X} for a block size of $B = 100$, $K = 7$, and $W = 0.04$. For each method of estimation, the final time-frequency spectrum estimate was taken to

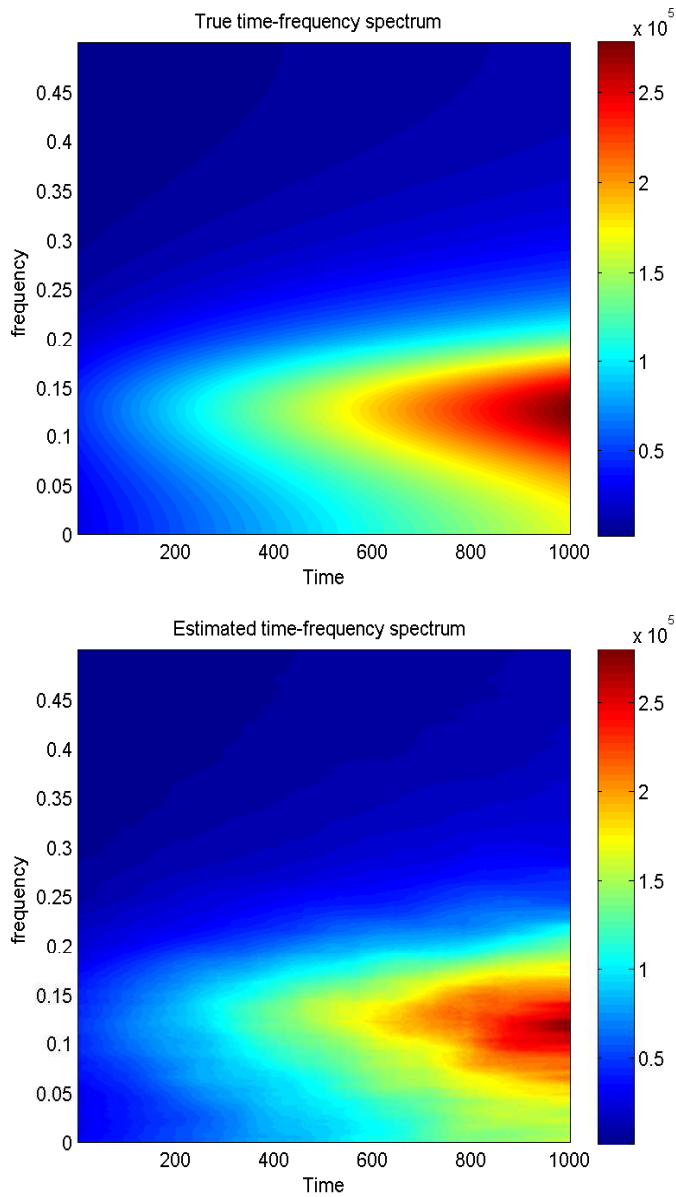


Figure 3.7: **The time-frequency spectrum and the BCMTFSE for Example 2.** The time-frequency spectrum of \mathbf{X} from Eq. (3.79) when $t \in \{0, 1, \dots, N - 1\}$, and $N = 1000$ (top) and estimated time-frequency spectrum using BCMTFSE with a block size of $B = 200$, $W = 0.02$ and $K = 7$ (bottom) for Example 2. The estimate in the bottom figure is the result of averaging over 100 realizations of \mathbf{X} .

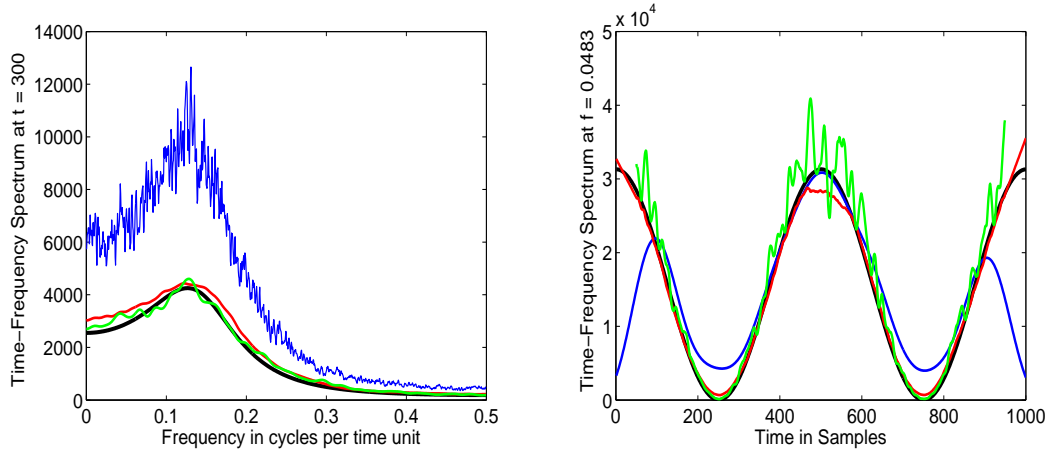


Figure 3.8: **Comparison of the HRS, SWHRS, BCMTFSE, and the time-frequency spectrum at $f = 0.0483$ and $t = 300$ for Example 3.** The time-frequency spectrum of \mathbf{X} (black line), HRS estimate (blue line), SWHRS estimate (green line), BCMTFSE (red line) at $f = 0.0483$ (right), and $t = 300$ (left) for Example 3. The relevant parameters are $B = 100$, $W = 0.04$, and $K = 7$. The estimates are averaged over 100 realizations. In the right plot the SWHRS estimate is not defined in the boundary regions.

be the average of the estimates over all 100 realizations.

Figure 3.8 compares the time-frequency spectrum of \mathbf{X} and all the estimates produced by the HRS estimator, SWHRS estimator, and BCMTFSE at $f = 0.0483$ and $t = 300$. Figure 3.9 shows the time-frequency spectrum and its estimation using the BCMTFSE.

3.9.4 Example 4

Assume that the partial autocorrelation functions (PACFs) of an autoregressive process of order two (or AR(2)) are known. In order to construct a nonstationary time series, we set the first partial autocorrelation, Ψ_1 to be constant, and the second one, Ψ_2 to be a time-dependent function

$$\Psi_1 \triangleq 0.52, \quad \text{and}$$

$$\Psi_2(t) \triangleq 0.3 \cos(2\pi f_s t), \quad \text{where } f_s = 0.002.$$

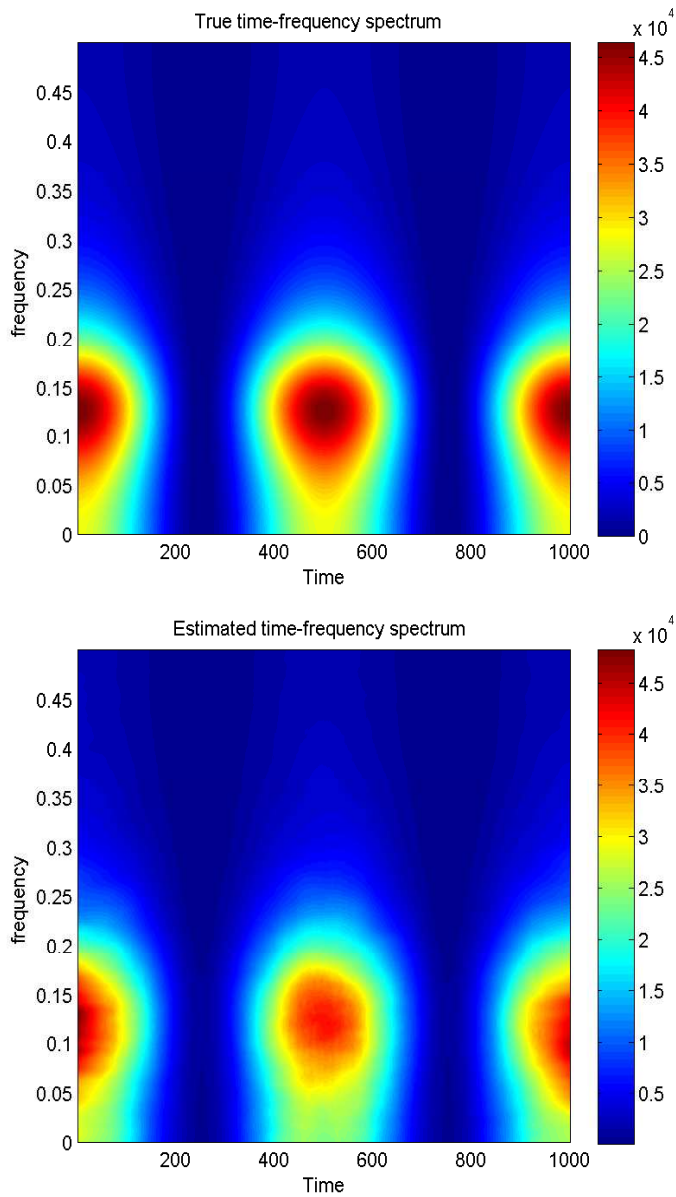


Figure 3.9: **The time-frequency spectrum and the BCMTFSE for Example 3.** The time-frequency spectrum of \mathbf{X} from Eq. (3.81) when $t \in \{0, 1, \dots, N - 1\}$, and $N = 1000$ (top) and estimated time-frequency spectrum using BCMTFSE with a block size of $B = 200$, $W = 0.02$ and $K = 7$ (bottom) for Example 3. The estimate in the bottom figure is the result of averaging over 100 realizations of \mathbf{X} .

It has been shown in [Durbin 1960] and [Ramsey 1974] that there exists a recursive relationship between the PACFs and the coefficients of an autoregressive (AR) process of the form

$$a_j^{(k+1)} = a_j^{(k)} - \Psi_{k+1} a_{k+1-j}^{(k)}, \quad j = 1, \dots, k \quad (3.82)$$

$$a_k^{(k)} = \Psi_k, \quad (3.83)$$

where $a_j^{(k)}$ is the j th AR coefficient and Ψ_k is the k th PACF. In particular, for an AR(2) process, Eqs. (3.82) and (3.83) become

$$\begin{aligned} a_1^{(1)} &= \Psi_1 \\ a_1^{(2)}(t) &= a_1^{(1)} - \Psi_2(t) a_1^{(1)} \\ a_2^{(2)}(t) &= \Psi_2(t). \end{aligned}$$

As we can see, knowledge of Ψ_1 and Ψ_2 is equivalent to knowledge of the time-dependent AR(2) coefficients $a_1^{(2)}$ and $a_2^{(2)}$.

Using the coefficients $a_1^{(2)}$ and $a_2^{(2)}$, we can define a nonstationary AR(2) process $\mathbf{X} \triangleq \{X_t\}_{t \in \mathbb{Z}}$ by defining

$$X_t \triangleq a_1^{(2)}(t) X_{t-1} + a_2^{(2)}(t) X_{t-2} + \varepsilon_t, \quad t \in \mathbb{Z}, \quad (3.84)$$

where $\{\varepsilon_t\}_{t \in \mathbb{Z}}$ is a stationary white noise process with variance $\sigma_\varepsilon^2 = 10^4$.

Assume that $\mathbf{Y} = \{Y_t\}_{t \in \mathbb{Z}}$ is a AR(p) stationary process. Then the spectrum of \mathbf{Y} is [Percival and Walden 1993]

$$S_{\mathbf{Y}}(f) = \frac{\sigma_\varepsilon^2}{\left| 1 - \sum_{u=1}^p a_u^{(p)} e^{-i2\pi f u} \right|^2}, \quad \forall t \in \mathbb{Z}, \forall f \in [-1/2, 1/2], \quad (3.85)$$

where $a_u^{(p)}$ are the AR(p) coefficients and σ_ε^2 is as defined as before. Having the time-

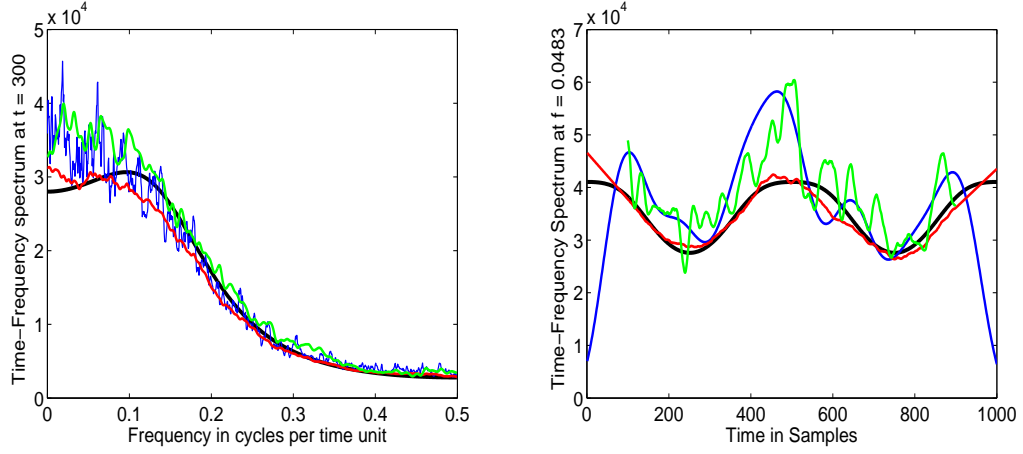


Figure 3.10: **Comparison Between the HRS, SWHRS, BCMTFSE, and the time-frequency spectrum at $f = 0.0483$ and $t = 300$ for Example 4.** The time-frequency spectrum of \mathbf{X} (black line), HRS estimate (blue line), SWHRS estimate (green line), BCMTFSE (red line) at $f = 0.0483$ (right), and $t = 300$ (left) for Example 4. The relevant parameters are $B = 100$, $W = 0.04$, and $K = 7$. The estimates are averaged over 100 realizations. In the right plot the SWHRS estimate is not defined in the boundary regions.

dependent coefficients of the nonstationary autoregressive process \mathbf{X} , one can replace $\alpha_u^{(p)}$ in Eq. (3.86) by $\alpha_u^{(p)}(t)$ in order to calculate the time-frequency spectrum of \mathbf{X}

$$S_{\mathbf{X}}(t, f) = \frac{10^4}{\left|1 - \sum_{u=1}^p a_u^{(p)}(t) e^{-i2\pi f u}\right|^2}, \quad \forall t \in \mathbb{Z}, \forall f \in [-1/2, 1/2]. \quad (3.86)$$

We generate 100 realizations of \mathbf{X} of length $N = 1000$. To each realization, we apply the HRS estimator, SWHRS estimator and BCMTFSE to estimate the time-frequency spectrum of \mathbf{X} for a block size of $B = 100$, $K = 7$, and $W = 0.04$. For each method of estimation, the final time-frequency spectrum estimate was taken to be the average of the estimates over all 100 realizations.

Figure 3.10 compares the time-frequency spectrum of \mathbf{X} and all the estimates produced by the HRS estimator, SWHRS estimator, and BCMTFSE at $f = 0.0483$ and $t = 300$. Figure 3.11 shows the time-frequency spectrum and its estimation using the BCMTFSE.

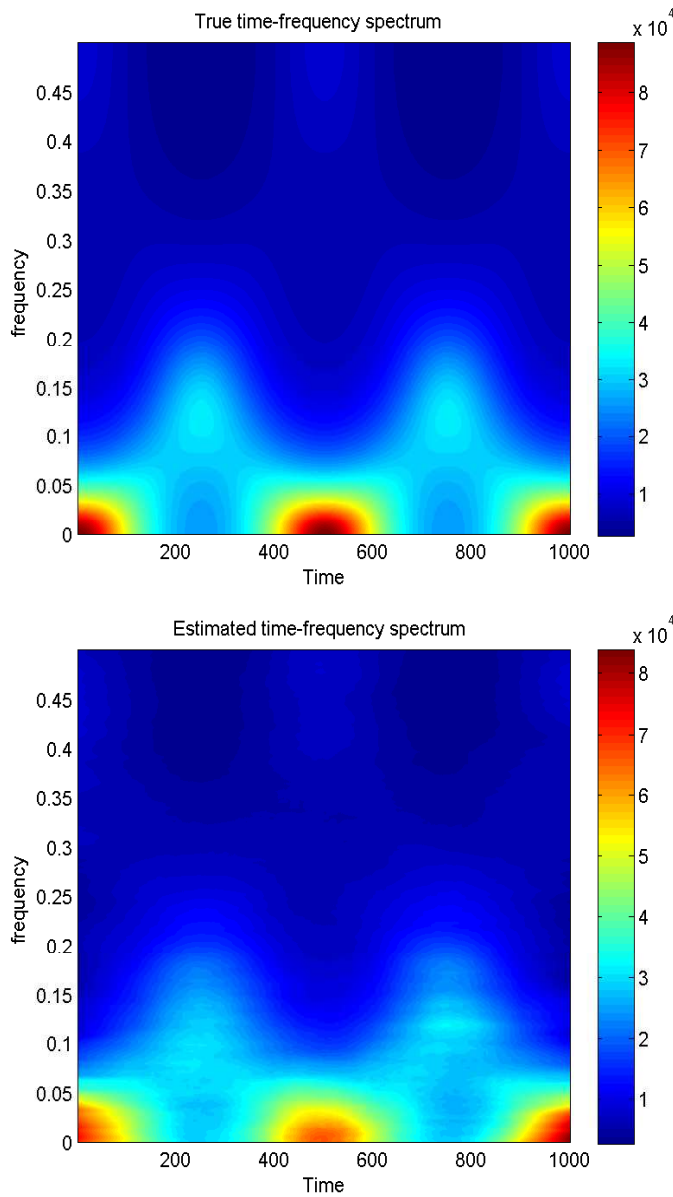


Figure 3.11: **The time-frequency spectrum and the BCMTFSE for Example 4.** The time-frequency spectrum of \mathbf{X} from Eq. (3.86) when $t \in \{0, 1, \dots, N - 1\}$, and $N = 1000$ (top) and estimated time-frequency spectrum using BCMTFSE with a block size of $B = 100$, $W = 0.04$ and $K = 7$ (bottom) for Example 4. The estimate in the bottom figure is the result of averaging over 100 realizations of \mathbf{X} .

3.9.5 Comments on the Examples

Figures 3.2, 3.3 for Example 1, Figure 3.6 for Example 2, Figure 3.8 for Example 3, and Figure 3.10 for Example 4 all display comparisons between the time-frequency spectrum, the HRS estimator, the SWHRS estimator and finally the BCMTFSE at $t = 300$ and $f = 0.0483$. It is clear from looking at each of these figures that the BCMTFSE is superior in estimating the time-frequency spectrum near and in the time boundaries of the time-frequency plane. The improvement is more obvious in the plots appearing on the right-hand sides of Figures 3.6, 3.8, and 3.10. The improvement is not very evident in Example 1, since the time-frequency spectrum itself tends to zero at the boundaries of the time-frequency plane. Also, examining each of the figures mentioned above, one can clearly see that the BCMTFSE is “smoother” than the the HRS and SWHRS. It is possible to see that for a fixed time point, the time-frequency spectra of each of the four given examples have relatively slow variation in the frequency direction. As a result, blocking the data with a small block size (small compared to the sample size) improves the time resolution of the time-frequency spectrum estimate while maintaining a reasonable frequency resolution. Note that if, at some fixed time and frequency, the time-frequency spectrum changes rapidly in the time and frequency directions, then one might not hope to estimate the time-frequency spectrum with good time and frequency resolutions.

3.10 Conclusion

In this chapter, we proposed an estimator of the time-frequency spectrum of a nonstationary process. The estimator was derived using an estimate of the time-derivative of the process’s time-frequency spectrum. The key advantage of our estimator is that it has improved boundary behaviour in the time-frequency plane versus two existing windowed estimates such as the HRS and SWHRS. Moreover, due to blocking

our estimator has better time resolution compared with the HRS estimator and it is smoother comparing with HRS and SWHRS. The performance of our estimator was demonstrated by applying it to several simulated nonstationary processes.

Chapter 4

Diagnostic Plots for Detection of Uniformly Modulated Processes and an Improved BCMTFSE

4.1 Introduction

Uniformly modulated processes (UMPs) (see Section 3.2.1) form a class of nonstationary processes whose time-frequency spectra take a particularly simple form. This simplicity makes UMPs convenient choices of nonstationary processes for analysis and simulation. Besides the mathematical simplicity of UMPs, they have been successfully used in practice as models for real-world data. For example, UMPs are suitable models for seismological data [Herbst 1963a,b,c]. Specific examples of the models suggested by Herbst were applied to earthquake data by Fujita and Shibara [1978], and Dargahi-Noubary [1978a,b] has used UMPs to model earthquake and explosion data. Dargahi-Noubary and Laycock [1981] also discuss the problem of analyzing seismological data modeled by UMPs with a view to discriminating between earthquakes and nuclear explosions.

In Section 3.7, we introduced the BCMTFSE to estimate the time-frequency spectrum of a nonstationary process. The BCMTFSE is based on a division of a given realization into overlapping segments (blocks). As a result, the BCMTFSE has improved time resolution at the cost of diminished frequency resolution. In this chapter, we show that if the process under study is a UMP, we can improve the frequency resolution of the BCMTFSE, and hence obtain an estimator of the time-frequency spectrum with “good” time and frequency resolutions. Since the estimator we propose is based on the assumption that the process under study is a UMP, we first describe a heuristic graphical technique which one can use to draw reasonably accurate conclusions about whether a given process is indeed a UMP.

This chapter is structured as follows. In Section 4.2 we introduce a graphical technique which uses the BCMTFSE to draw conclusions about whether or not a process is a UMP. In Section 4.3 we describe a case in which the modulating function of a UMP can be estimated; this estimate is used in Section 4.4 to improve the frequency resolution of the BCMTFSE. In Section 4.5 we demonstrate the performance of the graphical technique introduced in Section 4.2, and the time-frequency spectrum estimator introduced in Section 4.4, on simulated nonstationary processes.

4.2 Diagnostic Plots for Detection of UMPs

Let $\mathbf{X} \triangleq \{X_t\}_{t \in \mathbb{Z}}$ be a discrete-time real-valued zero-mean nonstationary process with time-frequency spectrum $S_{\mathbf{X}}$. Since \mathbf{X} is real-valued, $S_{\mathbf{X}}$ is symmetric in f around $f = 0$, so we restrict our attention to frequencies $f \in [0, 1/2]$. Evaluating $S_{\mathbf{X}}$ at N time points $t \in \{0, 1, \dots, N-1\}$ and M frequencies $f_k = \frac{k-1}{2M}$, where $k \in \{1, \dots, M\}$ and $M \geq 2N$ yields a discretized version of $S_{\mathbf{X}}$ which is an $N \times M$ matrix, denoted by $\mathbb{S}_{\mathbf{X}}$. We call the matrix $\mathbb{S}_{\mathbf{X}}$ the *time-frequency spectrum matrix* of \mathbf{X} (with respect to N and M) or the *TFS matrix* of \mathbf{X} for short.

It can easily be seen that the TFS matrix of \mathbf{X} has rank one if \mathbf{X} is a UMP. Briefly, if \mathbf{X} is a UMP then $X_t = C_t Y_t$ for all $t \in \mathbb{Z}$, where $\mathbf{Y} \triangleq \{Y_t\}_{t \in \mathbb{Z}}$ is a stationary process and each $C_t \in \mathbb{R}$ is nonnegative. The time-frequency spectrum of \mathbf{X} is therefore given by $S_{\mathbf{X}}(t, f) = C_t^2 S_{\mathbf{Y}}(f)$, where $S_{\mathbf{Y}}$ is the spectrum of \mathbf{Y} (see Section 3.2.1 for details). We further assume that \mathbf{Y} is non-deterministic [Grenander and Szegö 1955] so that $S_{\mathbf{Y}} > 0$ and also that each $C_t \neq 0$. The TFS matrix of \mathbf{X} is therefore given by

$$\mathbb{S}_{\mathbf{X}} = \begin{bmatrix} C_0^2 S_{\mathbf{Y}}(f_1) & C_0^2 S_{\mathbf{Y}}(f_2) & \dots & C_0^2 S_{\mathbf{Y}}(f_M) \\ C_1^2 S_{\mathbf{Y}}(f_1) & C_1^2 S_{\mathbf{Y}}(f_2) & \dots & C_1^2 S_{\mathbf{Y}}(f_M) \\ \vdots & \vdots & \ddots & \vdots \\ C_{N-1}^2 S_{\mathbf{Y}}(f_1) & C_{N-1}^2 S_{\mathbf{Y}}(f_2) & \dots & C_{N-1}^2 S_{\mathbf{Y}}(f_M) \end{bmatrix}.$$

The reason that the above matrix has rank one is because $\mathbb{S}_{\mathbf{X}}$ can be written as the product of a column vector $[C_0^2 \ C_1^2 \ \dots \ C_{N-1}^2]^T$ where superscript T indicates transposition and a row vector $[S_{\mathbf{Y}}(f_1) \ S_{\mathbf{Y}}(f_2) \ \dots \ S_{\mathbf{Y}}(f_M)]$. Note that a stationary process is a UMP with $C_t = 1$ for all $t \in \mathbb{Z}$, and therefore $S_{\mathbf{X}}(t, f) = S_{\mathbf{Y}}(f)$ when \mathbf{X} is stationary. It is then obvious that the TFS matrix of \mathbf{X} is a rank one matrix when \mathbf{X} is stationary. The TFS matrix of \mathbf{X} having higher rank (*i.e.*, rank > 1) indicates that \mathbf{X} is not a UMP.

Similarly, discretization of $\log S_{\mathbf{X}}$ at the same M frequencies and N time points gives another $N \times M$ matrix, which we refer to as the *log time-frequency spectrum matrix* of \mathbf{X} , or the *LTFS matrix* of \mathbf{X} , denoted by $\log \mathbb{S}_{\mathbf{X}}$. It can be seen that the LTFS matrix is a rank one matrix if \mathbf{X} is a stationary process and is a rank two matrix if \mathbf{X} is a UMP with $C_t \neq 1$ for all $t \in \mathbb{Z}$. Indeed, the LTFS matrix, $\log \mathbb{S}_{\mathbf{X}}$, is

explicitly given by

$$\begin{aligned} \log \mathbb{S}_{\mathbf{X}} &= \begin{bmatrix} 2 \log C_0 + \log S_{\mathbf{Y}}(f_1) & \dots & 2 \log C_0 + \log S_{\mathbf{Y}}(f_M) \\ 2 \log C_1 + \log S_{\mathbf{Y}}(f_1) & \dots & 2 \log C_1 + \log S_{\mathbf{Y}}(f_M) \\ \vdots & \ddots & \vdots \\ 2 \log C_{N-1} + \log S_{\mathbf{Y}}(f_1) & \dots & 2 \log C_{N-1} + \log S_{\mathbf{Y}}(f_M) \end{bmatrix} \\ &= \begin{bmatrix} 2 \log C_0 & \dots & 2 \log C_0 \\ 2 \log C_1 & \dots & 2 \log C_1 \\ \vdots & \ddots & \vdots \\ 2 \log C_{N-1} & \dots & 2 \log C_{N-1} \end{bmatrix} + \begin{bmatrix} \log S_{\mathbf{Y}}(f_1) & \dots & \log S_{\mathbf{Y}}(f_M) \\ \log S_{\mathbf{Y}}(f_1) & \dots & \log S_{\mathbf{Y}}(f_M) \\ \vdots & \ddots & \vdots \\ \log S_{\mathbf{Y}}(f_1) & \dots & \log S_{\mathbf{Y}}(f_M) \end{bmatrix}. \end{aligned}$$

In the above equation, the left-hand matrix has rank one since it can be written as a product of a column vector $[\log C_0 \log C_1 \dots \log C_{N-1}]^T$ and a row vector $[2 \ 2 \ \dots \ 2]$. Similarly, assuming $S_{\mathbf{Y}}(f) \neq 1$ for all $f \in \{f_1, f_2, \dots, f_M\}$, the left-hand matrix has rank one since it can be written as the product of a column vector $[1 \ 1 \ \dots \ 1]^T$ and a row vector $[\log S_{\mathbf{Y}}(f_1) \log S_{\mathbf{Y}}(f_2) \dots \log S_{\mathbf{Y}}(f_M)]$. The rank of the sum of two rank one matrices is less than or equal to 2 and therefore the rank of $\log \mathbb{S}_{\mathbf{X}}$ is at most 2 when \mathbf{X} is a UMP. If \mathbf{X} is stationary, $C_t = 1$ for all $t \in \mathbb{Z}$ and so the left-hand matrix is identically zero. As a result, the rank of the LTFS matrix is one. Higher ranks (*i.e.*, rank > 2) of the LTFS matrix indicate that the underlying process \mathbf{X} is not a UMP.

Since we are limited to an estimate of $S_{\mathbf{X}}$, we must find a way to estimate the rank of the estimated TFS matrix, which we denote by $\widehat{\mathbb{S}}_{\mathbf{X}}$. Let X_0, X_1, \dots, X_{N-1} be a realization of \mathbf{X} . Using this realization, we estimate the time-frequency spectrum of \mathbf{X} using the BCMTFSE described in Chapter 3.

There are several existing methods in the literature to test the rank of a random matrix. Let \mathbb{B} be an arbitrary $T \times T$ real-valued random matrix whose rank is of interest. Three different tests proposed by Cragg and Donald [1997], Robin and

Smith [2000], and Ratsimalahelo [2002] assume that there exists a root- T estimator $\widehat{\mathbb{B}}$ of \mathbb{B} so that $\sqrt{T}\text{vec}(\widehat{\mathbb{B}} - \mathbb{B}) \xrightarrow{\text{dist}} \mathcal{N}(0, \Sigma)$, where the symbol “ $\xrightarrow{\text{dist}}$ ” means “converges in distribution” and $\mathcal{N}(0, \Sigma)$ denotes a multivariate normal distribution with mean 0 and covariance matrix Σ . Each of three cited papers makes the assumption that a consistent estimator of Σ is available. Lawley [1956], on the other hand, suggested a test for the rank of a random matrix which was not based on the existence of an estimate of Σ . The test is based instead on the assumption that there exist two Gaussian random vectors r_1 and r_2 such that $\mathbb{B} = \mathbf{E}\{r_1 r_2^\dagger\}$, where superscript \dagger denotes conjugate transpose. Lawley’s test also assumes that \mathbb{B} is full rank, in other words, that the rows and columns of \mathbb{B} are linearly independent sets.

We are interested here in testing the ranks of the estimated TFS matrix $\widehat{\mathbb{S}}_{\mathbf{X}}$, and the estimated LTFS matrix, $\log \widehat{\mathbb{S}}_{\mathbf{X}}$. The methods proposed in [Cragg and Donald 1997], [Robin and Smith 2000], and [Ratsimalahelo 2002] to test the rank of a random matrix are not appropriate for testing the rank of the estimated TFS and LTFS matrices. The reason is that, even assuming that $\sqrt{N}\text{vec}(\widehat{\mathbb{S}}_{\mathbf{X}} - \mathbb{S}_{\mathbf{X}}) \xrightarrow{\text{dist}} \mathcal{N}(0, \Sigma_1)$ and $\sqrt{N}\text{vec}(\log \widehat{\mathbb{S}}_{\mathbf{X}} - \log \mathbb{S}_{\mathbf{X}}) \xrightarrow{\text{dist}} \mathcal{N}(0, \Sigma_2)$, we do not have an obvious method to estimate the covariance matrices Σ_1 and Σ_2 . The method proposed by [Lawley 1956] is also not an appropriate test for determining the rank of the estimated TFS and LTFS matrices. Even assuming that $\log \widehat{\mathbb{S}}_{\mathbf{X}}$ is approximately Gaussian, and $\log \widehat{\mathbb{S}}_{\mathbf{X}} \log \widehat{\mathbb{S}}_{\mathbf{X}}^T$ is a good approximation to $\mathbf{E}\{\log \widehat{\mathbb{S}}_{\mathbf{X}} \log \widehat{\mathbb{S}}_{\mathbf{X}}^T\}$, these are not sufficient assumptions to consider the test suggested by Lawley [1956]. The difficulty is that, due to properties of the DPSS, and the use of overlapping blocks when estimating the time-frequency spectrum using the BCMTFSE, the matrix $\log \widehat{\mathbb{S}}_{\mathbf{X}} \log \widehat{\mathbb{S}}_{\mathbf{X}}^T$ cannot be full rank. The test proposed by [Lawley 1956] is very sensitive to its assumptions; since the assumptions are not completely satisfied in this application, the test cannot be used.

Constructing a test which is not based on any of the methods mentioned above would involve knowledge of the distribution of the time-frequency spectrum estimated

using the BCMTFSE. Since we do not have computable expressions for the expected value and variance of the BCMTFSE (see Section 3.8), we therefore cannot say anything about its distribution. Instead, we propose a graphical method to approximately determine the rank of $\widehat{\mathbb{S}}_{\mathbf{X}}$ and $\log \widehat{\mathbb{S}}_{\mathbf{X}}$. This test can be looked at only as a heuristic tool to make decisions about the rank of $\widehat{\mathbb{S}}_{\mathbf{X}}$ and $\log \widehat{\mathbb{S}}_{\mathbf{X}}$ and does not constitute a true statistical test. The method is based on a singular value decomposition of $\widehat{\mathbb{S}}_{\mathbf{X}}$ and $\log \widehat{\mathbb{S}}_{\mathbf{X}}$, and an examination of their singular values in order to make decisions regarding their ranks. Before describing the method, we briefly review the singular value decomposition.

Let A be a real $N \times M$ matrix. The *singular value decomposition* (SVD) of A is a factorization of A such that $A = U_a D_a V_a^T$, where $U_a \in \mathbb{R}^{N \times N}$ and $V_a \in \mathbb{R}^{M \times M}$ are two orthogonal matrices and $D_a \in \mathbb{R}^{N \times M}$. The matrix D_a is diagonal; its first $p = \min(M, N)$ diagonal entries are the singular values of A and its remaining entries are zero. The number of non-zero singular values of A is equal to its rank (for details regarding the SVD, see [Golub and Van Loan 1983]).

Since $\widehat{\mathbb{S}}_{\mathbf{X}}$ is perturbed by noise, *i.e.*, $\mathbb{S}_{\mathbf{X}} \neq \widehat{\mathbb{S}}_{\mathbf{X}}$, we cannot expect that the singular values of $\widehat{\mathbb{S}}_{\mathbf{X}}$ are equal to those of $\mathbb{S}_{\mathbf{X}}$, or even that $\widehat{\mathbb{S}}_{\mathbf{X}}$ has the same number of non-zero singular values as $\mathbb{S}_{\mathbf{X}}$. As a result, in order to say anything about the rank of estimated TFS matrices and LTFS matrices in order to infer information about the underlying process \mathbf{X} , we take a completely heuristic approach, as follows.

1. Compute the SVD of $\widehat{\mathbb{S}}_{\mathbf{X}}$ and sort the singular values of $\widehat{\mathbb{S}}_{\mathbf{X}}$ in decreasing order. Plot the sorted singular values and visually identify the number of singular values that are clearly separated from the rest. If the number of clearly separated singular values is more than one, we conclude that \mathbf{X} is not a UMP. If the number of clearly separated singular values is one, we conclude that \mathbf{X} is either stationary or a UMP, and proceed to step 2.
2. Compute the SVD of $\log \widehat{\mathbb{S}}_{\mathbf{X}}$ and sort the singular values of $\log \widehat{\mathbb{S}}_{\mathbf{X}}$ in decreasing

order. Plot the sorted singular values starting from the second-largest, and visually identify the number of singular values that are clearly separated from the rest. If the second-largest singular value is clearly separated from the rest, we conclude that \mathbf{X} is a UMP; otherwise, we conclude that \mathbf{X} is stationary. Note that the magnitudes of the singular values of $\log \widehat{\mathbb{S}}_{\mathbf{X}}$ are not “large” in general; since they are sorted in decreasing order, the second-largest singular value might appear close to the rest and not clearly separated. To support the conclusion made in this step between \mathbf{X} being a UMP or stationary, we proceed to step 3.

3. Use the computed SVD of $\widehat{\mathbb{S}}_{\mathbf{X}}$ from step 1. We have $\widehat{\mathbb{S}}_{\mathbf{X}} = UDV^T$ as described earlier. Plot the first column U_1 of U . For a UMP, the column U_1 is an estimate of $[gC_0^2 \ gC_1^2 \ \cdots \ gC_{N-1}^2]^T$ where $g \in \mathbb{R}$ (see Section 4.3). If \mathbf{X} is stationary, $C_t = 1$ for all $t \in \{0, 1, \dots, N-1\}$ and therefore U_1 estimates a constant vector (*i.e.*, a vector all of whose entries are equal). As a result, if U_1 appears to be approximately constant, we conclude that \mathbf{X} is stationary; otherwise, we conclude that \mathbf{X} is a UMP. We refer to U_1 as the *first left eigenvector* of $\widehat{\mathbb{S}}_{\mathbf{X}}$ in the rest of this chapter. We refer to the second column of U as the *second left eigenvector* of $\widehat{\mathbb{S}}_{\mathbf{X}}$.

4.3 Estimation of $\{C_t\}$ and S_Y using the Estimated TFS Matrix of a UMP

Assume that $\mathbf{X} \triangleq \{X_t\}_{t \in \mathbb{Z}}$ is a UMP, so that its time-frequency spectrum has the form $S_{\mathbf{X}}(t, f) = C_t^2 S_Y(f) = G_t S_Y(f)$. As described in Section 4.2, a discretization of $S_{\mathbf{X}}$ at M frequencies $f \in \{f_1, f_2, \dots, f_M\}$ and N time points $t \in \{0, 1, 2, \dots, N-1\}$, denoted by $\mathbb{S}_{\mathbf{X}}$, is called the TFS matrix of \mathbf{X} . In vector notation, $\mathbb{S}_{\mathbf{X}} = \vec{G}\vec{S}$, where $\vec{G} = [G_0 \ G_1 \ \cdots \ G_{N-1}]^T$ is a column vector of length N and

$\vec{S} = [S_Y(f_1) S_Y(f_2) \cdots S_Y(f_M)]$ is a row vector of size M . For notational convenience, we also assume $\vec{C} = [C_0 C_1 \cdots C_{N-1}]^T$ is a column vector of length N .

Let X_0, X_1, \dots, X_{N-1} be a realization of \mathbf{X} . The time-frequency spectrum of \mathbf{X} can be estimated using the BCMTFSE described in Chapter 3. The estimated TFS matrix of \mathbf{X} is an $N \times M$ matrix denoted by $\widehat{\mathbb{S}}_{\mathbf{X}}$. Assuming that the graphical method described in Section 4.2 concludes that \mathbf{X} is a UMP, the goal here is to estimate \vec{G} , \vec{C} and \vec{S} from $\widehat{\mathbb{S}}_{\mathbf{X}}$.

To do so, apply the SVD to $\widehat{\mathbb{S}}_{\mathbf{X}}$ to obtain

$$\widehat{\mathbb{S}}_{\mathbf{X}} = UDV^T,$$

where $U \in \mathbb{R}^{N \times N}$, $D \in \mathbb{R}^{N \times M}$, and $V \in \mathbb{R}^{M \times M}$. Since $N < M$ the first N diagonal entries of D are the singular values of $\widehat{\mathbb{S}}_{\mathbf{X}}$, and its remaining entries are zero. Recall from Section 4.2 that if \mathbf{X} is a UMP, $\widehat{\mathbb{S}}_{\mathbf{X}}$ should have only one “non-zero” or clearly separated singular value. As a result, the first singular value of $\widehat{\mathbb{S}}_{\mathbf{X}}$ should be sufficient to approximately reconstruct $\widehat{\mathbb{S}}_{\mathbf{X}}$, via the approximation

$$\widehat{\mathbb{S}}_{\mathbf{X}} \approx U_1 l_1 V_1^T, \tag{4.1}$$

where U_1 is the first column of U , l_1 is the first singular value of $\widehat{\mathbb{S}}_{\mathbf{X}}$, and V_1^T is the first row of V^T .

Let $B_u, B_v \in \mathbb{R} \setminus \{0\}$ be such that $l_1 = B_u B_v$. Then

$$\widehat{\mathbb{S}}_{\mathbf{X}} \approx U_1 l_1 V_1^T = (B_u U_1)(B_v V_1)^T,$$

so we can regard $B_u U_1$ as an estimate of \vec{G} and $(B_v V_1)^T$ as an estimate of \vec{S} . It is obvious that there are in fact an infinite number of constants B_u and B_v whose product is l_1 ; as a result, one cannot hope to estimate \vec{G} and \vec{S} using the BCMTFSE.

Given $\widehat{\mathbb{S}}_{\mathbf{X}}$, the most one can hope for is to estimate \vec{G} and \vec{S} up to a normalizing constant. To see this, recall that $S_{\mathbf{X}}(t, f) = G_t S_{\mathbf{Y}}(f)$, so the method itself actually specifies G_t only up to a normalizing constant, therefore we assume that $G_{t_1} = 1$ for some given t_1 where $0 \leq t_1 \leq N - 1$. As a result, $S_{\mathbf{X}}(t_1, f) = S_{\mathbf{Y}}(f)$ for all f and \mathbf{X} is referred to as a *normal UMP*.

In order to estimate \vec{G} and \vec{S} under the assumption that \mathbf{X} is a normal UMP, we apply the SVD to $\widehat{\mathbb{S}}_{\mathbf{X}}$ as in Eq. (4.1). Since $G_{t_1} = 1$ and we want $B_u U_1$ to estimate \vec{G} , we select B_u such that the t_1 th entry of U_1 multiplied by B_u is equal to 1. Then from the fact that $l_1 = B_u B_v$, it follows that $B_v = \frac{l_1}{B_u}$. As a result, $\widehat{\vec{G}} \triangleq B_u U_1$ is an estimate of \vec{G} and $\widehat{\vec{S}} \triangleq B_v V_1^T$ is an estimate of \vec{S} . Since \vec{C} is a real-valued vector $\widehat{\vec{C}} \triangleq \sqrt{\widehat{\vec{G}}}$ is an estimate of \vec{C} .

4.4 Improving the Frequency Resolution of the BCMTFSE for UMPs

Let $\mathbf{X} \triangleq \{X_t\}_{t \in \mathbb{Z}}$ be a discrete-time UMP. Let X_0, X_1, \dots, X_{N-1} be a realization of \mathbf{X} . Let $\vec{X} = [X_0 \ X_1 \ \dots \ X_{N-1}]^T$ be a column vector of length N . We apply the BCMTFSE (see Chapter 3) to \vec{X} in order to estimate $\mathbb{S}_{\mathbf{X}}$. Conceptually, the BCMTFSE is a “sliding window” estimator; as a result, the frequency resolution of the BCMTFSE is traded off in order to achieve better time resolution. In Section 4.2, we described a heuristic graphical procedure to determine which class of processes \mathbf{X} belongs to. In this section, we describe an application in which knowing which class of processes \mathbf{X} belongs to can be used to improve the frequency resolution of the BCMTFSE.

Following the steps described in Section 4.2 to draw conclusions about \mathbf{X} , if one concludes that \mathbf{X} is a UMP, then the frequency resolution of the BCMTFSE can be improved as follows. Recall from Section 4.3 that \vec{G} and \vec{C} can be estimated

up to a normalizing constant. Assuming that $\widehat{\vec{C}}$ has non-zero entries, \vec{X} can be divided by $\widehat{\vec{C}}$ to obtain a new realization Y_0, Y_1, \dots, Y_{N-1} , which can be looked at as a realization of a stationary process \mathbf{Y} . We apply multitaper spectrum estimation (see Appendix B) to Y_0, Y_1, \dots, Y_{N-1} in order to estimate the spectrum of \mathbf{Y} at M frequencies $f \in \{f_1, f_2, \dots, f_M\}$. We denote $\vec{S}_M = [\widehat{S}_{\mathbf{Y}}(f_1) \widehat{S}_{\mathbf{Y}}(f_2) \cdots \widehat{S}_{\mathbf{Y}}(f_M)]$ which is a row vector of length M . The $N \times M$ matrix $\mathbb{S}_{\mathbf{X}}^I \triangleq \widehat{\vec{G}} \vec{S}_M$ is called the *improved time-frequency spectrum estimator* (ITFSE) for \mathbf{X} . In Section 4.5, we provide an example to show the improvement of the frequency resolution of the BCMTFSE using the ITFSE modification.

4.5 Examples

In this section we consider five example nonstationary processes, four of which were previously introduced in Chapter 3. For each of the first four examples, we apply the graphical method explained in Section 4.2. For the fifth and final example, we apply the BCMTFSE and ITFSE methods and compare the two.

4.5.1 Example 1

Recall the nonstationary UMP \mathbf{X} introduced in Section 3.9.1, Eq. (3.74). We generate 100 realizations of \mathbf{X} of length $N = 1000$. For each realization, we estimate the time-frequency spectrum of \mathbf{X} using the BCMTFSE (see Chapter 3) at N time points $t \in \{0, 1, \dots, N-1\}$ and M frequencies $f \in \{f_1, f_2, \dots, f_M\}$ to create the estimated TFS matrix $\widehat{\mathbb{S}}_{\mathbf{X}}$ (see Section 4.2). For the sake of comparison, the final estimates of the TFS matrix of \mathbf{X} are the averages of the estimated TFS matrices over all 100 realizations, over 20 realizations, over 10 realizations, and finally over a single realization. We compute the SVD of $\widehat{\mathbb{S}}_{\mathbf{X}}$ and $\log \widehat{\mathbb{S}}_{\mathbf{X}}$ and follow the steps described in section 4.2 in order to draw conclusions about the class of processes \mathbf{X} belongs to.

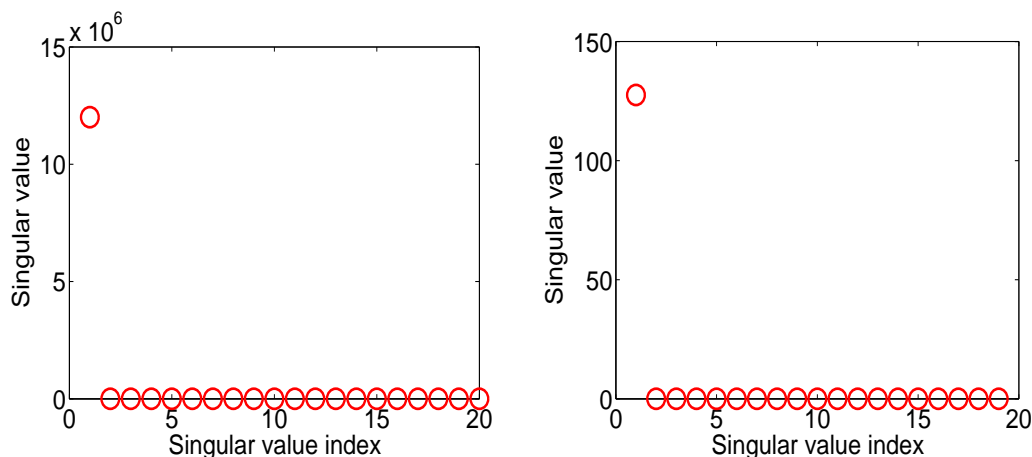


Figure 4.1: **Singular values of the theoretical TFS matrix for Example 1.** The first 20 singular values of the theoretical TFS matrix (left plot) and the first 20 singular values of the theoretical LTFS matrix (right plot), starting from the second-largest.

Figure 4.1 displays the first 20 singular values of $\mathbb{S}_{\mathbf{X}}$ and $\log \mathbb{S}_{\mathbf{X}}$. These two matrices were computed by evaluating the theoretical time-frequency spectrum of \mathbf{X} from Eq. (3.77) and its base-10 logarithm at $t \in \{0, 1, \dots, 1000\}$ and $f \in \{f_1, f_2, \dots, f_M\}$ where $M = 2000$ and $f_k = \frac{k-1}{2M}$. Figure 4.2 displays the first 20 sorted singular values of $\widehat{\mathbb{S}}_{\mathbf{X}}$. Figure 4.3 displays the first 20 sorted singular values of $\log \widehat{\mathbb{S}}_{\mathbf{X}}$ starting from the second-largest. Figure 4.4 displays the first left eigenvector of $\widehat{\mathbb{S}}_{\mathbf{X}}$ as described in step 3 in Section 4.2.

Following the steps described in Section 4.2, we can say the following. The number of clearly separated singular values in the bottom-right plot (in blue) of Figure 4.2 is 1, and therefore we conclude that \mathbf{X} is either a UMP or stationary. Examining the singular values of the estimated LTFS matrix, starting from the second-largest (shown in blue in the bottom-right plot of Figure 4.3), it is clear that one of the singular values is separated from the rest. Therefore, we conclude that \mathbf{X} is a UMP. The bottom-right plot (in blue) of Figure 4.4 also gives additional support to this conclusion, since the first left eigenvector of $\widehat{\mathbb{S}}_{\mathbf{X}}$ is obviously not a constant vector.

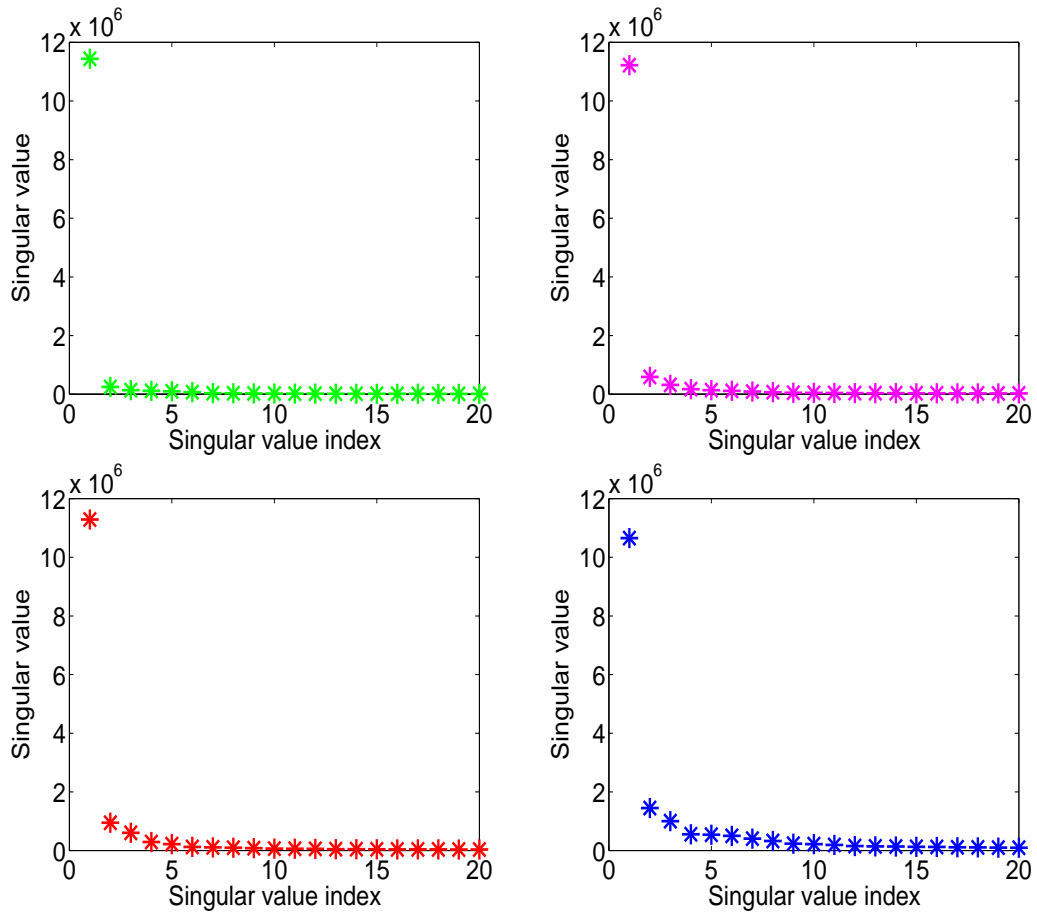


Figure 4.2: **Singular values of the estimated TFS matrix for Example 1.** The first 20 singular values of the estimated TFS matrix when it is the average of 100 estimated TFS matrices (top-left plot in green), 20 estimated TFS matrices (top-right plot in magenta), 10 estimated TFS matrices (bottom-left plot in red) and finally 1 estimated TFS matrix (bottom-right plot in blue). In order to estimate the time-frequency spectrum, we have used the BCMTFSE explained in Chapter 3 with parameters $B = 100$, $BW = 4$, and $K = 7$.

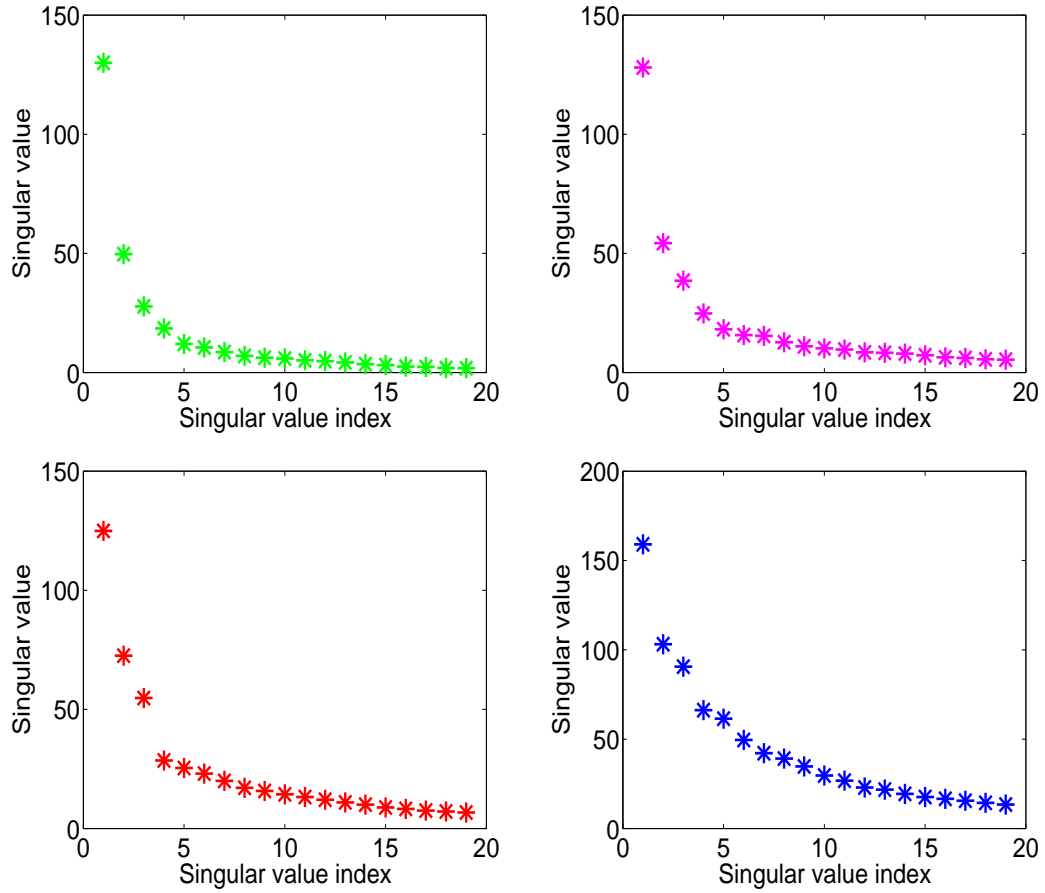


Figure 4.3: **Singular values of the estimated LTFS matrix for Example 1.** The first 20 singular values of the estimated LTFS matrix, starting from the second-largest. The LTFS matrix used to compute the singular values is the average of 100 estimated LTFS matrices (top-left plot in green), 20 estimated LTFS matrices (top-right plot in magenta), 10 estimated LTFS matrices (bottom-left plot in red) and finally 1 estimated LTFS matrix (bottom-right plot in blue). In order to estimate the time-frequency spectrum, we have used the BCMTFSE technique explained in Chapter 3 with parameters $B = 100$, $BW = 4$, and $K = 7$.

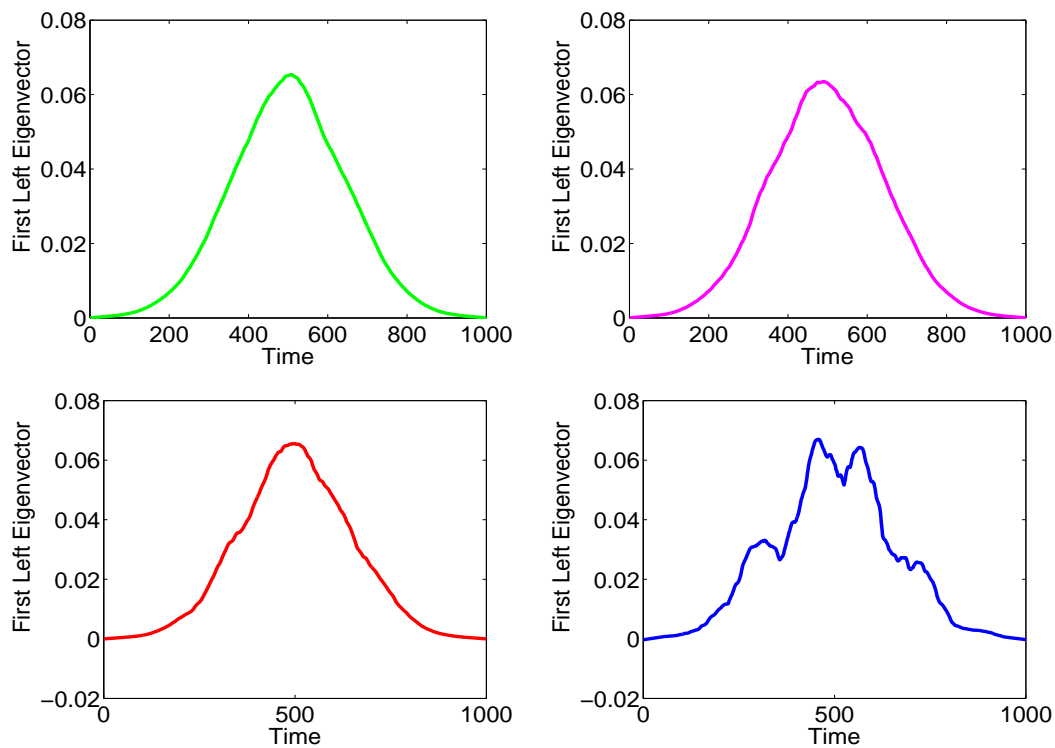


Figure 4.4: **The first left eigenvector of the estimated TFS matrix for Example 1.** The first left eigenvector (corresponding to the largest singular value) of $\widehat{\mathbb{S}}_{\mathbf{x}}$, when the estimated TFS matrix is the average of 100 estimated TFS matrices (top-left plot in green), 20 estimated TFS matrices (top-right plot in magenta), 10 estimated TFS matrices (bottom-right plot in red) and finally 1 estimated TFS matrix (bottom-right plot in blue). In order to estimate the time-frequency spectrum, we have used the BCMTFSE method explained in Chapter 3 with parameters $B = 100$, $BW = 4$, and $K = 7$.

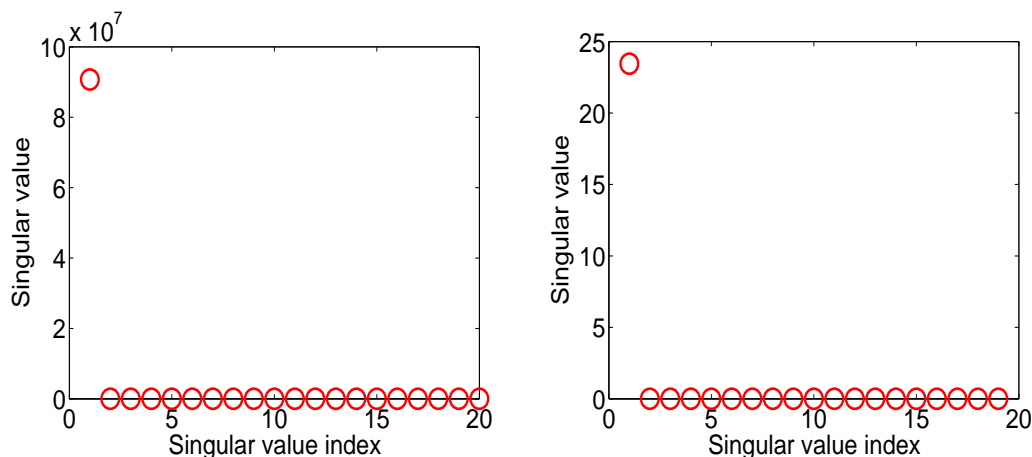


Figure 4.5: **Singular values of the theoretical TFS matrix for Example 2.** The first 20 singular values of the theoretical TFS matrix (left plot) and the first 20 singular values of the theoretical LTFS matrix (right plot), starting from the second-largest.

4.5.2 Example 2

Recall the nonstationary UMP \mathbf{X} introduced in Section 3.9.2, Eq. (3.78). We generate 100 realizations of \mathbf{X} of length $N = 1000$. For each realization, we estimate the time-frequency spectrum of \mathbf{X} using the BCMTFSE (see Chapter 3) at N time points $t \in \{0, 1, \dots, N - 1\}$ and M frequencies $f \in \{f_1, f_2, \dots, f_M\}$ to create the estimated TFS matrix $\widehat{\mathbb{S}}_{\mathbf{X}}$. The final estimates of the TFS matrix are the averages of the estimated TFS matrices over all 100 realizations and over a single realization. We compute the SVD of $\widehat{\mathbb{S}}_{\mathbf{X}}$ and $\log \widehat{\mathbb{S}}_{\mathbf{X}}$ and follow the steps described in section 4.2 in order to draw conclusion about \mathbf{X} .

Figure 4.5 displays the first 20 singular values of $\mathbb{S}_{\mathbf{X}}$ and $\log \mathbb{S}_{\mathbf{X}}$. These two matrices were computed by evaluating the theoretical time-frequency spectrum of \mathbf{X} from Eq. (3.79) and its base-10 logarithm at $t \in \{0, 1, \dots, 1000\}$ and $f \in \{f_1, f_2, \dots, f_M\}$ where $M = 2000$ and $f_k = \frac{k-1}{2M}$. Figure 4.6 displays the first 20 singular values of $\widehat{\mathbb{S}}_{\mathbf{X}}$. Figure 4.7 displays the first 20 singular values of $\log \widehat{\mathbb{S}}_{\mathbf{X}}$ starting from the second-largest. Figure 4.8 displays the first left eigenvector of $\widehat{\mathbb{S}}_{\mathbf{X}}$ as described in step 3 in Section 4.2.

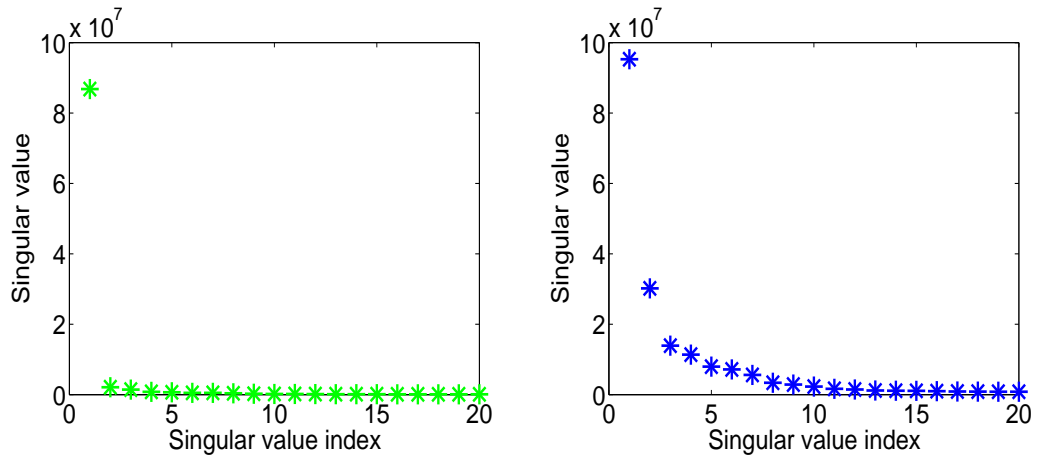


Figure 4.6: **Singular values of the estimated TFS matrix for Example 2.** The first 20 singular values of the estimated TFS matrix when it is the average of 100 estimated TFS matrices (left plot in green), and 1 estimated TFS matrix (right plot in blue). In order to estimate the time-frequency spectrum, we have used the BCMTFSE explained in Chapter 3 with parameters $B = 200$, $BW = 4$, and $K = 7$.

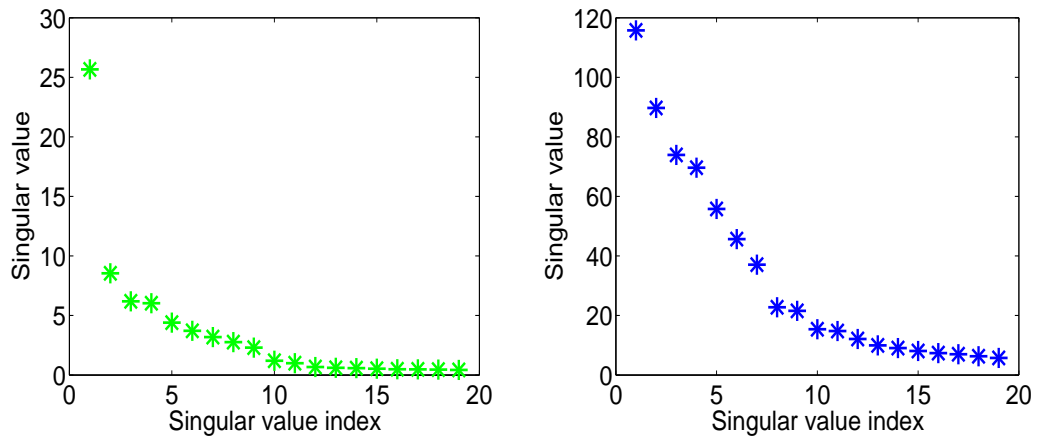


Figure 4.7: **Singular values of the estimated LTFS matrix for Example 2.** The first 20 singular values of the estimated LTFS matrix, starting from the second-largest. The LTFS matrix used to compute the singular values is the average of 100 estimated LTFS matrices (left plot in green), and 1 estimated LTFS matrix (right plot in blue). In order to estimate the time-frequency spectrum, we have used the BCMTFSE technique explained in Chapter 3 with parameters $B = 200$, $BW = 4$, and $K = 7$.

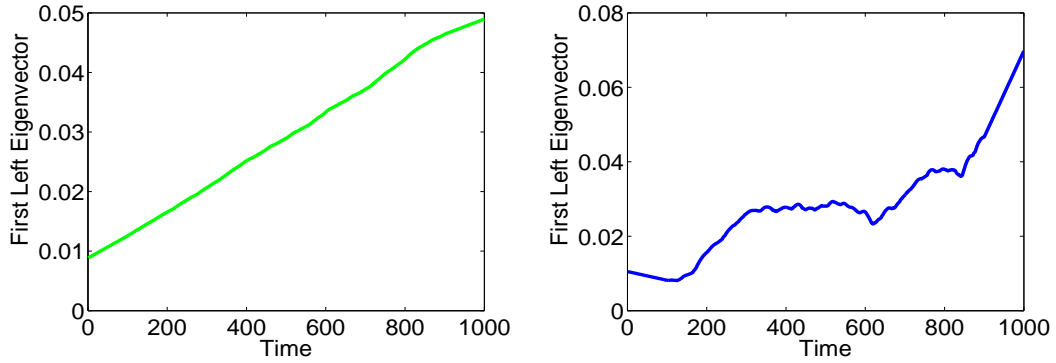


Figure 4.8: **The first left eigenvector of the estimated TFS matrix for Example 2.** The first left eigenvector (corresponding to the largest singular value) of $\widehat{\mathbb{S}}_{\mathbf{X}}$, when the estimated TFS matrix is the average of 100 estimated TFS matrices (left plot in green), and 1 estimated TFS matrix (right plot in blue). In order to estimate the time-frequency spectrum, we have used the BCMTFSE technique explained in Chapter 3 with parameters $B = 200$, $BW = 4$, and $K = 7$.

Following the steps described in Section 4.2, we can say the following. Analyzing the right-hand side plot of Figure 4.6 may lead to two different conclusions. First, if the number of clearly separated singular values is deemed to be 2, we would conclude that \mathbf{X} is nonstationary and is not a UMP. This conclusion is obviously false, and illustrates the weakness of a heuristic visual technique. Second, if the second-largest singular value in the right-hand side plot of Figure 4.6 is not deemed to be clearly separated from the rest, we conclude that the underlying process is a UMP or is stationary. This conclusion would allow us to move to the next step, and examine the singular values of the estimated LTFS matrix, starting from the second-largest (shown in blue in the right-hand side plot of Figure 4.7). It is not clear simply from looking at the plot if the second-largest singular value is clearly separated from the rest, and so one may conclude that \mathbf{X} is stationary. The right-hand side plot of Figure 4.8 gives no support to this conclusion, since the first left eigenvector of $\widehat{\mathbb{S}}_{\mathbf{X}}$ in this plot is obviously not a constant vector. Hence, we can conclude that \mathbf{X} is a UMP.

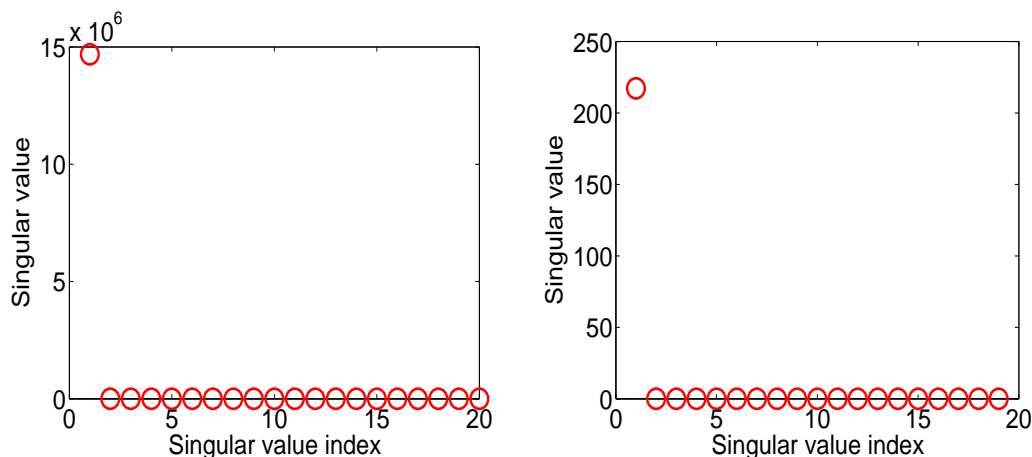


Figure 4.9: **Singular values of the theoretical TFS matrix for Example 3.** The first 20 singular values of the theoretical TFS matrix (left plot) and the first 20 singular values of the theoretical LTFS matrix (right plot), starting from the second-largest.

4.5.3 Example 3

Recall the nonstationary UMP \mathbf{X} introduced in Section 3.9.3, Eq. (3.80). We generate 100 realizations of \mathbf{X} of length $N = 1000$. For each realization, we estimate the time-frequency spectrum of \mathbf{X} using the BCMTFSE (see Chapter 3) at N time points $t \in \{0, 1, \dots, N - 1\}$ and M frequencies $f \in \{f_1, f_2, \dots, f_M\}$ to create the estimated TFS matrix $\widehat{\mathbb{S}}_{\mathbf{X}}$. The final estimates of the TFS matrix are the averages of the estimated TFS matrices over all 100 realizations and over a single realization. We compute the SVD of $\widehat{\mathbb{S}}_{\mathbf{X}}$ and $\log \widehat{\mathbb{S}}_{\mathbf{X}}$ and follow the steps described in section 4.2 in order to draw conclusion about \mathbf{X} .

Figure 4.9 displays the first 20 singular values of $\mathbb{S}_{\mathbf{X}}$ and $\log \mathbb{S}_{\mathbf{X}}$. These two matrices were computed by evaluating the theoretical time-frequency spectrum of \mathbf{X} from Eq. (3.81) and its base-10 logarithm at $t \in \{0, 1, \dots, 1000\}$ and $f \in \{f_1, f_2, \dots, f_M\}$ where $M = 2000$ and $f_k = \frac{k-1}{2M}$. Figure 4.10 displays the first 20 singular values of $\widehat{\mathbb{S}}_{\mathbf{X}}$. Figure 4.11 displays the first 20 singular values of $\log \widehat{\mathbb{S}}_{\mathbf{X}}$ starting from the second-largest. Figure 4.12 displays the first left eigenvector of $\widehat{\mathbb{S}}_{\mathbf{X}}$ as described in step 3 in Section 4.2.

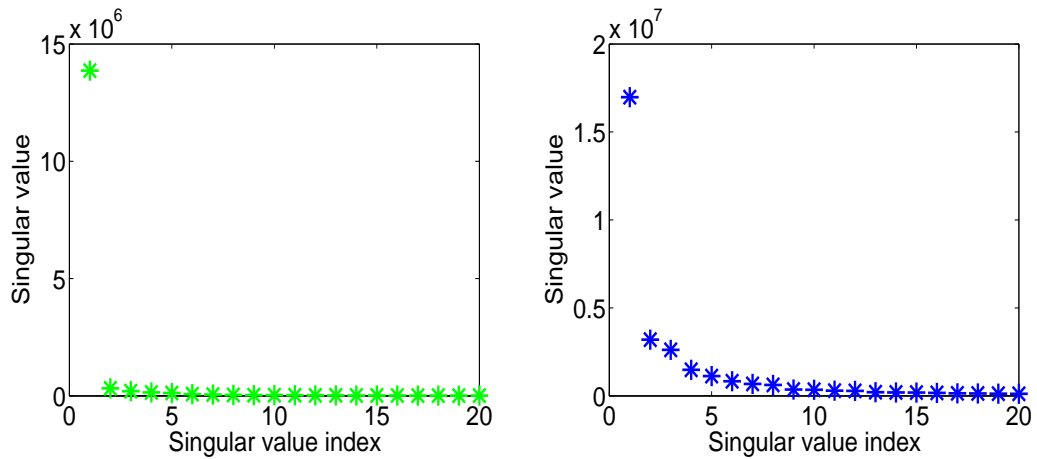


Figure 4.10: **Singular values of the estimated TFS matrix for Example 3.** The first 20 singular values of the estimated TFS matrix when it is the average of 100 estimated TFS matrices (left plot in green), and 1 estimated TFS matrix (right plot in blue). In order to estimate the time-frequency spectrum, we have used the BCMTFSE explained in Chapter 3 with $B = 100$, $BW = 4$, and $K = 7$.

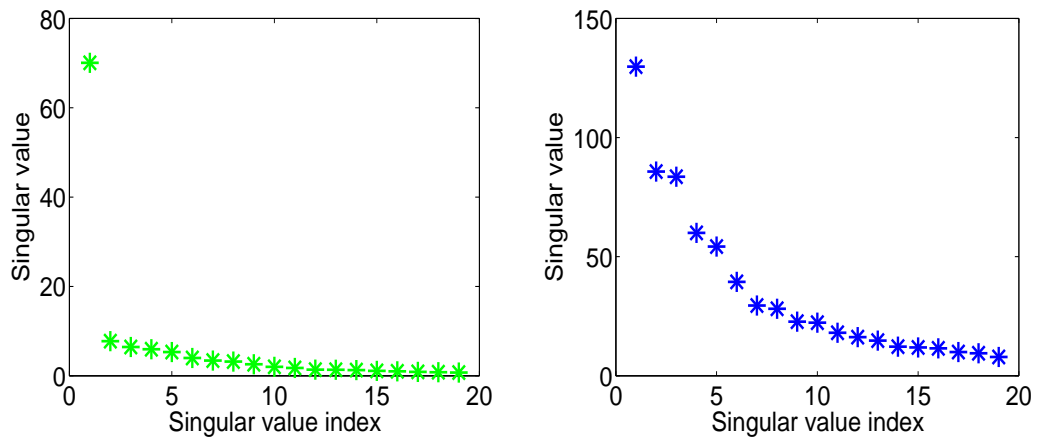


Figure 4.11: **Singular values of the estimated LTFS matrix for Example 3.** The first 20 singular values of the estimated LTFS matrix, starting from the second-largest. The LTFS matrix used to compute the singular values is the average of 100 estimated LTFS matrices (left plot in green), and 1 estimated LTFS matrix (right plot in blue). In order to estimate the time-frequency spectrum, we have used the BCMTFSE technique explained in Chapter 3 with parameters $B = 100$, $BW = 4$, and $K = 7$.

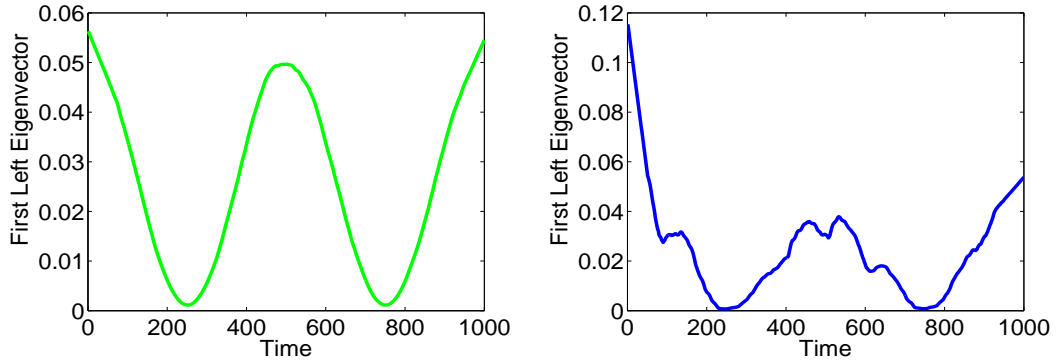


Figure 4.12: **The first left eigenvector of the estimated TFS matrix for Example 3.** The first left eigenvector (corresponding to the largest singular value) of $\widehat{\mathbf{S}}_{\mathbf{X}}$, when the estimated TFS matrix is the average of 100 estimated TFS matrices (left plot in green), and 1 estimated TFS matrix (right plot in blue). In order to estimate the time-frequency spectrum, we have used the BCMTFSE technique explained in Chapter 3 with parameters $B = 100$, $BW = 4$, and $K = 7$.

Following the steps described in Section 4.2, we can say the following. The number of clearly separated singular values in the right-hand side plot of Figure 4.10 is 1, and therefore we conclude that \mathbf{X} is either a UMP or stationary. Examining the singular values of the estimated LTFS matrix, starting from the second-largest (the right-hand side plot of Figure 4.11), one might say that one of the singular values is separated from the rest and therefore conclude that \mathbf{X} is a UMP. If there is any hesitation about this conclusion, the the right-hand side plot of Figure 4.12 can provide additional support for this conclusion, since the first left eigenvector of $\widehat{\mathbf{S}}_{\mathbf{X}}$ is obviously not a constant vector.

4.5.4 Example 4

Recall the nonstationary AR(2) process \mathbf{X} introduced in Section 3.9.4, Eq. (3.84). We generate 100 realizations of \mathbf{X} of length $N = 1000$. For each realization, we estimate the time-frequency spectrum of \mathbf{X} using the BCMTFSE (see Chapter 3) at N time points $t \in \{0, 1, \dots, N - 1\}$ and M frequencies $f \in \{f_1, f_2, \dots, f_M\}$ to create the estimated TFS matrix $\widehat{\mathbf{S}}_{\mathbf{X}}$. The final estimates of the TFS matrix are the averages of the estimated TFS matrices over all 100 realizations and over a single realization.

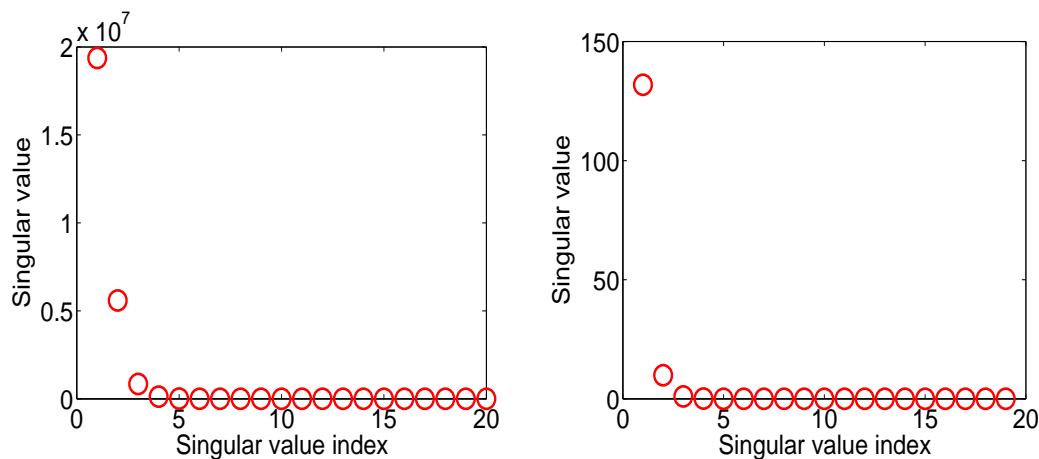


Figure 4.13: **Singular values of the theoretical TFS matrix for Example 4.** The first 20 singular values of the theoretical TFS matrix (left plot) and the first 20 singular values of the theoretical LTFS matrix (right plot) starting from the second-largest.

We compute the SVD of $\widehat{\mathbb{S}}_{\mathbf{X}}$ and $\log \widehat{\mathbb{S}}_{\mathbf{X}}$ and follow the steps described in section 4.2 in order to draw conclusion about \mathbf{X} .

Figure 4.13 displays the first 20 singular values of $\mathbb{S}_{\mathbf{X}}$ and $\log \mathbb{S}_{\mathbf{X}}$. These two matrices were computed by evaluating the theoretical time-frequency spectrum of \mathbf{X} from Eq. (3.86) and its base-10 logarithm at $t \in \{0, 1, \dots, 1000\}$ and $f \in \{f_1, f_2, \dots, f_M\}$ where $M = 2000$ and $f_k = \frac{k-1}{2M}$. Figure 4.14 displays the first 20 singular values of $\widehat{\mathbb{S}}_{\mathbf{X}}$. Figure 4.15 displays the first 20 singular values of $\log \widehat{\mathbb{S}}_{\mathbf{X}}$ starting from the second-largest. Figure 4.16 displays the first left eigenvector of $\widehat{\mathbb{S}}_{\mathbf{X}}$ as described in step 3 in Section 4.2.

Following the steps described in Section 4.2, we can say the following. The number of clearly separated singular values in the right-hand side plot of Figure 4.14 is 1, and therefore we conclude that \mathbf{X} is either a UMP or stationary. At this point, we know that this conclusion is false, but we continue to the second step. Examining the singular values of the estimated LTFS matrix, starting from the second-largest (shown in blue in the right-hand side plot of Figure 4.15), one can see that the number of clearly separated singular values is 2, and this disagrees with the conclusion made in the previous step. More specifically, if \mathbf{X} is stationary or a UMP, the number of

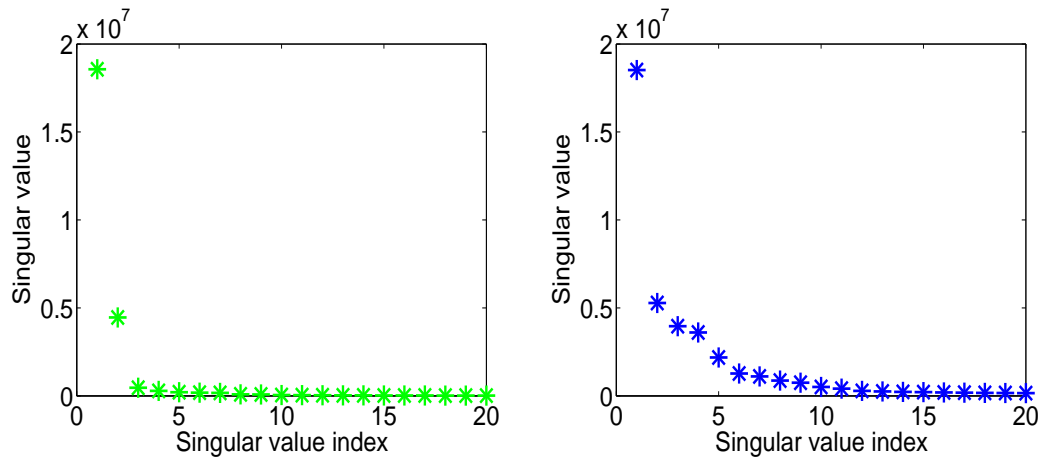


Figure 4.14: **Singular values of the estimated TFS matrix for Example 4.** The first 20 singular values of the estimated TFS matrix when it is the average of 100 estimated TFS matrices (left plot in green), and 1 estimated TFS matrix (right plot in blue). In order to estimate the time-frequency spectrum, we have used the BCMTFSE explained in Chapter 3 with parameters $B = 100$, $BW = 4$, and $K = 7$.

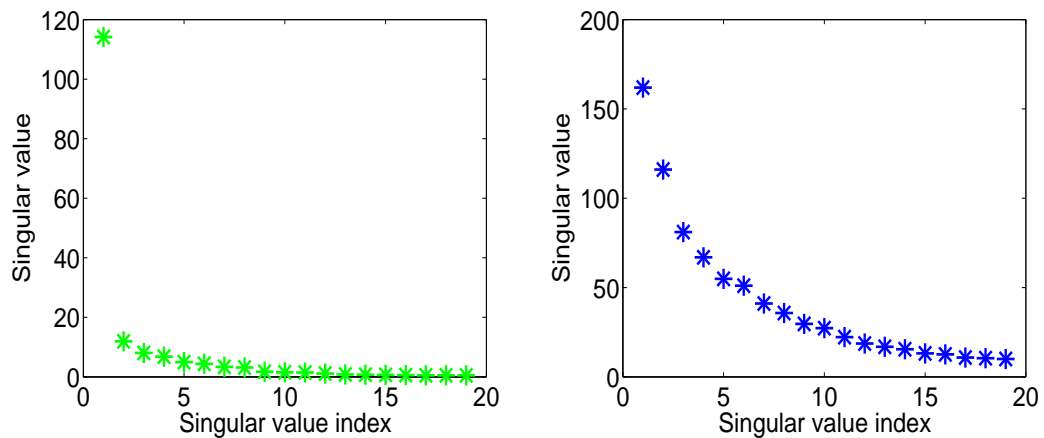


Figure 4.15: **Singular values of the estimated LTFS matrix for Example 4.** The first 20 singular values of the estimated LTFS matrix starting from the second-largest. The LTFS matrix used in computing the singular values is the average of 100 estimated LTFS matrices (left plot in green), and 1 estimated LTFS matrix (right plot in blue). In order to estimate the time-frequency spectrum, we have used the BCMTFSE explained in Chapter 3 with parameters $B = 100$, $BW = 4$, and $K = 7$.

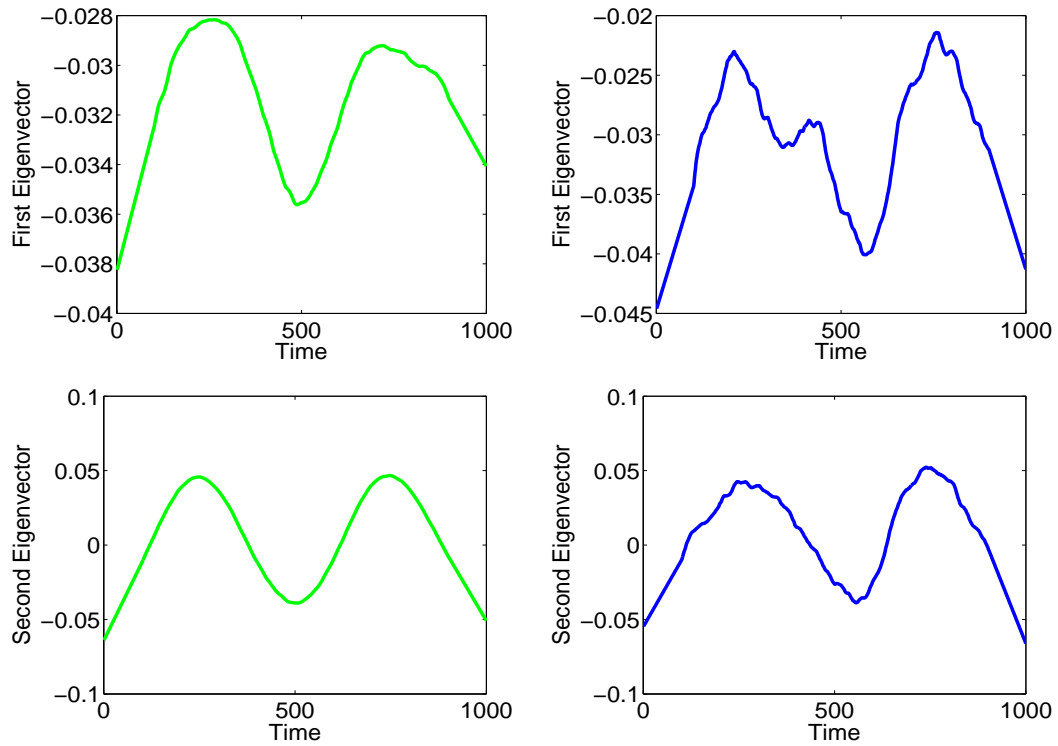


Figure 4.16: **The first and second left eigenvectors of the estimated TFS matrix for Example 4.** The first (top plots) and second (bottom plots) left eigenvectors of $\widehat{S}_{\mathbf{X}}$, when the estimated TFS matrix is the average of 100 estimated TFS matrices (left plots in green), and 1 estimated TFS matrix (right plot in blue). In order to estimate the time-frequency spectrum, we have used the BCMTFSE method explained in Chapter 3 with parameters $B = 100$, $BW = 4$, and $K = 7$.

clearly separated singular values of $\log \widehat{\mathbb{S}}_{\mathbf{X}}$, starting from the second-largest should not exceed 1. An examination of the first two left eigenvectors of $\widehat{\mathbb{S}}_{\mathbf{X}}$, shown in the right-hand side plots of Figure 4.16, supports this disagreement since the second left eigenvector does not appear to be noise and in fact appears to follow a systematic pattern. As a result of the observations from the second and third steps, we can recover from the false conclusion made in the first step by saying that \mathbf{X} is not a UMP. We note that the false conclusion in the first step is based on the fact that the second singular value does not appear clearly separated from the rest of the singular values, even though its size is still relatively large.

4.5.5 Example 5

Let $\mathbf{X} = \{X_t\}_{t \in \mathbb{Z}}$ be a discrete-time UMP of the form

$$X_t = \cos(2\pi f_s t) Y_t, \quad t \in \mathbb{Z}, \quad (4.2)$$

where $f_s = 0.002$ is a fixed frequency, and $\mathbf{Y} = \{Y_t\}_{t \in \mathbb{Z}}$ is the fourth-order autoregressive process [Percival and Walden 1993]

$$Y_t = 2.7607Y_{t-1} - 3.8106Y_{t-2} + 2.6535Y_{t-3} - 0.9238Y_{t-4} + \varepsilon_t, \quad \forall t \in \mathbb{Z}. \quad (4.3)$$

Here $\{\varepsilon_t\}_{t \in \mathbb{Z}}$ is a stationary white noise process with variance 10^4 . The spectrum of \mathbf{Y} , $S_{\mathbf{Y}}$, follows the form shown in Eq. (3.85) where $a_1 = 2.7607$, $a_2 = -3.8106$, $a_3 = 2.6535$, and $a_4 = -0.9238$.

The theoretical time-frequency spectrum of \mathbf{X} is given by

$$S_{\mathbf{X}}(t, f) = \cos^2(2\pi f_s t) S_{\mathbf{Y}}(f), \quad t \in \mathbb{Z}, f \in [-1/2, 1/2]. \quad (4.4)$$

We generate 100 realizations of \mathbf{X} of length $N = 1000$. For each realization, we

estimate the time-frequency spectrum of \mathbf{X} using the BCMTFSE (see Chapter 3) at N time points $t \in \{0, 1, \dots, N-1\}$ and M frequencies $f \in \{f_1, f_2, \dots, f_M\}$ to create the estimated TFS matrix $\widehat{\mathbf{S}}_{\mathbf{X}}$. The final estimates of the TFS matrix are taken to be the averages of the estimated TFS matrices over all 100 realizations and over a single realization.

We compute the SVD of $\widehat{\mathbf{S}}_{\mathbf{X}}$, and use the observation that $C_t = \cos(2\pi f_s t) = 1$ when $t = 500$. By the scheme explained in Section 4.3, \vec{G} and \vec{C} can be estimated up to a normalizing factor. We estimate \vec{C} and \vec{G} when the estimated TFS matrix is the average of 100 TFS matrices, as follows.

Assuming each realization is in the form of a length- N column vector $\vec{X}^{(k)}$, we divide each realization $\vec{X}^{(k)}$ by \vec{C} to obtain new realizations $Y_0^{(k)}, Y_1^{(k)}, \dots, Y_{N-1}^{(k)}$ (see Section 4.4). For this particular example, \vec{C} has non-zero entries. We use the multitaper spectrum estimator to estimate the spectrum for each realization $Y_0^{(k)}, Y_1^{(k)}, \dots, Y_{N-1}^{(k)}$, and take the final multitaper estimate to be the average of all 100 multitaper spectrum estimates. Denoting the final multitaper spectrum by \vec{S}_M , we get the ITFSE, $S_{\mathbf{X}}^I = \widehat{\vec{G}}\vec{S}_M$, as explained in Section 4.4. We repeat this process using only 1 realization.

Figure 4.17 compares the performance of the BCMTFSE and the ITFSE when using 100 realizations (top plots) or only 1 realization (bottom plots). We note that in this example, for a fixed time point, the theoretical time-frequency spectrum has closely-spaced peaks along the frequency direction. Similarly, for a fixed frequency, the time-frequency spectrum has a “rapid” variation along the time direction. As was mentioned in Chapter 3, blocking the data is an effective way to estimate the time-frequency spectrum with good time resolution. This is done by selecting a sufficiently small block size relative to the sample size. The right-hand side plots in Figure 4.17 (in red) demonstrate the good time resolution of the BCMTFSE. As a result of focusing on improving the time resolution of the time-frequency spectrum

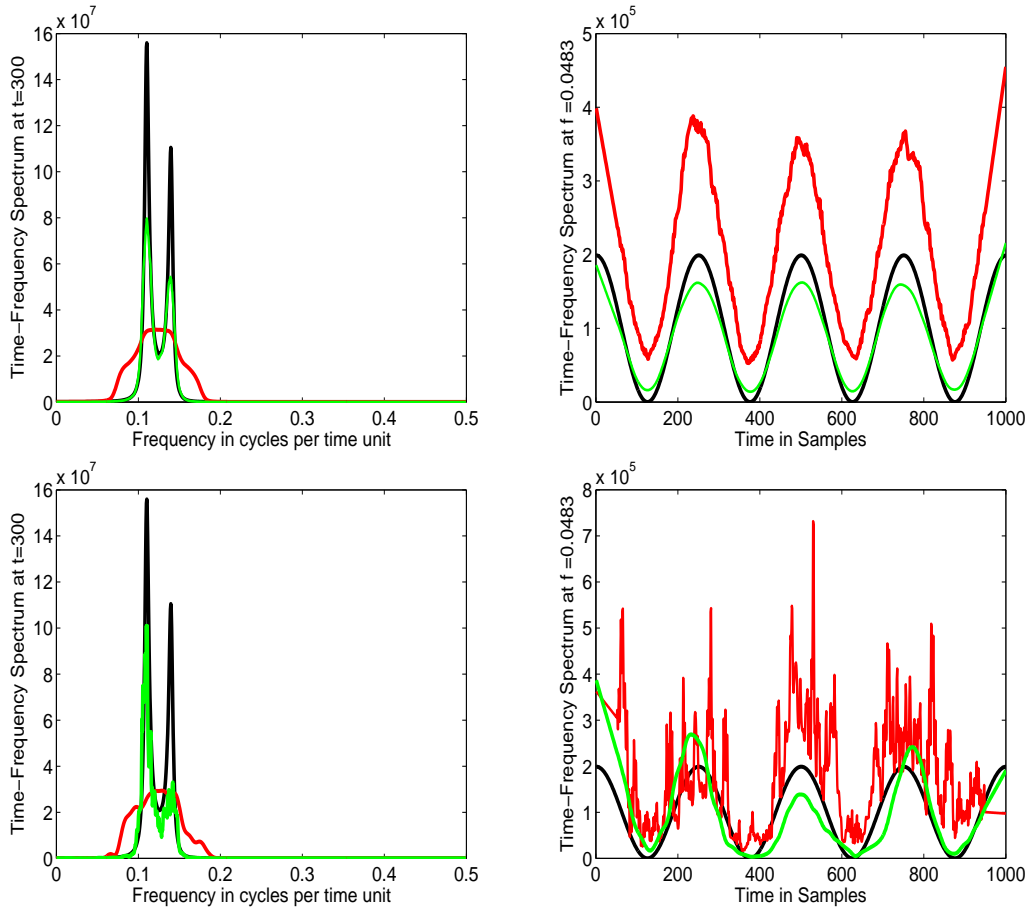


Figure 4.17: **Comparison of the BCMTFSE, ITFSE and the time-frequency spectrum for Example 5.** Time-frequency spectrum (black line), BCMTFSE (red line) and ITFSE (green line) at $f = 0.0483$ (right) and $t = 300$ (left) for Example 5. The ITFSE is taken to be the average over 100 realizations (top plots) and over a single realization (bottom plots). The relevant parameters are $B = 100$, $W = 0.04$, and $K = 7$.

estimate, the frequency resolution decreases to the point of oversmoothing the two closely-spaced peaks in this example. This can be easily seen in the left-hand side plots of Figure 4.17 (in red). Since the underlying process in this example is a UMP, its frequency resolution can be improved using the ITFSE as described in Section 4.4. This improvement can be seen in the left-hand side plots of Figure 4.17 (in green). The frequency resolution improvement has obviously affected the time-frequency spectrum estimate in the time direction by adjusting the level of power. This can be seen in the right-hand side plots of Figure 4.17 (in green).

4.6 Conclusion

In this chapter, we introduced a graphical technique which, given a realization of nonstationary process \mathbf{X} , uses the BCMTFSE to draw conclusions about the class of processes \mathbf{X} belongs to. If the conclusion is that \mathbf{X} is a UMP, we introduced a new time-frequency spectrum estimator which has empirically better frequency resolution than the BCMTFSE. The use of these techniques was illustrated using several example nonstationary processes belonging to different classes.

Chapter 5

Unfolding Aliases in Bivariate Time Series

The well-known Shannon-Whittaker sampling (interpolation) theorem states that if a bandlimited continuous-time signal is sampled with a sampling rate greater than twice the highest frequency component present in the signal, then the samples are sufficient to uniquely reconstruct the original signal. If this condition is not met by the sampling procedure, the phenomenon of *aliasing* occurs. That is, frequencies at or exceeding the Nyquist frequency are “folded back” or “aliased” into the Nyquist band $[-\mathcal{F}_n, \mathcal{F}_n)$, (or just $[0, \mathcal{F}_n)$ for real-valued processes) where $\mathcal{F}_n \triangleq 1/(2\Delta T)$ cycles per unit of the sampling interval ΔT . To make reliable inferences about the observed signal, it is preferable to avoid having aliases. This is usually accomplished either by sampling appropriately, or by band-limiting the signal, *i.e.*, by applying a low-pass filter prior to sampling (see Section 2.2 for details). There are, however, circumstances where it is impossible to low-pass filter prior to sampling. Therefore it is of practical interest to have techniques available to detect when aliasing occurs in a sampled signal and, if possible, to “unfold” the aliased frequencies.

In order to make such detections, it is evident that additional information is

required, beyond that which is contained in a single realization. Let $\{\mathcal{W}(t)\}_{t \in \mathbb{R}}$ be a continuous-time real-valued process with “mixed spectrum”. Let $\mathbf{X} \triangleq \{X_t\}_{t \in \mathbb{Z}}$ and $\mathbf{Y} \triangleq \{Y_t\}_{t \in \mathbb{Z}}$ be two real-valued processes. Assume $X_t = \mathcal{W}(t\Delta T) + \zeta(t\Delta T)$, where $\Delta T > 0$ is the sampling interval and $\{\zeta(t)\}_{t \in \mathbb{R}}$ is a continuous-time stationary noise process. Assume further that $Y_t = \mathcal{W}(t\Delta T + \tau) + \varepsilon(t\Delta T)$, where $\tau \leq \Delta T$ is the *time delay* between \mathbf{X} and \mathbf{Y} and $\{\varepsilon(t)\}_{t \in \mathbb{R}}$ is a continuous-time stationary noise process independent from $\{\zeta(t)\}_{t \in \mathbb{R}}$. In this chapter, we describe a technique to detect aliased frequency content, given a bivariate time series $\{(X_t, Y_t) : t = 0, 1, \dots, N - 1\}$. In this case, aliasing can be seen to manifest as departures from the expected linearity of the phase function [Rögnvaldsson 1993] of the complex coherency between \mathbf{X} and \mathbf{Y} .

In Section 5.1, we introduce the *phase function* of the complex coherency between \mathbf{X} and \mathbf{Y} , which is a linear function of frequency, and the process by which this phase line and unaliased frequencies are folded into the Nyquist band. In Section 5.2, we describe the process of “unfolding” the phase line to estimate the unaliased frequencies corresponding to estimated aliased frequencies of interest, which in this thesis are those frequencies of suspected line components in the signal. To clarify the unfolding technique proposed in Section 5.2, we apply it in Section 5.3 to simulated data generated by a process consisting of line components embedded in white noise. The technique is also applied to daily solar noon flux data compiled by the National Geophysical Data Center (NGDC) of the National Oceanic and Atmospheric Administration. We use a set of bivariate data corresponding to a pair of terrestrial observation stations with approximately twelve hours of longitudinal time difference. Here, the longitudinal time difference plays the role of the time delay mentioned above, since the two stations observe the same signal. Concluding remarks are made in Section 5.4. In computations requiring estimates of spectra or coherence, we employ the multitaper methods developed by Thomson [1982]. These methods, as well

as techniques for bias reduction and variance estimation via jackknifing, are reviewed in Appendices B and D.

5.1 Coherence, Time Delay, and Aliasing

In the physical sciences, spectral analysis is used to study the frequency-domain behaviour of systems. When two systems are being studied simultaneously, a technique known as *coherence analysis* can be used to study the interrelationships between the two systems in the frequency domain. Indeed, coherence analysis essentially provides a frequency-domain analogue of the notion of cross-correlation in the time-domain.

In the following, we will assume that all processes are zero-mean and have finite variance. Let $\mathbb{R}_{>0}$ denote the set of positive real numbers. Assume $\mathbf{X} \triangleq \{X_t\}_{t \in \mathbb{Z}}$ and $\mathbf{Y} \triangleq \{Y_t\}_{t \in \mathbb{Z}}$ are two real-valued processes. The *coherence* between \mathbf{X} and \mathbf{Y} is a complex-valued function of frequency, denoted by $C_{\mathbf{XY}}$, and is defined in Eq. (D.1) in Appendix D. The *magnitude-squared coherence* (MSC) between \mathbf{X} and \mathbf{Y} , denoted by $\gamma_{\mathbf{XY}}$, is defined by $\gamma_{\mathbf{XY}}(f) \triangleq |C_{\mathbf{XY}}(f)|^2$ (see Appendix D).

The complex-valued coherence, $C_{\mathbf{XY}}$, can be represented in polar form at each frequency f as

$$C_{\mathbf{XY}}(f) = \alpha(f)e^{i\varphi(f)}, \quad \forall f \in \mathbb{R}, \quad (5.1)$$

where α and φ are, respectively, the real-valued *coherence amplitude function* and *coherence phase function*. In the following, the coherence amplitude function and coherence phase function will be referred to simply as the *amplitude function* and *phase function*, respectively. It is clear from the polar form of $C_{\mathbf{XY}}$ that the MSC satisfies $\gamma_{\mathbf{XY}} = \alpha^2$. We assume that there exists a continuous-time real-valued process

$\mathcal{U}_c \triangleq \{\mathcal{U}(t)\}_{t \in \mathbb{R}}$ such that

$$X_t = \mathcal{U}(t\Delta T) + \zeta(t\Delta T) \quad \text{and} \quad Y_t = \mathcal{U}(t\Delta T + \tau) + \varepsilon(t\Delta T), \quad (5.2)$$

for all $t \in \mathbb{Z}$, where $\Delta T \in \mathbb{R}_{>0}$ is the sampling interval, $\tau \in \mathbb{R}_{>0}, \tau < \Delta T$, is the *time delay* between \mathbf{X} and \mathbf{Y} , and $\mathbf{T} \triangleq \{\zeta(t)\}_{t \in \mathbb{R}}$ and $\mathbf{E} \triangleq \{\varepsilon(t)\}_{t \in \mathbb{R}}$ are two continuous-time, independent stationary noise processes representing the measurement or instrument error. We further assume that \mathcal{U}_c has a mixed spectrum (see Appendix C). Recalling Eq. (C.1) from Appendix C, we have

$$\mathcal{U}(t) = \sum_{j=1}^J D_j \cos(2\pi g_j t + \theta_j) + \vartheta(t), \quad \forall t \in \mathbb{Z},$$

where each $g_j, D_j, \theta_j \in \mathbb{R}$ and $\vartheta \triangleq \{\vartheta(t)\}_{t \in \mathbb{R}}$ is a continuous-time stationary noise process independent from \mathbf{T} and \mathbf{E} .

The *extended Cramér representation* or *spectral representation* (see [Munk and Hasselmann 1964] or [Brockwell and Davis 1987] for details) of \mathcal{U}_c is given by

$$\mathcal{U}(t) = \int_{\mathbb{R}} e^{i2\pi ft} dZ_{\mathcal{U}_c}(f), \quad \forall t \in \mathbb{R}, \quad (5.3)$$

where for $\mu_j = \frac{D_j e^{i\theta_j}}{2}$,

$$dZ_{\mathcal{U}_c}(f) = \sum_{j=1}^J [\mu_j \delta(f - g_j) df + \overline{\mu_j} \delta(f + g_j) df] + dZ_{\vartheta}(f). \quad (5.4)$$

Here δ denotes the Dirac delta function, the overline denotes complex conjugation, and $\{Z_{\vartheta}(f)\}_{f \in \mathbb{R}}$ is an orthogonal-increment process associated with ϑ . The processes $\mathbf{X}, \mathbf{Y}, \mathbf{T}, \mathbf{E}$ and ϑ also have (extended) spectral representations of the form shown

in Eq. (B.1). For example,

$$\vartheta(t) = \int_{\mathbb{R}} e^{i2\pi ft} dZ_{\vartheta}(f), \quad t \in \mathbb{R}.$$

We note that an advantage of using the extended Cramér representation is that spectrum analysis and harmonic analysis are made distinct; indeed, the “harmonic” part of \mathcal{W}_c is determined by the first moment of $dZ_{\mathcal{W}_c}$, while its spectrum of the continuous part is determined by the second central moment of $dZ_{\mathcal{W}_c}$. This distinction avoids many of the problems incurred by lumping discrete and continuous spectra together [see Wiener 1949, page 59].

Using the extended Cramér representations for \mathbf{X} and \mathbf{Y} and using Eq. (5.2), we see that

$$dZ_{\mathbf{X}}(f) = dZ_{\mathcal{W}_c}(f) + dZ_{\mathbf{T}}(f), \quad \forall t \in \mathbb{R} \quad (5.5)$$

and

$$dZ_{\mathbf{Y}}(f) = e^{i2\pi f\tau} dZ_{\mathcal{W}_c}(f) + dZ_{\mathbf{E}}(f), \quad \forall t \in \mathbb{R}, \quad (5.6)$$

where $\{Z_{\mathbf{T}}(f)\}_{f \in \mathbb{R}}$ and $\{Z_{\mathbf{E}}(f)\}_{f \in \mathbb{R}}$ are the orthogonal-increment processes associated with \mathbf{T} and \mathbf{E} , and $\{Z_{\mathbf{X}}(f)\}_{f \in \mathbb{R}}$ and $\{Z_{\mathbf{Y}}(f)\}_{f \in \mathbb{R}}$ are processes associated with \mathbf{X} and \mathbf{Y} . We define the spectra of \mathbf{X} and \mathbf{Y} by $\mathbf{E}\{|dZ_{\mathbf{X}}(f)|^2\} = S_{\mathbf{X}}(f) df$ and $\mathbf{E}\{|dZ_{\mathbf{Y}}(f)|^2\} = S_{\mathbf{Y}}(f) df$, and the cross-spectrum [Priestley 1981] between \mathbf{X} and \mathbf{Y} by

$$\mathbf{E}\{dZ_{\mathbf{X}}(f) \overline{dZ_{\mathbf{Y}}(f)}\} = S_{\mathbf{XY}}(f) df.$$

We have

$$S_{\mathbf{X}}(f) = \sum_{j=1}^J |\mu_j|^2 \delta(f - g_j) + |\mu_j|^2 \delta(f + g_j) + S_{\boldsymbol{\vartheta}}(f) + S_{\mathbf{T}}(f), \quad \forall f \in \mathbb{R} \quad (5.7)$$

$$S_{\mathbf{Y}}(f) = \sum_{j=1}^J |\mu_j|^2 \delta(f - g_j) + |\mu_j|^2 \delta(f + g_j) + S_{\boldsymbol{\vartheta}}(f) + S_{\mathbf{E}}(f), \quad \forall f \in \mathbb{R}, \quad (5.8)$$

where $S_{\boldsymbol{\vartheta}}(f) df = \mathbb{E}\{|dZ_{\boldsymbol{\vartheta}}(f)|^2\}$, $S_{\mathbf{T}}(f) df = \mathbb{E}\{|dZ_{\mathbf{T}}(f)|^2\}$, and $S_{\mathbf{E}}(f) df = \mathbb{E}\{|dZ_{\mathbf{E}}(f)|^2\}$.

Similarly, the cross spectrum $S_{\mathbf{XY}}$ is given by

$$S_{\mathbf{XY}}(f) = e^{-i2\pi f\tau} \left[\sum_{j=1}^J |\mu_j|^2 \delta(f - g_j) + |\mu_j|^2 \delta(f + g_j) + S_{\boldsymbol{\vartheta}}(f) \right], \quad \forall f \in \mathbb{R}.$$

Substituting the above expressions for $S_{\mathbf{X}}$, $S_{\mathbf{Y}}$, and $S_{\mathbf{XY}}$ into Eq. (D.1), and comparing the result with Eq. (5.1), we obtain the following expressions for the amplitude and phase functions:

$$\alpha(f) = \frac{\sum_{j=1}^J |\mu_j|^2 \delta(f - g_j) + |\mu_j|^2 \delta(f + g_j) + S_{\boldsymbol{\vartheta}}(f)}{\sqrt{S_{\mathbf{X}}(f)} \sqrt{S_{\mathbf{Y}}(f)}}, \quad \forall f \in \mathbb{R}, \quad (5.9)$$

$$\varphi(f) = -2\pi f\tau, \quad \forall f \in \mathbb{R}. \quad (5.10)$$

It is clear from Eq. (5.10) that the phase function is a linear function of the radian frequency $2\pi f$, passing through the origin, with slope $-\tau$. The graph of the phase function will be called the *phase line*. Here, for ease of interpretation, we keep the phase unit as degrees. In particular, if τ is the time delay in seconds, Eq. (5.10) becomes

$$\varphi(f) = -360 \times f \times \tau, \quad (5.11)$$

where 360 is the number of degrees per cycle and f is frequency in Hertz.

Remark 5.1.1 *The time delay can also be taken to be $\Delta T - \tau$. Let $\tilde{X}_t = X_{t+1}$ for*

each $t \in \mathbb{Z}$ and set $\tilde{\mathbf{X}} \triangleq \{\tilde{X}_t\}_{t \in \mathbb{Z}}$. In this case, the initial sampling time of \mathbf{Y} is less than that of $\tilde{\mathbf{X}}$, with a time delay of $\Delta T - \tau$ between the two processes. After calculating $S_{\mathbf{Y}\tilde{\mathbf{X}}}(f)$, in the coherence between \mathbf{Y} and $\tilde{\mathbf{X}}$ the amplitude function from Eq. (5.9) remains the same and the phase function from Eq. (5.10) has $\Delta T - \tau$ substituted for τ .

Looking at the amplitude function at different frequency components, it is easy to see that $\alpha(f) \approx 1$ if the power of the measurement errors, $S_{\mathbf{T}}(f)$ and $S_{\mathbf{E}}(f)$, at f are small relative to the power of the background noise, $S_{\mathfrak{g}}(f)$. Also, of relevance in Section 5.2, $\alpha(f) \approx 1$ in the presence of a strong line component (*i.e.*, a g_j at which μ_j is large relative to the noise power). Because of this, it is easy to see that the only factor that distinguishes the coherence at such frequencies is the value of the phase function.

When plotted, the phase-frequency (P-F) pairs from Eq. (5.11) form a *P-F plot*. In the following illustrations, we only consider positive frequencies since φ is an odd function of frequency. According to Eq. (5.11), the phase at positive integer multiples of the Nyquist frequency $\mathcal{F}_n = 1/(2\Delta T)$ in cycles per second is

$$\varphi_j = -360 \times \tau \times j\mathcal{F}_n = -180 \times \frac{\tau}{\Delta T} \times j, \quad j \in \{1, 2, 3, \dots\}. \quad (5.12)$$

Assume that we have five P-F pairs $p_k = (f_k, \varphi(f_k))$, $k \in \{1, 2, 3, 4, 5\}$ lying on the phase line, one of whose frequencies is smaller than the Nyquist frequency, as shown in Figure 5.1. The P-F pairs on the phase line are called the *unaliased pairs* and their first components f_k , are called the *unaliased frequencies*. This is illustrated in Figure 5.1(a). The phase line has been shown up to $f = 4\mathcal{F}_n$ with the phases φ_j at $j\mathcal{F}_n$, $j \in \{1, 2, 3, 4\}$; the five P-F pairs p_k , $k \in \{1, 2, 3, 4, 5\}$, are shown clearly on the phase line.

Recall that the Nyquist criterion places a limitation on the highest frequency

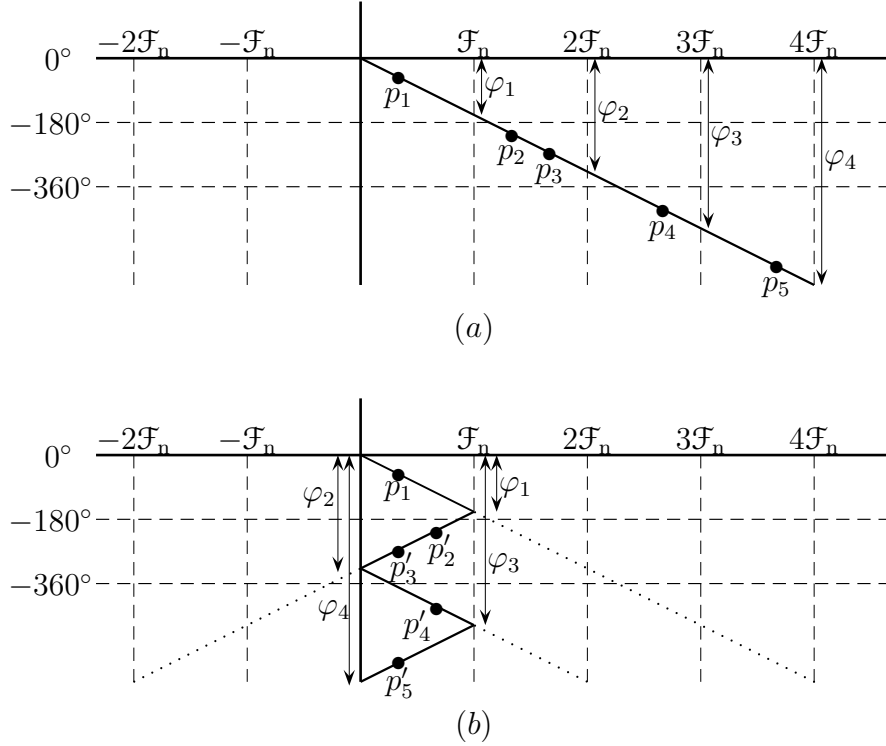


Figure 5.1: **Illustration of the folding process of the phase line.** The vertical axis is the phase axis (in degrees), and the horizontal axis is the frequency axis (in cycles/time unit). Figure 5.1(a) shows the phase line and five P-F pairs p_1, p_2, p_3, p_4, p_5 . Figure 5.1(b) shows the completed folding process of the phase line inside the Nyquist band while maintaining the phases φ_j , $j \in \{1, 2, 3, 4\}$ inside this band. In Figure (b), the line containing the point p_1 is the *zeroth alias* (corresponding to $a = 0$). The line containing the points p'_2 and p'_3 , originally in the $[\mathcal{F}_n, 2\mathcal{F}_n)$ frequency band is the *first alias line* (corresponding to $a = 1$). The line containing the point p'_4 , originally in the $[2\mathcal{F}_n, 3\mathcal{F}_n)$ frequency band is the *second alias line* (corresponding to $a = 2$). Finally, the line containing the point p'_5 , originally in the $[3\mathcal{F}_n, 4\mathcal{F}_n)$ frequency band, is the *third alias line* (corresponding to $a = 3$). The dotted lines show the track of the phase line during folding.

of a signal which can be unambiguously represented in a frequency-domain representation of the signal following sampling (this limitation is, of course, reflected in any frequency-domain analysis technique based on samples, *e.g.*, coherence analysis). Loosely speaking, any frequency exceeding the Nyquist frequency will be “folded back” into the Nyquist band $[0, \mathcal{F}_n)$, and this folding procedure places the entire phase line inside the Nyquist band. The folding process into the Nyquist band is known as *aliasing*; accordingly, the folded frequencies are known as *aliased frequencies*.

Consider the P-F plot and the phase line shown in Figure 5.1(a)—the folding process of this phase line is shown in Figure 5.1(b). As can be seen, the phase line, including all the P-F pairs in the P-F plot, folds back and forth at the Nyquist frequency \mathcal{F}_n and zero frequency, while maintaining the phases φ_j , $j \in \{1, 2, 3, 4\}$, from Eq. (5.12) inside the Nyquist band. This process continues, until all P-F pairs in the P-F plot appear in the interval $[0, \mathcal{F}_n)$. The P-F pairs $p'_k = (f'_k, \varphi(f_k))$, $k \in \{2, 3, 4, 5\}$, appearing in the Nyquist band in Figure 5.1(b) are called *aliased pairs*. These aliased pairs differ from the unaliased P-F pairs $p_k = (f_k, \varphi(f_k))$ on the phase line only in their first component, *i.e.*, the aliased frequencies. We also refer to unaliased P-F pairs whose frequency is not changed by the folding process, (*i.e.*, that lie in the Nyquist band on the phase line), as aliased pairs when we think of them as lying on the folded phase line. Thus, in Figure 5.1(b), the P-F pair p_1 is thought of as an aliased pair even though the folding process of the phase line has not changed the value of f_1 .

The folded phase line inside the Nyquist band creates a set of lines called the *aliased phase lines* or *alias lines*. Each alias line inside the Nyquist band can be represented by a nonnegative integer a . The integer a is called its *alias number*; it corresponds to the position of the alias line in the translated Nyquist band $[a\mathcal{F}_n, (a+1)\mathcal{F}_n)$. We note that $a = 0$ indicates that for the first alias line, the position of this line in the Nyquist band and the translated Nyquist band are the same. In our example,

$a \in \{0, 1, 2, 3\}$, since the final translated Nyquist band is $[3\mathcal{F}_n, 4\mathcal{F}_n)$.

Knowing the true alias line or alias number related to a given aliased frequency allows us to determine the original (unaliased) position of that frequency. This is essentially following the procedure of Figure 5.1 backwards. We call this backwards process *unfolding* of the phase line, which uses the aliased frequencies and their related alias numbers to deduce the unaliased frequencies.

For example, comparing the aliased and unaliased P-F pairs from Figure 5.1(a) and Figure 5.1(b), we obtain $f_2 = 2\mathcal{F}_n - f'_2$, $f_3 = 2\mathcal{F}_n - f'_3$, $f_4 = 2\mathcal{F}_n + f'_4$, and $f_5 = 4\mathcal{F}_n - f'_5$. Generally, denoting an aliased frequency by f' and an unaliased frequency by f , we have

$$f = \begin{cases} a_{f'}\mathcal{F}_n + f', & a_{f'} \text{ is even;} \\ (a_{f'} + 1)\mathcal{F}_n - f', & a_{f'} \text{ is odd,} \end{cases} \quad (5.13)$$

where $a_{f'}$ is the true alias number related to the aliased frequency f' .

As we observed in Figure 5.1, the folded phase line starts at the origin and continues folding downwards inside the Nyquist band up to some highest alias number. However, coherence phase estimates will typically be taken to be inside a given 360 degree phase band (*e.g.*, $[-180, 180)$ or $[-360, 0)$). Therefore, after completing the folding process in Figure 5.1(b), we transfer all the aliased pairs and the alias lines inside a phase band of 360 degrees (taken to be $[-360, 0)$ in this chapter). This is done by simply shifting each point on the folded phase line by a multiple of 360, until all the points appear inside the $[-360, 0)$ phase band.

In Figure 5.2(a), we denote the shifted aliased pairs by $p''_k = (f'_k, \varphi'(f_k))$, $k \in \{4, 5\}$. As we can see, the shifted aliased pairs, p''_k , are different from the aliased pairs $p'_k = (f'_k, \varphi(f_k))$, in their second component. Figure 5.2(a) shows the shifted aliased pairs as bullets and the unaliased P-F pairs on the phase line as circles. The positions of the P-F pairs p_1 , p'_2 , and p'_3 remain the same, since the phases of these pairs are

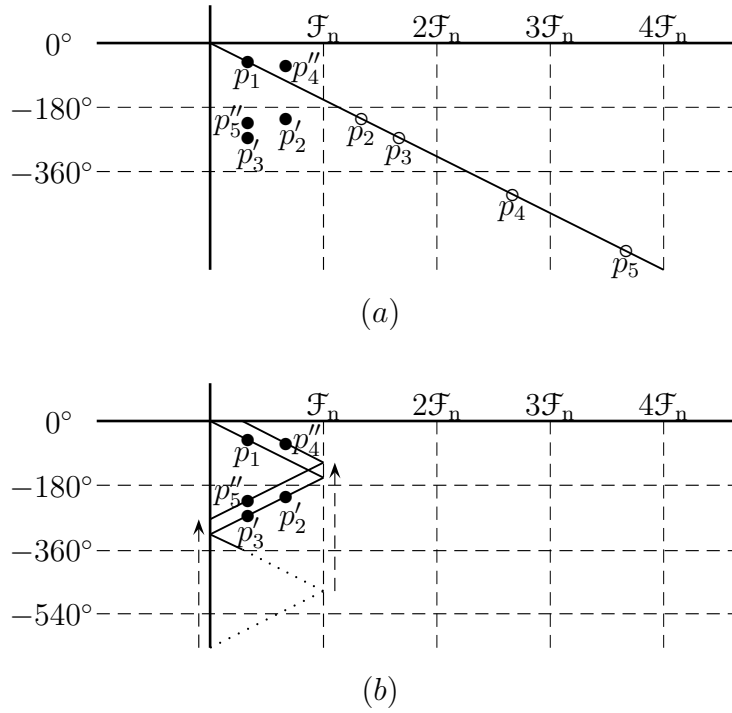


Figure 5.2: **Illustration of the shifting process of the phase line and aliased pairs into a 360 degree phase band.** The vertical axis is the phase axis (in degrees), and the horizontal axis is the frequency axis (in cycles/time unit). Figure 5.2(a) shows the aliased pairs (bullets) inside the $[-360, 0)$ phase band. The phase line and the unaliased P-F pairs p_1, p_2, p_3, p_4, p_5 are shown as circles. Note that the aliased and unaliased positions for p_1 are identical and is shown with bullet. Figure 5.2(b) shows the shifting process of the alias lines inside the $[-360, 0)$ phase band. The line containing the point p_1 is the *zeroth alias* (corresponding to $a = 0$). The line containing the points p_2 and p_3 is the *first alias line* (corresponding to $a = 1$). The line containing the point p_4 is the *second alias line* (corresponding to $a = 2$). Finally, the line containing the point p_5 is the *third alias line* (corresponding to $a = 3$). The dotted lines show the original position of the alias lines with phase values below -360 inside the Nyquist band.

themselves inside the $[-360, 0)$ phase band. We also apply the same shifting process to the alias lines, as illustrated in Figure 5.2(b). The dotted lines track the original position of the alias lines inside the Nyquist band. As we can see in Figure 5.2(b), the second alias line has broken into two parts in order to keep all the phase values inside the $[-360, 0)$ phase band.

5.2 Unaliasing Coherent Frequencies

It was mentioned in Section 5.1 that, in light of Eq. (5.11), knowledge of the time delay τ between \mathbf{X} and \mathbf{Y} determines the values of the (true) phase function at different unaliased frequencies. In practice, one has finite realizations of the two processes \mathbf{X} and \mathbf{Y} from which aliased frequencies are estimated. For a given estimated aliased frequency of interest, say \hat{f}' , the goal is to obtain the corresponding unaliased frequency estimate, say \hat{f} . To do so one can estimate the shifted coherence phase associated with \hat{f} , denoted by $\hat{\varphi}'$, using for example the multitaper coherence estimate given in Eq. (D.4) in the form of Eq. (5.1) or by using the phase estimate derived from the jackknifed multitaper coherence estimate given in Eq. (D.7), and so obtain the shifted aliased P-F pair estimate $(\hat{f}', \hat{\varphi}')$. Unfolding the aliased frequency estimate \hat{f}' then proceeds by placing the shifted aliased pair estimate $(\hat{f}', \hat{\varphi}')$ on the plot of the folded and shifted phase line (an example of which is given in Figure 5.2(b)) and seeing which alias line falls closest to the estimated P-F point. The alias number corresponding to this alias line is then an estimate of the alias number related to \hat{f}' , and the unaliased frequency estimate, \hat{f} , is then obtained via Eq. (5.13).

Unfortunately, in general coherence phase estimates have high variance (see [Jenkins and Watts 1968] or [Thomson and Chave 1991] for details) and in this case they are not accurate enough to reliably be used in our unfolding procedure. One exception is phase estimation at line component frequencies [Jenkins and Watts 1968] with

sufficiently large power compared with the power of the background stationary noise (also known as the *signal-to-noise ratio* or simply SNR). Fortunately, it is just such frequencies that are typically of interest in practice.

To estimate the coherence function $C_{\mathbf{X}\mathbf{Y}}$, we employ the multitaper coherence estimate $\widehat{C_{\mathbf{X}\mathbf{Y}}}$ from Eq. (D.4). Recall that \mathbf{X} and \mathbf{Y} follow the form shown in Eq. (5.2). For simplicity, assume that $\Delta T = 1$ so that $\mathcal{F}_n = 1/2$. Assume we have realizations of \mathbf{X} and \mathbf{Y} , respectively X_0, X_1, \dots, X_{N-1} and Y_0, Y_1, \dots, Y_{N-1} . Given these realizations, estimates of the spectra for \mathbf{X} and \mathbf{Y} and the cross-spectrum between \mathbf{X} and \mathbf{Y} at the frequency g_j of the j th line component can be obtained by first calculating the eigencoefficients (see Appendix B). The eigencoefficients of \mathbf{X} and \mathbf{Y} , denoted by $y_k(f; \mathbf{X})$ and $y_k(f; \mathbf{Y})$ respectively (see Appendix B, Eq. (B.7)), are

$$y_k(f; \mathbf{X}) = \sum_{j=1}^J \mu_j V_k(f - g_j) + \sum_{j=1}^J \bar{\mu}_j V_k(f + g_j) + \tilde{T}_k(f) + \tilde{v}_k(f), \quad \forall f \in \mathbb{R} \quad (5.14)$$

and

$$\begin{aligned} y_k(f; \mathbf{Y}) &= \sum_{j=1}^J \mu_j V_k(f - g_j) e^{i2\pi g_j \tau} + \sum_{j=1}^J \bar{\mu}_j V_k(f + g_j) e^{-i2\pi g_j \tau} \\ &\quad + \tilde{E}_k(f) + \tilde{G}_k(f). \end{aligned} \quad (5.15)$$

In the above $V_k(N, W; f) \equiv V_k(f)$ denotes the discrete Fourier transform of the

sequence $\nu_t^{(k)}(N, W)$ (see Appendix A, Eq. (A.15)) and

$$\begin{aligned}\tilde{T}_k(f) &\triangleq \sum_{t=0}^{N-1} \zeta(t) \nu_t^{(k)}(N, W) e^{-i2\pi f t}. \\ \tilde{\vartheta}_k(f) &\triangleq \sum_{t=0}^{N-1} \vartheta(t) \nu_t^{(k)}(N, W) e^{-i2\pi f t}. \\ \tilde{E}_k(f) &\triangleq \sum_{t=0}^{N-1} \varepsilon(t) \nu_t^{(k)}(N, W) e^{-i2\pi f t}. \\ \tilde{G}_k(f) &\triangleq \sum_{t=0}^{N-1} \vartheta(t + \tau) \nu_t^{(k)}(N, W) e^{-i2\pi f t}.\end{aligned}$$

Substituting the eigencoefficients of \mathbf{X} and \mathbf{Y} from Eqs. (5.14) and (5.15) into Eqs. (D.2) and (D.3) gives an estimate of the spectra for \mathbf{X} and \mathbf{Y} and the cross-spectrum between \mathbf{X} and \mathbf{Y} at frequency g_j of the j th line component. We have

$$\begin{aligned}\widehat{S}_{\mathbf{X}}(g_j) &= \frac{1}{K} \sum_{k=0}^{K-1} |\mu_j V_k(N, W; 0)|^2 \\ &+ \frac{1}{K} \sum_{k=0}^{K-1} 2\text{Re} \left\{ \tilde{T}_k(g_j) \overline{\tilde{\vartheta}_k(g_j)} \right\} \\ &+ \frac{1}{K} \sum_{k=0}^{K-1} 2\text{Re} \left\{ \mu_j V_k(N, W; 0) \left(\overline{\tilde{T}_k(g_j)} + \overline{\tilde{\vartheta}_k(g_j)} \right) \right\} \\ &+ \frac{1}{K} \sum_{k=0}^{K-1} |\tilde{T}_k(g_j)|^2 + \frac{1}{K} \sum_{k=0}^{K-1} |\tilde{\vartheta}_k(g_j)|^2 \\ &+ \mathbb{V}_{\mathbf{X}}(g_j),\end{aligned}\tag{5.16}$$

$$\begin{aligned}
\widehat{S}_{\mathbf{Y}}(g_j) &= \frac{1}{K} \sum_{k=0}^{K-1} |\mu_j V_k(N, W; 0)|^2 \\
&+ \frac{1}{K} \sum_{k=0}^{K-1} 2\text{Re} \left\{ \widetilde{E}_k(g_j) \overline{\widetilde{G}_k(g_j)} \right\} \\
&+ \frac{1}{K} \sum_{k=0}^{K-1} 2\text{Re} \left\{ \mu_j V_k(N, W; 0) e^{i2\pi g_j \tau} \left(\overline{\widetilde{E}_k(g_j)} + \overline{\widetilde{G}_k(g_j)} \right) \right\} \\
&+ \frac{1}{K} \sum_{k=0}^{K-1} |\widetilde{E}_k(g_j)|^2 + \frac{1}{K} \sum_{k=0}^{K-1} |\widetilde{G}_k(g_j)|^2 \\
&+ \mathbb{V}_{\mathbf{Y}}(g_j),
\end{aligned} \tag{5.17}$$

and

$$\begin{aligned}
\widehat{S}_{\mathbf{XY}}(g_j) &= \frac{1}{K} \sum_{k=0}^{K-1} |\mu_j V_k(N, W; 0)|^2 e^{-i2\pi g_j \tau} \\
&+ \frac{1}{K} \sum_{k=0}^{K-1} \mu_j V_k(N, W; 0) \left(\overline{\widetilde{E}_k(g_j)} + \overline{\widetilde{G}_k(g_j)} \right) \\
&+ \frac{1}{K} \sum_{k=0}^{K-1} \overline{\mu_j V_k(N, W; 0)} e^{-i2\pi g_j \tau} \left[\widetilde{T}_k(g_j) + \widetilde{\vartheta}_k(g_j) \right] \\
&+ \frac{1}{K} \sum_{k=0}^{K-1} \widetilde{T}_k(g_j) \left(\overline{\widetilde{E}_k(g_j)} + \overline{\widetilde{G}_k(g_j)} \right) + \frac{1}{K} \sum_{k=0}^{K-1} \widetilde{\vartheta}_k(g_j) \left(\overline{\widetilde{E}_k(g_j)} + \overline{\widetilde{G}_k(g_j)} \right) \\
&+ \mathbb{V}_{\mathbf{XY}}(g_j).
\end{aligned} \tag{5.18}$$

In the above, $\mathbb{V}_{\mathbf{X}}(g_j)$, $\mathbb{V}_{\mathbf{Y}}(g_j)$, and $\mathbb{V}_{\mathbf{XY}}(g_j)$ include any term containing $V_k(N, W; f)$ for $f \neq 0$. Eqs. (5.16), (5.17), and (5.18) can be represented in a condensed form as

$$\begin{aligned}
\widehat{S}_{\mathbf{X}}(g_j) &\approx \frac{1}{K} \sum_{k=0}^{K-1} |\mu_j V_k(N, W; 0)|^2 + N_{\mathbf{X}}(g_j), \\
\widehat{S}_{\mathbf{Y}}(g_j) &\approx \frac{1}{K} \sum_{k=0}^{K-1} |\mu_j V_k(N, W; 0)|^2 + N_{\mathbf{Y}}(g_j), \quad \text{and} \\
\widehat{S}_{\mathbf{XY}}(g_j) &\approx \frac{1}{K} \sum_{k=0}^{K-1} |\mu_j V_k(N, W; 0)|^2 e^{-i2\pi g_j \tau} + N_{\mathbf{XY}}(g_j),
\end{aligned}$$

where $N_{\mathbf{X}}(g_j) \in \mathbb{R}$, $N_{\mathbf{Y}}(g_j) \in \mathbb{R}$, and $N_{\mathbf{XY}}(g_j) \in \mathbb{C}$ denote the cross terms in Eqs. (5.16), (5.17), and (5.18) containing the stationary noise components from \mathbf{X} and \mathbf{Y} . The terms $\mathbb{V}_{\mathbf{X}}(g_j)$, $\mathbb{V}_{\mathbf{Y}}(g_j)$, and $\mathbb{V}_{\mathbf{XY}}(g_j)$ in Eqs. (5.16), (5.17), and (5.18) are assumed to be negligible for this approximation. This is a reasonable assumption since for each $k \in \{0, 1, \dots, K-1\}$, $V_k(N, W; f) \approx 0$ for all $|f| > W$, since $V_k(N, W; f)$ is highly concentrated in the interval $(-W, W)$. We also assume that all line components of \mathbf{X} and \mathbf{Y} are spaced at least W apart (this is because the ordinary multitaper estimate averages over $\pm W$ and so does not resolve closely-spaced lines; see [Thomson 1982] or [Percival and Walden 1993] for details).

The spectra and cross-spectrum estimates above can be used to estimate the MSC at frequency g_j , $\widehat{\gamma_{\mathbf{XY}}}(g_j)$. If the SNR at frequency g_j is large, the terms $N_{\mathbf{X}}(g_j)$, $N_{\mathbf{Y}}(g_j)$, and $N_{\mathbf{XY}}(g_j)$ will be small relative to the power at the line component. As a result, for large SNR at g_j , $\widehat{\gamma_{\mathbf{XY}}}(g_j)$ will be close to 1 and the phase of the coherence estimate (in radians) will be approximately $-2\pi g_j \tau$, shifted by a multiple of 2π to lie in the interval $[-2\pi, 0)$.

As a result of the above discussion, we only consider unaliasing frequencies corresponding to periodic components of the process \mathbf{X} (or \mathbf{Y}) with large SNR. In order to isolate frequencies with large SNR, we first apply the multitaper harmonic F -test (referred to here simply as the F -test) for periodicity (see Appendix C for details). The test is applied to detect a line component at a given frequency f under the null hypothesis H_0 : there are no line components in the spectrum of the process in a bandwidth of length $2W$ centered at f , where W is a small bandwidth parameter chosen for the multitaper estimation procedure (typically, W is chosen so that the time-bandwidth product $2NW$ is between 4 and 10, see [Thomson 1982] for details). We apply the F -test to the realizations of both \mathbf{X} and \mathbf{Y} to limit the set of frequencies under consideration by requiring that both the F -tests for realizations of \mathbf{X} and \mathbf{Y} are moderately significant. The threshold for this test represents the usual compromise

between false detects and misses, and we have used the 95% level.

Next, we examine the coherence estimate and search for the significant frequencies from the F -tests which also have significant MSC. Since in this thesis, our focus is on line components with large MSC (close to 1), we keep only those significant frequencies from the F -tests for which the estimated MSC is larger than 0.9. This is an *ad hoc* choice but note that it corresponds to a very high significance level in a multitaper statistical test described in [Thomson 2007] to detect significant coherent frequencies under the null hypothesis $H_0: \gamma(f) = 0$, under which a frequency f is significant at level c if the estimated MSC at f is larger than $1 - (1 - c)^{1/(K-1)}$, where K is the number of data tapers. With $K = 7$ tapers, which is what we used, an estimated MSC greater than 0.9 corresponds to a significance level of $c = 0.999999$. Our final set of frequencies, those we consider to be strong candidates for frequencies of line components, with large SNR, are those which are significant under the F -tests in both \mathbf{X} and \mathbf{Y} , as described above, and also significant at the 99.9999% significance level under the test for coherency. Our shifted aliased P-F pairs then are made up of these significant frequencies together with the corresponding jackknifed phase estimates from Eq. (D.7).

Some practical issues which arise in the unaliasing process are now addressed. From the sample eigencoefficients in Eq. (B.7), one can see that the spectrum estimate in Eq. (B.9) is an even function of frequency and is periodic with period $2\mathcal{F}_n$. Similarly, the complex coherence estimator in Eq. (D.4) is periodic with period $2\mathcal{F}_n$ and, for real-valued data, its magnitude is an even function while its phase is an odd function.

This creates an ambiguity, a “further aliasing”, between frequencies $+f$ and $-f$, $f \in [-\mathcal{F}_n, \mathcal{F}_n)$, for real-valued data. Suppose we are trying to detect a line component with true frequency, say g , and g lies on an odd alias line. Then, assuming the SNR is large at this line component, based on the F -tests and the MSC, we will detect it close to the aliased frequency g' , where we take $g' \in [0, \mathcal{F}_n)$. However, for odd aliases

g actually gets aliased to $-g'$ in the coherence estimate and the phase estimate we are after is the phase of $\widehat{C_{\mathbf{X}\mathbf{Y}}}(-g')$. Unfortunately, we have no way of knowing whether the line component has aliased frequency g' or $-g'$ since we do not *a priori* know the alias number of the line component frequency. The simplest way to resolve this ambiguity is to associate two phase estimates with each detected aliased frequency under consideration. If g' denotes the detected aliased frequency, then one phase estimate is the phase of $\widehat{C_{\mathbf{X}\mathbf{Y}}}(g')$, where we take this phase to be in the interval $[-360, 0)$, in degrees. The second phase estimate is the phase of $\widehat{C_{\mathbf{X}\mathbf{Y}}}(-g')$, again taken to be in $[-360, 0)$; that is, we take the negative of the first phase estimate and subtract 360. (We actually use the jackknifed versions of these phase estimates, see Eq. (D.7)). In the unaliasing procedure, we compare both phase estimates to the folded and shifted alias lines. The “correct” phase is the one which provides a better fit to an alias line.

The unaliasing procedure now is simply to choose the alias line that minimizes the phase error. To do this, one chooses a maximum alias number, for example on a physical basis. For the given time delay τ , draw the folded and shifted alias lines, as in Figure 5.2(b), up to the maximum. The two phase estimates for a given detected aliased frequency g' are placed on the plot. The closest (in phase error) alias line to the first phase estimate and the closest alias line to the second phase estimate are determined. The alias line with the smaller phase error is the best fit. Ideally, the phase error from the best fitting alias line should be within one standard deviation of the phase estimate, where we use the jackknifed standard deviation of the phase estimate. In cases of near ties, our bias is to choose the lower frequency, but a considered decision should be informed by the properties of the physical process generating the data. If no alias lines give a “good” fit (within two standard deviations) to either of the phase estimates, we may declare the unfolding procedure to have failed or consider increasing the maximum number of alias lines. Whether or not this is a

good idea is again application dependent.

In addition, one should bear in mind that the folded and shifted alias lines will eventually start to “lie on top of one another” (since the time delay will be a rational number in practice.) If A is the smallest natural number such that φ_{2A} is a multiple of 360, then the maximum number of distinct alias lines that will appear inside the $[-360, 0)$ phase band is $2A$. The alias lines will then start to fold exactly “on top of” the first $2A$ alias lines inside the $[-360, 0)$ phase band. Even before this occurs, however, we do not recommend letting the folded and shifted alias lines fall “nearly” on top of one another, say within two jackknife standard deviations apart.

Remark 5.2.1 *Following Remark 5.1.1, when the time delay is $\Delta T - \tau$ instead of τ , the coherence estimate will vary with the phase line and the final result for the unaliased frequencies remains unchanged.*

Remark 5.2.2 *Recall that the technique described in Section 5.1 is applicable when the two processes \mathbf{X} and \mathbf{Y} satisfy the linear relationship of Eq. (5.2). We note that the same technique could be extended to a single process \mathbf{X} , say, by subsampling \mathbf{X} to create $n \geq 2$ processes $\mathbf{Y}^{(a)}$, $1 \leq a \leq n$. This can be accomplished in the following way: fix a new sampling interval $\Delta T' = n\Delta T$ where $n \in \mathbb{N}$, and set $\mathbf{Y}^{(a)} = \{X(t\Delta T' + (a-1)\Delta T)\}_{t \in \mathbb{Z}}$, $1 \leq a \leq n$. In this case, the coherence analysis can be applied to any two of $\mathbf{Y}^{(j)}$ and $\mathbf{Y}^{(k)}$, where $1 \leq j < k \leq n$ and $\tau = (k-j)\Delta T$. The final result can be based on averaging the P-F pairs resulting from the coherence analysis of every pair $(\mathbf{Y}^{(j)}, \mathbf{Y}^{(k)})$, $j < k$, with equal time delays. The unfolding process of the phase line can be then applied to the averaged P-F pairs, and the phase at the Nyquist frequency can be calculated using Eq. (5.12). We note that this subsampling approach is limited by the maximum number of unique folded and shifted alias lines one can distinguish. This number is $2A$, where A is the smallest natural number such that $(k-j)A/n$ is a natural number. Thus, in the best case we could not distinguish more than the first $2n$ alias lines. At the same time the Nyquist frequency has been*

reduced by a factor of $1/n$. Therefore, using this approach we cannot hope to detect line components whose true frequencies are greater than twice the original Nyquist frequency. Nonetheless, in some cases this technique may prove useful.

Remark 5.2.3 Let \mathbf{X} be a continuous-time process which follows the form shown in Eq. (5.2), where $\{\zeta(t)\}_{t \in \mathbb{R}}$, $\{\varepsilon(t)\}_{t \in \mathbb{R}}$, and $\{\vartheta(t)\}_{t \in \mathbb{R}}$ are three independent continuous-time real-valued zero-mean nonstationary noise processes. Supposing we have a realization of \mathbf{X} , we have observed in simulations that if the SNR is large at frequency g_j (the frequency of the j th line component), the method proposed in this chapter to unalias the aliased harmonic frequencies is still applicable. It is indeed possible to show that if \mathbf{X} follows the continuous-time equivalent of the representation shown in Eq. (3.12), we can proceed with a similar analysis as in Section 5.1, coherency can be calculated as a complex-valued function of both time and frequency (where the phase function remains linear as in Eq. (5.10)), but the amplitude function becomes time-dependent.

5.3 Examples

In this section we provide two examples. The first, in Section 5.3.1, uses simulated data to illustrate the unfolding process. In the second example, in Section 5.3.2, we examine seventeen years of daily solar radio noon flux data compiled by the NGDC. The analysis of this data was the motivation for the methods developed in this chapter.

5.3.1 Simulated Data Example

Consider $\mathbf{X} \triangleq \{X_t\}_{t \in \mathbb{Z}}$ and $\mathbf{Y} \triangleq \{Y_t\}_{t \in \mathbb{Z}}$ with the representations of the form shown in Eq. (5.2) with $\Delta T = 1$ day. We assume that $\vartheta(t) \equiv 0$ so that the random components of \mathbf{X} and \mathbf{Y} are independent. Further, for $j \in \{1, 2, \dots, 8\}$, we assume that $\theta_j = 0$

and $D_j = 10$, so that

$$X_t = \sum_{j=1}^8 10 \cos(2\pi g_j t) + \zeta_t, \quad \forall t \in \mathbb{Z},$$

where $\{\zeta_t\}_{t \in \mathbb{Z}}$ is a zero-mean unit-variance white noise process and the frequencies $\{g_1, \dots, g_8\}$, in units of μHz , are shown in the first column of Table 5.1. We assume that the time delay is $\tau = 0.22$ days. Following Eq. (5.2), the process \mathbf{Y} can be represented by

$$Y_t = \sum_{j=1}^8 10 \cos(2\pi g_j(t + 0.22)) + \varepsilon_t, \quad \forall t \in \mathbb{Z},$$

where $\{\varepsilon_t\}_{t \in \mathbb{Z}}$ is a zero-mean unit-variance white noise process independent of $\{\zeta_t\}_{t \in \mathbb{Z}}$.

Recall from Section 5.1 that by knowing the Nyquist frequency ($\mathcal{F}_n = 5.787 \mu\text{Hz}$, in this example), the translated Nyquist band related to each unaliased frequency is $[a\mathcal{F}_n, (a+1)\mathcal{F}_n)$, where a is the appropriate alias number. Using the unaliased frequencies from Table 5.1, the alias numbers were computed. Using Eq. (5.13), the true aliased frequencies were calculated. The aliased frequencies are reported in the third column of Table 5.1. The phase of the complex coherency between the two processes \mathbf{X} and \mathbf{Y} follows a linear form as in Eq. (5.11). Using the unaliased frequencies from Table 5.1 and the time delay $\tau = 0.22$ days, and making necessary unit changes, the true phase in degrees was calculated. The true coherence phase values are reported in the fourth column of Table 5.1.

In order to apply the technique explained in Section 5.2 using the estimation methods, we first consider finite realizations of the two processes \mathbf{X} and \mathbf{Y} at N time points as X_0, \dots, X_{N-1} and Y_0, \dots, Y_{N-1} for $N = 4000$. We apply the F -test (see Appendix C) to these realizations at the 95% significance level. The results of the F -tests confirm the appearance of large F -values (essentially at 100% significance) at the aliased frequencies calculated and reported in Table 5.1. At the significant

TUF(μ Hz)	AN	TAF(μ Hz)	TCP(deg.)
0.3490	0	0.3490	-2.3881
9.0197	1	2.5544	-61.721
13.8813	2	2.3072	-94.988
20.7646	3	2.3835	-142.089
26.2988	4	3.1507	-179.959
30.5430	5	4.1792	-209.002
79.2468	13	1.7717	-542.276
105.7646	18	1.5979	-723.734

Table 5.1: **True aliased frequencies and true phase calculation of complex coherency.** TUF is the true unaliased frequency (in μ Hz) chosen for the simulated example. AN is the alias number a related to each unaliased frequency associated with its translated Nyquist band $[a\mathcal{F}_n, (a+1)\mathcal{F}_n)$ for $\mathcal{F}_n = 5.787 \mu$ Hz. TAF is the true aliased frequency calculated using Eq. (5.13). TCP is the true coherence phase found using the unalised frequencies and the linear phase representation in Eq. (5.11).

frequencies we then apply the multitaper coherence test between the above data sets at the 99.9999% significance level. The line components have very large MSC values (close to 1) in the coherence test. For each of the detected aliased coherent frequencies we compute the two phase estimates and apply the unaliasing procedure as described in Section 5.2.

Table 5.2 shows the results of the unaliasing technique for the aliased frequencies appearing in the third column of Table 5.1. The highest alias number has been chosen to be 20 and the results in Table 5.2 are the averages from 100 repetitions. The second column of Table 5.2 shows the estimated phase for the aliased frequencies from the coherence test. This phase is the one which gives the minimum error in the alias detection. This error is shown in the third column of Table 5.2. As we can see, this error is smaller than $\sigma_{\hat{\varphi}}$, where $\sigma_{\hat{\varphi}}$ is the jackknifed estimate of the standard deviation of the phase estimate (JESDPE) from Eq. (D.8). The alias number related to each aliased frequency giving the minimum error from the phase estimate is shown in the fifth column of Table 5.2. Using the estimated aliased frequencies and their related estimated alias number results in the estimate of the unaliased frequencies following

EAF (μHz)	ECP (deg.)	MEE (deg.)	JESDPE (deg.)	EAN	EUf (μHz)
0.3490	-2.4168 (0.211)	0.1678 (0.131)	0.2094 (0.107)	0	0.3490 (3.35E-16)
2.5544	-61.6982 (0.199)	0.1576 (0.123)	0.2130 (0.101)	1	9.0196 (1.25E-14)
2.3072	-94.9321 (0.188)	0.1575 (0.116)	0.2056 (0.096)	2	13.8813 (1.96E-14)
2.3835	-142.608 (0.222)	0.1769 (0.136)	0.2154 (0.115)	3	20.7646 (2.50E-14)
3.1507	-179.8253 (0.123)	0.1378 (0.119)	0.2034 (0.096)	4	26.2988 (2.50E-14)
4.1792	-208.9706 (0.179)	0.1435 (0.111)	0.2098 (0.101)	5	30.5430 (2.50E-14)
1.7717	-542.2722 (0.199)	0.1583 (0.121)	0.2036 (0.101)	13	79.2468 (1.14E-13)
1.5979	-723.7274 (0.183)	0.1490 (0.105)	0.2030 (0.101)	18	105.7646 (9.99E-13)

Table 5.2: **Estimated unaliased frequencies for the simulated data.** EAF are the estimated aliased frequencies in μHz with MSC close to 1 which are exactly the aliased frequencies of interest shown in Table 5.1. ECP is the estimated coherence phase in degrees which gives the minimum error (in degrees) when determining the best fitting alias line for each estimated aliased frequency, as described in Section 5.2. The minimum error estimate is reported in column MEE. JESDPE in degrees is the jackknifed estimate of standard deviation of the phase estimate, $\sigma_{\hat{\varphi}}$, at each estimated aliased frequency. As we can see, the MEE at each estimated aliased frequency is smaller than $\sigma_{\hat{\varphi}}$. EAN is the estimated alias number for each estimated aliased frequency related to the coherence phase estimate. EUf is the estimated unaliased frequency in μHz , which is calculated using Eq. (5.13) when the estimated aliased frequency and the estimated alias number are available. All the estimated values are the average of 100 replications, and the values in parentheses are the standard deviations of the estimates over the 100 replications.

Eq. (5.13), and given in the sixth column of Table 5.2. We did not report the MSCs in Table 5.2 only because they were all very close to 1. Note that in this example, a very high signal-to-noise ratio of 50 dB has been used and so the detection and estimation are essentially exact.

5.3.2 Solar Noon Flux Data

The particular real-world example we consider here is seventeen years of daily solar radio noon flux data (1989–2006), collected by the U.S. Air Force and distributed by the NGDC of the National Oceanic and Atmospheric Administration (NOAA), publically available via FTP¹. These data were collected in four different observation stations at Learmonth (Australia), Palehua (Hawaii), Sagamore Hill (Massachusetts, U.S.A.) and San Vito (Italy). The noon flux data were measured at eight fixed frequencies: 245 MHz, 410 MHz, 606 MHz, 1415 MHz, 2695 MHz, 4995 MHz, 8800 MHz and 15400 MHz. For our analysis, we have chosen the series corresponding to the 2695 MHz frequency, since this frequency is simply the median of the above frequencies. Missing data points in this series were filled by a simple linear interpolator. The interpolated series was then iteratively run through a Wiener interpolator (see [Wiener 1949] for detail) until all the linearly-interpolated values were unchanged within a small prescribed tolerance.

To create a P-F plot, we apply our procedure to data sets collected at a pair of observation stations which are almost on opposite sides of the Earth longitudinally. The two stations in such a pair observe the same solar process but with an approximately 12-hour time offset. The additive stationary noise processes in Eq. (5.2) can be regarded as the noise generated by the process of measurement and various types of solar surface noise [Harvey et al. 1996].

As mentioned above, the main interest in this chapter is to detect the signal's

¹ftp://ftp.ngdc.noaa.gov/stp/solar_data/solar_radio/flux/usaf_noon_flux

periodic components. We apply the F -test at the 95% significance level to the solar noon flux data set for each observation station in a pair of stations and isolate those frequencies which are significant at both stations and also give an estimated MSC greater than 0.9. This gives us our set of estimated aliased frequencies of suspected line components.

As explained in Section 5.1, the time delay between each antipodal pair of observation stations can be used to create the phase line. This is accomplished by computing the phase in degrees at nonnegative integer multiples of the Nyquist frequency. The phase line folds inside the Nyquist band, creating different alias lines as explained in Section 5.1. Figure 5.3 shows an example of the P-F plot for the jackknifed multi-taper coherence phase estimates between the two observatory stations at Learmonth and Sagamore Hill, including the folded phase line inside the Nyquist band, for the highest alias number $A = 4$. The time offset between Learmonth and Sagamore Hill is 12.34 hours. Note that in this example the frequency unit is μHz . For the given daily data ($\Delta T = 1$ day) the Nyquist frequency $\mathcal{F}_n = 5.787 \mu\text{Hz}$, and we can use Eq. (5.12) to determine φ_j , at the frequencies $j\mathcal{F}_n$, where $j \in \{1, 2, 3, 4\}$. As is evident from Figure 5.3, the MSC is largest around the solar rotation frequency of approximately $0.4 \mu\text{Hz}$ and decreases (below 0.9) at higher frequencies. This is possibly a result of three factors. The first factor is that spectra of solar signals usually decrease above the solar rotation frequency. The second factor is that errors in measurement will be largest at periods of a few days because of the duration of weather patterns at each observatory station. The last factor is that the solar radio noon flux data has numerous missing values and interpolation errors tend to mask high frequencies.

In Section 5.2, we mentioned that the highest alias number one might use in the unaliasing process could be limited depending on the physical application. In the present example, there are two reasons for limiting the highest alias number: first, the stations, *i.e.*, Learmonth and Sagamore, are approximately 12 hours apart, so that

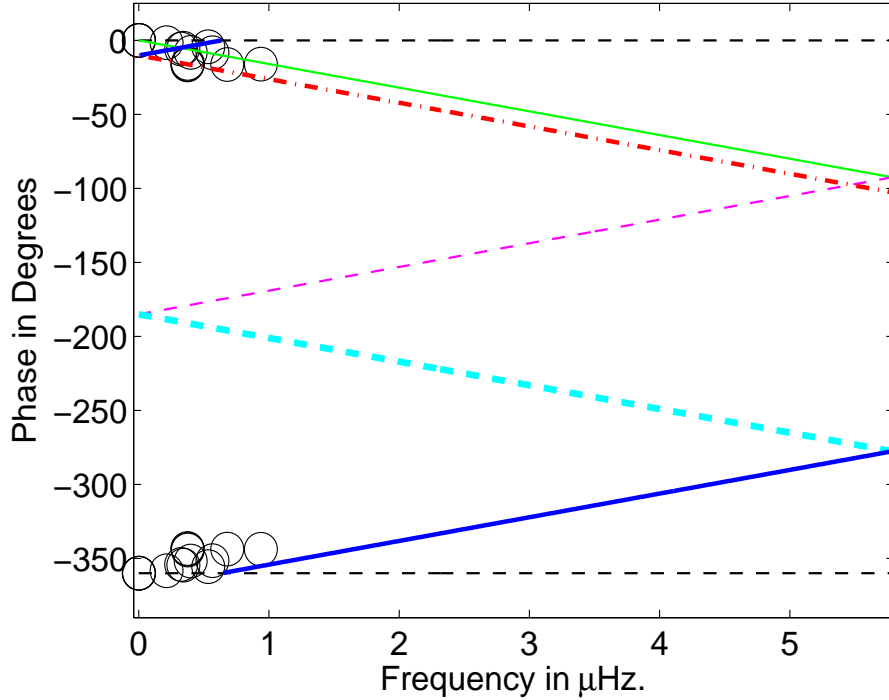


Figure 5.3: **Phase-frequency plot and folding of the phase line for the solar noon flux data from Learmonth and Sagamore Hill stations.** The time offset between the two stations is 12.34 hours and the Nyquist frequency is $\mathcal{F}_n = 5.787 \mu\text{Hz}$. The P-F pairs in this plot are at frequencies for which the F -test results for both data sets are significant at the 95% significance level, and at which the estimated MSC is larger than 0.9. In this plot, the P-F pairs and the alias lines are shown clearly in the $(-360, 0)$ phase band. The highest alias number used here is $A = 4$. The thin-solid line (green) shows the zeroth alias ($a = 0$), the thin-dashed line (magenta) shows the first alias ($a = 1$), the thick-dashed line (cyan) shows the second alias ($a = 2$), the thick-solid line (blue) shows the third alias ($a = 3$), and the thick-dotted-dashed line (red) shows the fourth alias ($a = 4$). As we can see, part of the third alias, and all of the fourth alias, which have phase values below -360 degrees have shifted up by 360 degrees. Note that in this plot every frequency is given two phases for reasons discussed in Section 5.2.

high aliases are nearly indistinguishable; second, the timing of the measurements usually varies about noon by a few minutes (K. F. Tapping, personal communication, December 1, 2006). This introduces a frequency-dependent phase variance that reduces the likelihood of high aliases. Taking into account the above problems, we limit the highest alias number to $A = 12$. We then apply the unfolding procedure described in Section 5.2. Table 5.3 reports all the aliased frequencies shown in Figure 5.3 with the best alias numbers and the estimated unaliased frequencies.

We now consider a few of the aliased frequencies in Table 5.3 in more detail. We first look at a few frequencies which, according to our analysis, are not aliased (*i.e.*, their alias number is zero) and are known to exist as low-frequency modes in the sun. The frequency $0.0014 \mu\text{Hz}$, with a period of 22.96 years, represents the known Hale cycle period [Hale 1924]. The frequency $0.0007 \mu\text{Hz}$, with a period of 45.92 years, on the other hand, is approximately the first sub-harmonic of the Hale-cycle also known as the Suess cycle. The frequency $0.3991 \mu\text{Hz}$, with a period of 29 days, is very close to the solar rotation period of 27.3 days [Wolff and Hickey 1987]. The frequency $0.214 \mu\text{Hz}$ with a period of 54 days, is the first sub-harmonic of the solar rotation frequency.

The second case we look at is when a frequency is aliased according to our analysis, but has been reported as a low-frequency mode in the literature. The period 33.6 days (frequency $0.344 \mu\text{Hz}$) was reported in [Pap et al. 1990] from an analysis of daily data of projected areas of passive spots, recorded from 1980–1988. In our result, the frequency $0.3423 \mu\text{Hz}$ (which is within one Rayleigh resolution of $0.344 \mu\text{Hz}$) may be affected by aliasing. As can be seen in Table 5.3, for errors smaller than the JESDPE, there are two alias possibilities for $0.3423 \mu\text{Hz}$. Alias zero has the smallest error, which supports the reported frequency in [Pap et al. 1990], but the error related to alias three is also much smaller than the JESDPE and might be the correct alias number. If alias three is accepted, the unaliased frequency is $22.8059 \mu\text{Hz}$ (period 12.8 hours). Similarly, $0.378 \mu\text{Hz}$ was reported in [Wolff and Hickey 1987] from a

EAF (μHz)	EMSC	ECP (deg.)	JESDPE (deg.)	EE (deg.)	EAN	EUF (μHz)	EPR (h,d,y)
0.0007	0.9977	-0.0064	0.1712	0.0049	0	0.0007	45.3y
0.0014	0.9983	-0.0141	0.2934	0.0085	0	0.0014	22.6y
0.0018	0.9985	-0.0183	0.3306	0.01	0	0.0018	17.6y
0.214	0.9004	1.5830	4.7983	1.8402	0	0.214	54.08d
0.3260	0.9247	-5.9177	6.709	0.9315	3	22.8221	12.7h
0.3423	0.9001	-5.4216	4.5883	0.0520	(0)	0.3423	33.81d
0.3423	0.9001	-5.4216	4.5883	0.6953	3	22.8059	12.8h
0.3730	0.9530	-16.6614	2.8596	0.4963	(4)	23.5211	11.95h
0.3730	0.9530	-16.6614	2.8596	2.2265	7	45.9233	6.05h
0.3744	0.9452	-16.2436	3.9338	0.2386	4	23.5226	11.8h
0.3758	0.9356	-15.5959	3.4046	0.6144	(4)	23.5239	11.81h
0.3758	0.9356	-15.5959	3.4046	1.2063	7	45.9202	6.05h
0.3991	0.9913	-8.1618	1.7787	1.2754	0	0.3991	29d
0.5341	0.9666	-4.3891	3.2108	2.7301	3	22.6141	12.28h
0.5662	0.9019	-8.4194	4.9549	0.6356	(0)	0.5662	20.44d
0.5662	0.9019	-8.4194	4.9549	2.9255	7	45.7301	6.07h
0.6789	0.9109	-16.3190	5.8533	5.4620	0	0.6789	17.05d
0.6789	0.9109	-16.3190	5.8533	4.7380	4	23.8270	11.66h
0.6789	0.9109	-16.3190	5.8533	3.4240	(11)	68.7656	4.04h
0.9374	0.9068	-16.1268	6.3770	1.1349	0	0.9374	12.35d
0.9374	0.9068	-16.1268	6.3770	0.5187	(11)	68.5070	4.05h

Table 5.3: **Estimated unaliased frequencies for the real-world example.** EAF is the estimated aliased frequency in μHz appearing in both the F -test result (exceeding the 95% significance level) and coherence result (with MSC larger than 0.9). EMSC is the estimated MSC. ECP is the jackknife coherence phase estimate (degrees). JESDPE is the jackknifed estimate of standard deviation of the phase estimate (degrees). EE is the estimated error (degrees) and represents the distance between the estimated phase and the true phase, using different alias lines; these errors were only accepted if smaller than the JESDPE. EAN is the estimated alias number for EAF whose EE is smaller than the JESDPE. If there is more than one EE, there is one EAN for each EE. We have shown the EAN for the smallest EE in parentheses. EUF is the estimated unaliased frequency (μHz), calculated using the EAF and related EAN in Eq. (5.13). EPR is the estimated period in years (y), days (d), or hours (h) for each EUF.

theoretical analysis as a low-frequency mode. In our analysis, $0.3758 \mu\text{Hz}$ (which is within one Rayleigh resolution of $0.378 \mu\text{Hz}$) is more likely affected by aliasing. Alias four and alias seven are the possibilities, as can be seen in Table 5.3. Alias four has the least error, and the related unaliased frequency is $23.5239 \mu\text{Hz}$ (period 11.8 hours).

For the third case, we consider frequencies which are aliased according to our analysis, and the corresponding unaliased frequency has been reported in the literature. The aliased frequencies $0.6789 \mu\text{Hz}$ and $0.9374 \mu\text{Hz}$ unalias to $68.7656 \mu\text{Hz}$ and $68.5070 \mu\text{Hz}$, respectively, when the minimum-error technique is used. These two unaliased frequencies fall in a frequency band expected to be dense with g -modes² (Henning and Scherrer [1988] report a frequency of $68 \mu\text{Hz}$ for the $l = 1$, $m = 1$, and $n = -9$ mode). We note that the preferred frequencies in the last two groups, $68.7656 \mu\text{Hz}$ and $68.5070 \mu\text{Hz}$, differ by 258.6 nHz , approximately the splitting expected between adjacent singlets of an $l = 1$ g -mode [Henning and Scherrer 1988]; if they are indeed from the same mode, that would imply an effective rotation rate of 517 nHz . The data set used for the analysis in [Henning and Scherrer 1988] is the Stanford observatory data from summer 1987, sampled every minute.

5.4 Conclusion

In this chapter, we presented a frequency-domain technique to detect aliased harmonic frequencies in the spectral analysis of time series. The technique is based on the coherence estimate between a process containing line components and stationary noise, and a time-delayed version of itself perturbed by stationary noise. The phase of the coherence estimate departs from the linear trend expected from the time delay between the two processes. We proposed that the nonlinearity of the coherence phase

²*g-modes* or *internal gravity modes* are a set of hydrodynamic modes in the sun caused by a density inversion near the top of the solar core, so their restoring force is buoyancy.

estimate can be explained as being the coherence phase for unaliased frequencies and not the aliased ones. We then used the information of the time delay and the coherence phase estimates to identify unaliased frequencies.

To illustrate the technique, we applied it to two examples, one using simulated data with very high SNR to illustrate the mechanics of the method and the other involving real-world data. For the latter example, we considered seventeen years of solar radio noon flux data, collected by the U.S. Air Force at four terrestrial observation stations during the years 1989–2006, and distributed by the NGDC. The jackknifed multitaper coherence estimates were computed for a pair of observation stations having an approximately 12-hour longitudinal time difference.

Chapter 6

Conclusion and Future Work

6.1 Conclusion

In this thesis, we introduced a new estimator of the Wold-Cramér evolutionary spectrum called the BCMTFSE. The BCMTFSE has improved boundary behaviour in the time-frequency plane compared with other commonly used estimators of Wold-Cramér evolutionary spectra. The performance of this estimator was demonstrated by applying it to several simulated nonstationary processes. We used the BCMTFSE to introduce a heuristic graphical technique to help one draw conclusions about the class that a particular process belongs to. Under the assumption that the process under study is a uniformly modulated process, we introduced the ITFSE to estimate its Wold-Cramér evolutionary spectrum. The ITFSE shows improved frequency resolution compared to the BCMTFSE. The performances of the graphical technique and the ITFSE were demonstrated by applying them to several simulated nonstationary processes.

We also introduced a graphical technique to detect and unalias aliased harmonic frequencies. The performance of this technique was demonstrated by applying it to a simulated process, and also by applying it to a real-world example (17 years of solar

daily noon flux data). For the solar data, we identified harmonic frequencies that are commonly reported in the literature and may be aliases of higher frequency modes.

6.2 Future Work

In this section, we describe future research endeavours related to the work presented in this thesis.

6.2.1 Methodology

- Forecasting of nonstationary processes using linear models such as ARMA model can be performed using the relationship between the ARMA coefficients and cepstrum coefficients [Schroeder 1981]. The cepstrum coefficients can be estimated via an estimate of the Wold-Cramér evolutionary spectrum. The BCMTFSE or ITFSE, therefore, can be used to forecast nonstationary processes.
- The main obstacle to deriving a formal statistical test to determine whether or not a given process is a UMP was the lack of knowledge about the distribution of the BCMTFSE and in particular, of the largest singular values of the matrix $\widehat{S}_{\mathbf{X}}$. It may be possible to determine (or approximate) the distributions of the BCMTFSE and of the singular values of the matrix $\widehat{S}_{\mathbf{X}}$. This knowledge could then be used to remove heuristics from the procedure described in Section 4.2.
- In order to define the BCMTFSE, we extrapolated the MTFSE near the time boundaries of the time-frequency plane. This was accomplished by estimating the time-derivative of the Wold-Cramér evolutionary spectrum. Analogously, estimating the second time-derivative of the Wold-Cramér evolutionary spectrum, when applicable, can be used for (possibly more accurate) locally quadratic extrapolations.

- Wold-Cramér evolutionary spectra are only defined for processes which do not contain any purely harmonic frequencies. For practical applications, this assumption is quite restrictive. If harmonic components are present, one must detect and remove them, and possibly unalias them. We proposed a graphical technique in Chapter 5 to unalias harmonic components, assuming stationary background noise. This procedure can be extended to unalias harmonic components in nonstationary background noise, via an extension of the BCMTFSE to estimate Wold-Cramér evolutionary cross spectra and coherences between two nonstationary processes.
- The graphical technique proposed in Chapter 5 used a minimum-error approach to selecting the “best” alias number fit to each aliased frequency. It may be possible to select the best fit in a more judicious way if the distribution of the phase of the coherence function is known.

6.2.2 Data Analysis: Simulated and Real-World Data

- Apply the BCMTFSE and/or ITFSE to real-world data, particularly seismic data; indeed, UMPs have been used successfully as models for seismic phenomena, as mentioned in Chapter 4.
- Apply the unaliasing method from Chapter 5 to the solar noon flux data between two stations with a time difference of less than 12 hours, and also between two stations with different measurement frequencies, as part of a more comprehensive analysis of this data set.
- For other helioseismology data, determine delay times between different carrier frequencies, and use this information to determine the propagation time in the solar atmosphere.

- Use a more rapidly-sampled solar flux data set, and compare the harmonic frequencies detected in the more rapidly-sampled data with the unaliased frequencies from the more slowly-sampled data.

Bibliography

- P. T. Brockwell and R. A. Davis. *Time Series: Theory and Methods*. Springer-Verlag, New York, 1987.
- E. C. Catmull. A hidden-surface algorithm with anti-aliasing. *Computer Graphics*, 12(3):6–11, 1978.
- L. Cohen. *Time-Frequency Analysis*. Prentice-Hall PTR, Upper Saddle River, New Jersey, 1995.
- L. Cohen. Generalized phase-space distribution functions. *Journal of Mathematical Physics*, 7(5):781–786, 1966.
- L. Cohen and T. E. Posch. Positive time-frequency distribution functions. *IEEE Transactions on Acoustics, Speech, and Signal Processing*, 33(1):31–38, 1985.
- J. G. Cragg and G. Donald. Inferring the rank of a matrix. *Journal of Econometrics*, 76:223–250, 1997.
- H. Cramér. *Mathematical Methods of Statistics*. Princeton University Press, Princeton, New Jersey, 1946.
- H. Cramér. On some classes of non-stationary processes. *Proceedings of the Fourth Berkeley Symposium on Mathematical Statistics and Probability*, 2:57–78, 1961.
- F. C. Crow. The aliasing problem in computer-generated shaded images. *Communications of the ACM*, 20(11):799–805, 1977.

- F. C. Crow. A comparison of antialiasing techniques. *Computer Graphics and Applications, IEEE*, 1(1):40–48, 1981.
- G. R. Dargahi-Noubary. On seismic classification using non-stationary models and a definition of complexity. Technical Report 96, Department of Mathematics, UMIST, 1978a.
- G. R. Dargahi-Noubary. A note on non-stationary model for seismic p -waves. Technical Report 97, Department of Mathematics, UMIST, 1978b.
- G. R. Dargahi-Noubary and P. J. Laycock. Special ratio discriminant and information theory. *Journal of Time Series Analysis*, 2(2):71–85, 1981.
- C. S. Detka, A. El-Jaroudi, and L. F. Chaparro. Relating the bilinear distributions and the evolutionary spectrum. *International Conference on Acoustics, Speech, and Signal Processing*, 4:496–499, 1993.
- J. Durbin. The fitting of time-series models. *Revue Inst. Inter. de Stat.*, 28:233–244, 1960.
- B. Efron. *The Jackknife, the Bootstrap, and other Resampling Plans*. SIAM, Philadelphia, 1982.
- M. M. Farhad and S. Mirzakuchaki. A gm-c anti-aliasing filter for digital radio receivers. *International Conference on Acoustics, Speech, and Signal Processing*, 1 – 5, 2008.
- P. Flandrin. *Time-Frequency/Time Scale Analysis*. Academic Press, New York, 1999.
- T. Fujita and H. Shibara. On a model of earthquake ground motions for response analysis and some examples of analysis through experiment. *Conference on Engineering Design for Earthquake Environments*, 12:139–148, 1978.

- D. Gabor. Theory of communications. *Journal of the IEE*, 93:429–457, 1946.
- G. H. Golub and C. F. Van Loan. *Matrix Computations*. The Johns Hopkins University Press, Baltimore, MD, 1983.
- U. Grenander and G. Szegö. *Toeplitz Forms and their Applications*. Chelsea Publishing, New York, 1955.
- G. E. Hale. The law of sun-spot polarity. *Proc. Natl. Acad. Sci. USA*, 10:53–55, 1924.
- R. W. Hamming. *Digital filters*. Prentice-Hall, New Jersey, 1989.
- F. J. Harris. On the use of windows for harmonic analysis with the discrete Fourier transform. *Proceedings of the IEEE*, 66:51–83, 1978.
- J. W. Harvey, F. Hill, R. P. Hubbard, J. R. Kennedy, J. W. Liebacher, J. A. Pinter, P. A. Gilman, R. W. Noyes, A. M. Title, J. Toomre, and R. K. Ulrich. The global oscillation network group (GONG) project. *Science*, 272:1284–1286, 1996.
- S. Haykin and D. J. Thomson. Signal detection in a nonstationary environment reformulated as an adaptive pattern classification problem. *Proceedings of the IEEE*, 86:2325–2344, 1998.
- H. M. Henning and P. H. Scherrer. The search for solar gravity modes. *Seismology of the Sun and Sun-Like Stars, ESA SP-286*, pages 419–423, 1988.
- L. J. Herbst. Periodogram analysis and variance fluctuation. *Journal of the Royal Statistical Society, Series B*, 25:442–450, 1963a.
- L. J. Herbst. A test for variance heterogeneity in the residuals of a Gaussian moving average. *Journal of the Royal Statistical Society, Series B*, 25:451–454, 1963b.
- L. J. Herbst. Almost periodic variances. *Annals of Mathematical Statistics*, 34:1549–1557, 1963c.

- G. M. Jenkins and D. G. Watts. *Spectral Analysis and its Applications*. Holden-Day, San Francisco, 1968.
- A. S. Kayhan, A. El-Jaroudi, and L. F. Chaparro. Evolutionary periodogram for nonstationary signals. *IEEE Transactions on Signal Processing*, 42(6):1527–1536, 1994.
- B. Klepser, M. Punzenberger, T. Rühlicke, and M. Zannoth. 5-Ghz and 2.4-Ghz dual-band RF-transceiver for WLAN 802.11a/b/g applications. *Radio Frequency Integrated Circuits Symposium*, pages 37–40, 2003.
- L. H. Koopmans. *The Spectral Analysis of Time Series*. Academic Press, New York, 1974.
- D. N. Lawley. Tests of significance for the latent roots of covariance and correlation matrices. *Biometrika*, 43:128–136, 1956.
- M. Loève. Fonctions aléatoires de second ordre. *Les Comptes Rendus de l'Académie des Sciences, Paris*, 222:942–944, 1946.
- A. Malekpour, T. C. Ling, and W. C. Lim. Location determination using radio frequency RSSI and deterministic algorithm. *Communication Networks and Services Research Conference*, pages 488–495, 2008.
- K. V. Mardia and P. E Jupp. *Directional Statistics*. John Wiley and Sons, London, England, 2000.
- W. Martin. Time-frequency analysis of random signals. *International Conference on Acoustics, Speech, and Signal Processing*, 7:1325–1328, 1982.
- G. Mélard. *Processus purement indéterminables à paramètre discret: Approches fréquentielle et temporelle*. PhD thesis, Université Libre de Bruxelles, 1975.

- G. Mélard and A. H. Schutter. Contributions to evolutionary spectral theory. *Journal of Time Series Analysis*, 10(1):41–63, 1989.
- K. S. Miller. Complex linear least squares. *SIAM Review*, 15(4):706–726, 1973.
- K. S. Miller. *Complex Stochastic Processes*. Addison Wesley, Reading, MA, 1974.
- W. H. Munk and K. Hasselmann. Super-resolution of tides. In K. Yoshida, editor, *Studies on Oceanography*, pages 339–344. Univ. of Tokyo Press, Tokyo, 1964.
- J. Pap, W. K. Tobiska, and S. D. Bouwer. Periodicities of solar irradiance and solar activity indices, I. *Solar Physics*, 129:165–189, 1990.
- E. Parzen. On consistent estimates of the spectrum of a stationary time series. *Annals of Mathematical Statistics*, 28:329–348, 1957.
- D. B. Percival and A. T. Walden. *Spectral Analysis for Physical Applications: Multitaper and Conventional Univariate Techniques*. Cambridge University Press, Cambridge, UK, 1993.
- J. W. Pitton. Linear and quadratic methods for positive time-frequency distributions. *International Conference on Acoustics, Speech, and Signal Processing*, 5:3649–3652, 1997.
- J. W. Pitton, P. J. Loughlin, and L. E. Atlas. Positive time-frequency distributions via maximum entropy deconvolution of the evolutionary spectrum. *International Conference on Acoustics, Speech, and Signal Processing*, 4:436–439, 1993.
- M. B. Priestley. Evolutionary spectrum and non-stationary processes. *Journal of the Royal Statistical Society, Series B*, 27(2):204–237, 1965.
- M. B. Priestley. *Spectral Analysis and Time Series*. Academic Press, London, England, 1981.

- M. B. Priestley. *Non-Linear and Non-Stationary Time Series Analysis*. Academic Press, London, England, 1988.
- D. H. Pritchard. Adjustable bandwidth optical filters, 1971. U.S. Patent 3,588,224.
- D. H. Pritchard. Stripe-color-encoded single-tube color-television camera system. *RCA Reviews*, 34:217–266, 1973.
- C. M. Rader. Recovery of undersampled periodic waveforms. *IEEE Transactions on Acoustics, Speech, and Signal Processing*, 25(3):242–249, 1977.
- F. L. Ramsey. Characterization of the partial autocorrelation function. *Annals of Statistics*, 2(6):1296–1301, 1974.
- Z. Ratsimalahelo. Rank test based on matrix perturbation theory. Technical Report 4, Economics and Econometrics Research Institute, Belgium, 2002.
- Jean-Marc Robin and R. J. Smith. Tests of rank. *Econometric Theory*, 16:151–175, 2000.
- O. E. Rögnvaldsson. Spectral estimation using the multiple-taper method. Technical Report RH-13-93, Science Institute: University of Iceland, 1993.
- R. B. Sanderson, J. B. Y. Tsui, and N. Freese. Reduction of aliasing ambiguities through phase relations. *IEEE Transactions on Aerospace and Electronic Systems*, 28(4):950–956, 1992.
- L. L. Scharf, B. Friedlander, and D. J. Thomson. Covariant estimators of time-frequency descriptors for nonstationary random processes. In *Proc. of the Thirty-Second Asilomar Conf. on Signals, Systems, and Computers*, pages 808–811, Madison, WI, 1998. Omnipress. IEEE Cat. No. 98CH36284.

- M. R. Schroeder. Direct (nonrecursive) relations between cepstrum and predictor coefficients. *IEEE Transactions on Acoustics, Speech, and Signal Processing*, 29(2):297–301, 1981.
- D. Slepian. Prolate spheroidal wave functions: Fourier analysis, and uncertainty. *Bell Systems Technical Journal*, 43:3009–3057, 1964.
- D. Slepian. Some asymptotic expansions for prolate spheroidal wave functions. *Journal of Mathematics and Physics*, 44:99–140, 1965.
- David Slepian. Prolate spheroidal wave functions, Fourier analysis, and uncertainty V: The discrete case. *Bell Systems Technical Journal*, 57:1371–1429, 1978.
- D. J. Thomson. Jackknifing multitaper spectrum estimates. *IEEE Signal Processing Magazine*, 24(7):20–30, 2007.
- D. J. Thomson. Spectrum estimation and harmonic analysis. *Proceedings of the IEEE*, 70:1055–1096, 1982.
- D. J. Thomson. Quadratic-inverse spectrum estimates: Applications to paleoclimatology. *Phil. Trans. R. Soc. Lond. A*, 332:539–597, 1990.
- D. J. Thomson. Non-stationary fluctuations in “stationary” time series. *Proc. SPIE*, 2027:236–244, 1993.
- D. J. Thomson. Multiple-window spectrum estimates for non-stationary data. In *Proc. Ninth IEEE SP Workshop on Statistical Signal and Array Processing*, pages 344–347, Portland, Oregon, 1998. IEEE.
- D. J. Thomson and A. D. Chave. Jackknifed error estimates for spectra, coherences, and transfer functions. In Simon Haykin, editor, *Advances in Spectrum Analysis and Array Processing*, volume 1, chapter 2, pages 58–113. Prentice-Hall, New Jersey, 1991.

- David J. Thomson. Multitaper analysis of nonstationary and nonlinear time series data. In W. Fitzgerald, R. Smith, A. Walden, and P. Young, editors, *Nonlinear and Nonstationary Signal Processing*, pages 317–394. Cambridge Univ. Press, London, England, 2000.
- D. Tjøstheim. Spectral generating operators for non-stationary processes. *Adv. Appl. Prob.*, 8:831–846, 1976.
- J. W. Tukey and R. W. Hamming. Measuring noise color. In D. R. Brillinger, editor, *The Collected Works of John W. Tukey Volume 1, Time Series: 1949-1964*, pages 1–127. Wadsworth, Belmont, CA, 1984.
- J. A. Ville. Théorie et applications de la notion de signal analytique. *Câbles et Transm.*, 2A:61–74, 1948.
- N. Wiener. *Extrapolation, Interpolation, and Smoothing of Stationary Time Series*. M.I.T. Press, Cambridge, MA, 1949.
- E. P. Wigner. On the quantum correction for thermodynamic equilibrium. *Physical Review*, 40(5):749–759, 1932.
- H. Wold. *A study in the analysis of stationary time series*. Almqvist and Wiksell, Stockholm, second edition, 1954.
- C. L. Wolff and J. R. Hickey. Solar irradiance change and special longitudes due to r -modes. *Science*, 235:1631–1633, 1987.
- L. Zadeh. Frequency analysis of variable networks. *Proc. IRE*, 38:291–299, 1950.

Appendix A

Prolate Spheroidal Wave Functions and Sequences

It was shown in [Slepian 1978] that the eigenfunctions of the Dirichlet kernel, known as prolate spheroidal wave functions, are fundamental in the study of time- and band-limited systems. In this appendix we collect the basic definitions and properties of prolate spheroidal wave functions and related functions.

For a fixed $N \in \mathbb{Z}_{>0}$, the (*uncentered*) *Dirichlet kernel* is the function $\mathcal{D}_N : \mathbb{R} \rightarrow \mathbb{C}$ defined by

$$\mathcal{D}_N(f) \triangleq \sum_{t=0}^{N-1} e^{-i2\pi ft} = \frac{\sin(N\pi f)}{\sin(\pi f)} e^{-i2\pi f \frac{N-1}{2}}. \quad (\text{A.1})$$

For convenience, we multiply the uncentered Dirichlet kernel by the function $e^{i2\pi f \frac{N-1}{2}}$ to center at zero and obtain the (*centered*) *Dirichlet kernel* which is a function $\mathcal{D}_N^{(c)} : \mathbb{R} \rightarrow \mathbb{R}$ and is defined by

$$\mathcal{D}_N^{(c)}(f) \triangleq \sum_{t=0}^{N-1} e^{-i2\pi f(t - \frac{N-1}{2})} = \frac{\sin(N\pi f)}{\sin(\pi f)}. \quad (\text{A.2})$$

For a fixed $0 < W < 1/2$, the *discrete prolate spheroidal wave functions* (DPSWFs)

$U_k(N, W; \cdot) \in \mathcal{L}^2([-1/2, 1/2]; \mathbb{R})$, $k \in \{0, 1, \dots, N-1\}$, are the solutions of the integral equation

$$\int_{-W}^W \mathcal{D}_N^{(c)}(f - f') U_k(N, W; f') df' = \lambda_k^{(c)}(N, W) U_k(N, W; f). \quad (\text{A.3})$$

In other words, the functions $U_k(N, W; \cdot)$ are eigenfunctions of the linear operator on $\mathcal{L}^2([-1/2, 1/2]; \mathbb{R})$ which maps $F \in \mathcal{L}^2([-1/2, 1/2]; \mathbb{R})$ to its convolution against $\mathcal{D}_N^{(c)}$ over $[-W, W]$. For more detail, see [Slepian 1964] and [Slepian 1965]. The associated eigenvalues $\lambda_k^{(c)}(N, W)$, $k \in \{0, 1, \dots, N-1\}$, have the following interpretation: The real number $\lambda_k^{(c)}(N, W)$ is the fraction of “energy” of $U_k(N, W; f)$ in the interval $[-W, W]$ relative to its total “energy” in $[-1/2, 1/2]$, *i.e.* $\int_{-W}^W |U_k(f)|^2 df / \int_{-1/2}^{1/2} |U_k(f)|^2 df$ where $U_k(f) \equiv U_k(N, W, f)$.

The eigenvalues are monotonically decreasing and are strictly bounded:

$$1 > \lambda_0^{(c)}(N, W) > \lambda_1^{(c)}(N, W) > \dots > \lambda_{N-1}^{(c)}(N, W) > 0.$$

A key property of the eigenvalues is that the first $\lfloor 2NW \rfloor - 1$ eigenvalues $\{\lambda_0^{(c)}(N, W), \lambda_1^{(c)}(N, W), \dots, \lambda_{\lfloor 2NW \rfloor - 1}^{(c)}(N, W)\}$, are approximately equal to 1.

The DPSWFs exhibit a *double orthogonality* property. In particular, they are orthogonal over $[-W, W]$:

$$\frac{1}{\lambda_k^{(c)}(N, W)} \int_{-W}^W U_j(N, W; f) U_k(N, W; f) df = \delta_{j,k}, \quad (\text{A.4})$$

and orthonormal over $[-1/2, 1/2]$:

$$\int_{-1/2}^{1/2} U_j(N, W; f) U_k(N, W; f) df = \delta_{j,k}. \quad (\text{A.5})$$

In the above, $\delta_{j,k}$ denotes the Kronecker delta function. The Fourier transforms of the

DPSWFs [Slepian 1978] are known as *discrete prolate spheroidal sequences* (DPSSs) and are defined by

$$\nu_t^{(k)}(N, W) \triangleq \frac{1}{\varepsilon_k \lambda_k^{(c)}(N, W)} \int_{-W}^W U_k(N, W; f) e^{-i2\pi f(t - \frac{N-1}{2})} df, \quad (\text{A.6})$$

where $k \in \{0, 1, \dots, N-1\}$ and $t \in \{0, 1, \dots, N-1\}$. (The above expression for $\nu_t^{(k)}(N, W)$ is in fact valid for all $t \in \mathbb{R}$, but we will not need this generality.) The complex number ε_k is defined to be 1 when k is even and i when k is odd. Because of the double orthogonality property of the DPSWFs, we can write equivalently

$$\nu_t^{(k)}(N, W) = \frac{1}{\varepsilon_k} \int_{-1/2}^{1/2} U_k(N, W; f) e^{-i2\pi f(t - \frac{N-1}{2})} df. \quad (\text{A.7})$$

The finite inverse Fourier transform of the DPSSs results in the following expression for the DPSWFs:

$$U_k(N, W; f) = \varepsilon_k \sum_{t=0}^{N-1} \nu_t^{(k)}(N, W) e^{i2\pi f(t - \frac{N-1}{2})}, \quad (\text{A.8})$$

where $k \in \{0, 1, \dots, N-1\}$. We can further see that the DPSWFs also satisfy $U_k(N, W; -f) = U_k(N, W; f)$ when k is even and $U_k(N, W; -f) = -U_k(N, W; f)$ when k is odd.

It can be shown that the DPSSs are the solutions of the Toeplitz matrix eigenproblem

$$\sum_{n=0}^{N-1} \frac{\sin(2\pi W(t-n))}{\pi(t-n)} \nu_n^{(k)}(N, W) = \lambda_k^{(c)}(N, W) \nu_t^{(k)}(N, W). \quad (\text{A.9})$$

The DPSSs also exhibit a double orthogonality property. In particular, they are

orthogonal over \mathbb{Z} so that

$$\lambda_k^{(c)}(N, W) \sum_{t=-\infty}^{\infty} \nu_t^{(j)}(N, W) \nu_t^{(k)}(N, W) = \delta_{j,k}, \quad (\text{A.10})$$

and orthonormal over $\{0, 1, \dots, N-1\}$ so that

$$\sum_{t=0}^{N-1} \nu_t^{(j)}(N, W) \nu_t^{(k)}(N, W) = \delta_{j,k}. \quad (\text{A.11})$$

If one begins instead with the *uncentered* Dirichlet kernel shown in Eq. (A.1), one arrives at complex-valued functions with similar properties to the DPSWFs. Specifically, for a fixed $0 < W < 1/2$, denote by $V_k(N, W; \cdot) \in \mathcal{L}^2([-1/2, 1/2]; \mathbb{C})$, $k \in \{0, 1, \dots, N-1\}$, the solutions of the integral equation

$$\int_{-W}^W \mathcal{D}_N(f - f') V_k(N, W; f') \, df' = \lambda_k(N, W) V_k(N, W; f). \quad (\text{A.12})$$

It can be shown that $\lambda_k(N, W) = \lambda_k^{(c)}(N, W)$ for all $k \in \{0, 1, \dots, N-1\}$. The functions $V_k(N, W; \cdot)$ have a double orthogonality property similar to the functions $U_k(N, W; \cdot)$. They are orthogonal over $[-W, W]$:

$$\frac{1}{\lambda_k(N, W)} \int_{-W}^W V_j(N, W; f) \overline{V_k(N, W; f)} \, df = \delta_{j,k}, \quad (\text{A.13})$$

and orthonormal over $[-1/2, 1/2]$:

$$\int_{-1/2}^{1/2} V_j(N, W; f) \overline{V_k(N, W; f)} \, df = \delta_{j,k}. \quad (\text{A.14})$$

In the above, the overline denotes complex conjugation. It can easily be seen that the functions $V_k(N, W; \cdot)$ satisfy $V_k(N, W; -f) = \overline{V_k(N, W; f)}$.

For $t \in \{0, 1, \dots, N-1\}$, the relationship between $V_k(N, W; \cdot)$ and $\nu_t^{(k)}(N, W)$ is

$$V_k(N, W; f) = \sum_{t=0}^{N-1} \nu_t^{(k)}(N, W) e^{-i2\pi ft}. \quad (\text{A.15})$$

Comparing Eqs. (A.8) and (A.15) gives the relationship between $U_k(N, W; \cdot)$ and $V_k(N, W; \cdot)$ as

$$V_k(N, W; f) = \varepsilon_k^{-1} e^{-i2\pi f \frac{N-1}{2}} U_k(N, W; -f), \quad (\text{A.16})$$

or equivalently

$$U_k(N, W; f) = \varepsilon_k e^{-i2\pi f \frac{N-1}{2}} V_k(N, W; -f). \quad (\text{A.17})$$

Substituting Eq. (A.17) into Eqs. (A.6) and (A.7) respectively, and recalling that $\lambda_k(N, W) = \lambda_k^{(c)}(N, W)$, one arrives at the following relationships:

$$\nu_t^{(k)}(N, W) = \frac{1}{\lambda_k(N, W)} \int_{-W}^W V_k(N, W; f) e^{i2\pi ft} df \quad (\text{A.18})$$

$$\nu_t^{(k)}(N, W) = \int_{-1/2}^{1/2} V_k(N, W; f) e^{i2\pi ft} df. \quad (\text{A.19})$$

Appendix B

Multiple-Window Spectrum

Estimation

Let $\mathbf{X}_c \triangleq \{X(t)\}_{t \in \mathbb{R}}$ be a continuous-time real-valued zero-mean stationary Gaussian stochastic process. We assume that \mathbf{X}_c is stationary, meaning that it has a Cramér or spectral representation [Cramér 1946] of the form

$$X(t) = \int_{\mathbb{R}} e^{i2\pi ft} dZ_{\mathbf{X}_c}(f), \quad \forall t \in \mathbb{R}, \quad (\text{B.1})$$

where $\{Z_{\mathbf{X}_c}(f)\}_{f \in \mathbb{R}}$ is an orthogonal-increment process associated to \mathbf{X}_c .

Now define a discrete-time real-valued zero-mean stationary Gaussian stochastic process $\mathbf{X} \triangleq \{X_t\}_{t \in \mathbb{Z}}$ by setting $X_t \triangleq X(t\Delta T)$, where $t \in \mathbb{Z}$ and $\Delta T \in \mathbb{R}_{>0}$ is some sampling interval. A similar spectral representation holds for \mathbf{X} ,

$$X_t = \int_{-\mathcal{F}_n}^{\mathcal{F}_n} e^{i2\pi ft} dZ_{\mathbf{X}}(f), \quad \forall t \in \mathbb{Z}, \quad (\text{B.2})$$

where $\mathcal{F}_n \triangleq 1/(2\Delta T)$ is the *Nyquist frequency* and $\{Z_{\mathbf{X}}(f)\}_{f \in [-\mathcal{F}_n, \mathcal{F}_n]}$ is an orthogonal-increment process associated to \mathbf{X} . The spectrum of \mathbf{X} is defined by the second

moment of $\{dZ_{\mathbf{X}}(f)\}$ as

$$S_{\mathbf{X}}(f) df = \mathbb{E}\{|dZ_{\mathbf{X}}(f)|^2\}. \quad (\text{B.3})$$

The relationship between $dZ_{\mathbf{X}_c}$ and $dZ_{\mathbf{X}}$ can be found in [Percival and Walden 1993]. For simplicity, we assume $\Delta T = 1$ and so the Nyquist frequency is $\mathcal{F}_n = 1/2$.

From Eq. (B.3) we see that estimating $S_{\mathbf{X}}$ is equivalent to estimating the second moment of $dZ_{\mathbf{X}}$. Assume we have a realization X_0, X_1, \dots, X_{N-1} of \mathbf{X} . To estimate the second moment of $dZ_{\mathbf{X}}$ from a finite realization of \mathbf{X} , Thomson [1982] suggested that we transform into the frequency domain by using the discrete Fourier transform of the given realization as:

$$G(f) = \sum_{t=0}^{N-1} X_t e^{-i2\pi ft}. \quad (\text{B.4})$$

Substituting Eq. (B.2) into Eq. (B.4) and applying Eq. (A.1), we get

$$G(f) = \int_{-1/2}^{1/2} \mathcal{D}_N(f - f') dZ_{\mathbf{X}}(f'), \quad (\text{B.5})$$

where in the above \mathcal{D}_N is the Dirichlet kernel (see Appendix A). The above equation is called the *fundamental equation of spectrum estimation* [Parzen 1957] and is a linear Fredholm integral equation of the first kind.

In order to estimate $dZ_{\mathbf{X}}$, Thomson [1982] suggested an approximate solution to the integral equation shown in Eq. (B.5) in a small frequency band $(f - W, f + W)$ where $0 < W < 1/2$, $W \ll 1/2$, is known as the *analysis bandwidth*. The *high-resolution estimate* of $dZ_{\mathbf{X}}$ [Thomson 1982], denoted $\widehat{dZ_{\mathbf{X}}}$, and valid for frequencies $\xi - W < f < \xi + W$ when $0 < \xi < 1/2$, is

$$\widehat{dZ_{\mathbf{X}}}(f; \xi) = \sum_{k=0}^{K-1} V_k(N, W; f - \xi) \frac{y_k(\xi)}{\lambda_k(N, W)}, \quad (\text{B.6})$$

where

$$y_k(f) \triangleq \sum_{t=0}^{N-1} X_t \nu_t^{(k)}(N, W) e^{-i2\pi ft} \quad (\text{B.7})$$

are the estimated Fourier-Bessel expansion coefficients or the *eigencoefficients*. In the above we choose $K = \lfloor 2NW \rfloor$ as this is the maximum number of DPSWFs whose energy is highly concentrated in the interval $[-W, W]$ (see Appendix A).

Corresponding to the high-resolution estimate of $dZ_{\mathbf{X}}$, there is a *high-resolution spectrum estimate* [Thomson 1982], valid for frequencies $\xi - W < f < \xi + W$ when $0 < \xi < 1/2$, defined by

$$\widehat{S}_{\mathbf{X}}(f; \xi) \triangleq \frac{1}{N} \left| \widehat{dZ}_{\mathbf{X}}(f; \xi) \right|^2 = \frac{1}{N} \left| \sum_{k=0}^{K-1} V_k(N, W; f - \xi) \frac{y_k(\xi)}{\lambda_k(N, W)} \right|^2. \quad (\text{B.8})$$

It can be seen that the high-resolution spectrum estimate is a sum of the square magnitude of a complex, approximately Gaussian random variable, and so is approximately distributed as χ_2^2 , and therefore is an inconsistent estimator [Thomson 1982]. To overcome the consistency problem, Thomson [1982] suggested averaging the high-resolution spectrum estimate over interior frequency bands $(\xi - W, \xi + W)$. Using the orthogonality property of the DPSWFs represented in Eq. (A.13), the *multiple-window spectrum estimate* or simply *multi-taper spectrum estimate* is derived as

$$\begin{aligned} \frac{1}{2W} \int_{\xi-W}^{\xi+W} \widehat{S}_{\mathbf{X}}(f; \xi) df &= \frac{1}{2NW} \sum_{k=0}^{K-1} \frac{1}{\lambda_k(N, W)} |y_k(\xi)|^2 \\ &\approx \frac{1}{K} \sum_{k=0}^{K-1} |y_k(\xi)|^2 \triangleq \widehat{S}_{\mathbf{X}}(\xi), \end{aligned} \quad (\text{B.9})$$

as $\lambda_k(N, W) \approx 1$ for $k = \{0, 1, \dots, \lfloor 2NW \rfloor\}$ (see Appendix A). The estimate shown in Eq. (B.9) is a sum of squares of K approximately uncorrelated Gaussian random variables, each with an approximately χ_2^2 distribution. Consequently, $\widehat{S}_{\mathbf{X}}$ is distributed

approximately as χ_{2K}^2 divided by K . This estimator is consistent, as for a fixed W , its distribution has approximately $4NW$ degrees of freedom [Thomson 1982].

Appendix C

Harmonic Analysis

Let $\mathcal{U}_c \triangleq \{\mathcal{U}(t)\}_{t \in \mathbb{R}}$ be a continuous-time real-valued process with a “mixed spectrum,” and let $W \in \mathbb{R}_{>0}$ be fixed. The assumption that \mathcal{U}_c has a mixed spectrum means that its spectrum is comprised of a finite number of harmonic (line) components superimposed on a continuous background spectrum. To be precise, we assume that for each $t \in \mathbb{R}$, $\mathcal{U}(t)$ has the form

$$\mathcal{U}(t) = \sum_{j=1}^J D_j \cos(2\pi g_j t + \theta_j) + \vartheta(t), \quad (\text{C.1})$$

where each $g_j, D_j, \theta_j \in \mathbb{R}$ and $\vartheta \triangleq \{\vartheta(t)\}_{t \in \mathbb{R}}$ is a continuous-time zero-mean stationary Gaussian process. We call g_j, D_j, θ_j the *frequency, amplitude, and phase of the j th line component* of \mathcal{U}_c , respectively. We assume that for each j , $|g_j| > W/2$ (this assumption will be used below). For each $t \in \mathbb{R}$, we can rewrite Eq. (C.1) as

$$\begin{aligned} \mathcal{U}(t) &= \sum_{j=1}^J \left[\frac{D_j}{2} e^{i(2\pi g_j t + \theta_j)} + \frac{D_j}{2} e^{-i(2\pi g_j t + \theta_j)} \right] + \vartheta(t) \\ &= \sum_{j=1}^J [\mu_j e^{i2\pi g_j t} + \overline{\mu_j} e^{-i2\pi g_j t}] + \vartheta(t), \end{aligned} \quad (\text{C.2})$$

where $\mu_j \triangleq (D_j e^{i\theta_j})/2$ for each j , and the overline denotes complex conjugation.

Let $\Delta T \in \mathbb{R}_{>0}$ be some sampling interval, and define the Nyquist frequency $\mathcal{F}_n \triangleq 1/(2\Delta T)$. Define a discrete-time process $\mathcal{U}_d \triangleq \{\mathcal{U}_t\}_{t \in \mathbb{Z}}$ by setting $\mathcal{U}_t \triangleq \mathcal{U}(t\Delta T)$, for each $t \in \mathbb{Z}$. Then for each $t \in \mathbb{Z}$, we can write \mathcal{U}_t as

$$\mathcal{U}_t = \sum_{j=1}^J [\mu_j e^{i2\pi g_j t \Delta T} + \overline{\mu_j} e^{-i2\pi g_j t \Delta T}] + \vartheta(t\Delta T). \quad (\text{C.3})$$

Since ϑ is zero-mean by assumption, the expected value of \mathcal{U}_t is

$$\mathbb{E}\{\mathcal{U}_t\} = \sum_{j=1}^J [\mu_j e^{i2\pi g_j t \Delta T} + \overline{\mu_j} e^{-i2\pi g_j t \Delta T}], \quad (\text{C.4})$$

so that $\mathcal{U}_t = \mathbb{E}\{\mathcal{U}_t\} + \vartheta(t\Delta T)$ for each $t \in \mathbb{Z}$. For simplicity we assume $\Delta T = 1$, so the Nyquist frequency is $\mathcal{F}_n = 1/2$. Now, let $\mathcal{U}_0, \mathcal{U}_1, \dots, \mathcal{U}_{N-1}$ be a realization of \mathcal{U}_d of length N . The k th eigencoefficient of \mathcal{U}_d with bandwidth W (see Appendix B, Eq. (B.7)), evaluated at $f \in [-1/2, 1/2)$, is then

$$\begin{aligned} y_k(\mathcal{U}_d; f) &= \sum_{t=0}^{N-1} \mathcal{U}_t \nu_t^{(k)}(N, W) e^{-i2\pi f t} \\ &= \sum_{t=0}^{N-1} [\mathbb{E}\{\mathcal{U}_t\} + \vartheta(t)] \nu_t^{(k)}(N, W) e^{-i2\pi f t} \\ &= \sum_{t=0}^{N-1} \mathbb{E}\{\mathcal{U}_t\} \nu_t^{(k)}(N, W) e^{-i2\pi f t} + \tilde{\vartheta}_k(f), \end{aligned} \quad (\text{C.5})$$

where we have defined

$$\tilde{\vartheta}_k(f) \triangleq \sum_{t=0}^{N-1} \vartheta(t) \nu_t^{(k)}(N, W) e^{-i2\pi f t}. \quad (\text{C.6})$$

Substituting the expression for $\mathbf{E}\{\mathcal{U}_t\}$ from Eq. (C.4) into Eq. (C.5) yields

$$\begin{aligned} y_k(\mathcal{U}_d; f) &= \sum_{t=0}^{N-1} \left(\sum_{j=1}^J [\mu_j e^{i2\pi g_j t} + \overline{\mu}_j e^{-i2\pi g_j t}] \right) \nu_t^{(k)}(N, W) e^{-i2\pi f t} + \tilde{\vartheta}_k(f) \\ &= \sum_{j=1}^J \mu_j V_k(N, W; f - g_j) + \overline{\mu}_j V_k(N, W; f + g_j) + \tilde{\vartheta}_k(f), \end{aligned} \quad (\text{C.7})$$

where $V_k(N, W; f)$ denotes the discrete-time Fourier transform of the k th Slepian sequence $\nu_t^{(k)}(N, W)$, evaluated at $f \in [-1/2, 1/2]$ (see Appendix A, Eq. (A.15)).

For the sake of illustration, we assume that $J = 1$; in other words, we assume that \mathcal{U}_c possesses one and only one line component. As a result, we have

$$y_k(\mathcal{U}_d; f) = \mu_1 V_k(N, W; f - g_1) + \overline{\mu}_1 V_k(N, W; f + g_1) + \tilde{\vartheta}_k(f). \quad (\text{C.8})$$

When $f = g_1$, Eq. (C.8) becomes

$$y_k(\mathcal{U}_d; g_1) = \mu_1 V_k(N, W; 0) + \overline{\mu}_1 V_k(N, W; 2g_1) + \tilde{\vartheta}_k(g_1). \quad (\text{C.9})$$

We note that for each k , $V_k(N, W; f) \approx 0$ for all $|f| > W$, since $V_k(N, W; \cdot)$ is highly concentrated in the interval $(-W, W)$ [Thomson 1982]. Since $|g_1| > W/2$ by assumption, we have

$$y_k(\mathcal{U}_d; g_1) \approx \mu_1 V_k(N, W; 0) + \tilde{\vartheta}_k(g_1). \quad (\text{C.10})$$

Since $\boldsymbol{\vartheta}$ is zero-mean stationary Gaussian, $\tilde{\vartheta}_k(f)$ will have a zero-mean complex Gaussian distribution for each k and f , say with a total variance of $\sigma_{\tilde{\vartheta}}^2$. We assume that the real and imaginary parts of $\tilde{\vartheta}_k(f)$ are uncorrelated Gaussian random variables and have equal semi-variances $\sigma_{\tilde{\vartheta}}^2/2$ [Percival and Walden 1993]. Due to the orthonormality of the Slepian sequences and assuming that $\boldsymbol{\vartheta}$ is locally white [Thomson 1982], the $\tilde{\vartheta}_k(f)$ are approximately pairwise uncorrelated for each fixed f . It follows from

Eqs. (C.10) and (A.15) that

$$\mathbb{E}\{y_k(\mathcal{U}_d; g_1)\} \approx \mu_1 V_k(N, W; 0) = \mu_1 \sum_{t=0}^{N-1} \nu_t^{(k)}(N, W) \quad (\text{C.11})$$

and

$$\text{Var}\{y_k(\mathcal{U}_d; g_1)\} = \mathbb{E}\{|y_k(\mathcal{U}_d; g_1)|^2\} - |\mathbb{E}\{y_k(\mathcal{U}_d; g_1)\}|^2 \approx \sigma_{\vartheta}^2. \quad (\text{C.12})$$

Supposing that we have chosen $K \leq \lfloor 2NW \rfloor$ (see Appendix B), we can now estimate μ_1 by complex linear least-squares, *i.e.*, by finding $\hat{\mu}_1$ that minimizes the sum of squares

$$\text{SS}(N, W, K; \hat{\mu}_1) \triangleq \sum_{k=0}^{K-1} |y_k(\mathcal{U}_d; g_1) - \hat{\mu}_1 V_k(N, W; 0)|^2. \quad (\text{C.13})$$

The minimizing value is given by

$$\begin{aligned} \hat{\mu}_1 &= \frac{\sum_{k=0}^{K-1} y_k(\mathcal{U}_d; g_1) V_k(N, W; 0)}{\sum_{k=0}^{K-1} V_k^2(N, W; 0)} \\ &= \frac{\sum_{k=0,2,\dots}^{K-1} y_k(\mathcal{U}_d; g_1) V_k(N, W; 0)}{\sum_{k=0,2,\dots}^{K-1} V_k^2(N, W; 0)}. \end{aligned} \quad (\text{C.14})$$

By Theorem 8.1 in [Miller 1973], we have the following four results. First, $\hat{\mu}_1$ is a random variable with a complex Gaussian distribution; using Eqs. (C.11), (C.12) and Eq. (C.14) we have (after some manipulations)

$$\mathbb{E}\{\hat{\mu}_1\} = \mu_1, \quad (\text{C.15})$$

$$\text{Var}\{\hat{\mu}_1\} = \frac{\sigma_{\vartheta}^2}{\sum_{k=0}^{K-1} V_k^2(N, W; 0)}. \quad (\text{C.16})$$

Second, an estimator of σ_{ϑ}^2 is given by

$$\widehat{\sigma_{\vartheta}^2} \triangleq \frac{1}{K-1} \sum_{k=0}^{K-1} |y_k(\mathcal{U}_d; g_1) - y_k^*(\mathcal{U}_d; g_1)|^2,$$

where

$$y_k^*(\mathcal{U}_d; g_1) \triangleq \widehat{\mu}_1 V_k(N, W; 0).$$

Third,

$$\frac{(2K-2)\widehat{\sigma_{\vartheta}^2}}{\sigma_{\vartheta}^2} \stackrel{\text{dist}}{=} \chi_{2K-2}^2, \quad (\text{C.17})$$

where the symbol “ $\stackrel{\text{dist}}{=}$ ” means “is distributed as.” Finally, $\widehat{\mu}_1$ and $(2K-2)\widehat{\sigma_{\vartheta}^2}/\sigma_{\vartheta}^2$ are independent.

Thomson [1982] proposed a hypothesis test for the presence of a line component in \mathcal{U}_c at a given frequency g_1 , under the null hypothesis $H_0 : \mu_1 = 0$. Under H_0 , $\widehat{\mu}_1$ is zero-mean and its variance is given in Eq. (C.16). Furthermore, under H_0 , $y_k(\mathcal{U}_d; g_1) = \widetilde{v}_k(g_1)$ and (using our earlier assumptions about the variance of $\widetilde{v}_k(f)$) the real and imaginary parts of $\widehat{\mu}_1$ are uncorrelated and have equal variance. Since $|\widehat{\mu}_1|^2$ is the sum of the squares of two uncorrelated random variables with equal variances (*i.e.*, the real and imaginary parts of $\widehat{\mu}_1$), we have

$$\frac{2|\widehat{\mu}_1|^2 \sum_{k=0}^{K-1} V_k^2(N, W; 0)}{\sigma_{\vartheta}^2} \stackrel{\text{dist}}{=} \chi_2^2. \quad (\text{C.18})$$

Since $\widehat{\mu}_1$ and $(2K-2)\widehat{\sigma_{\vartheta}^2}/\sigma_{\vartheta}^2$ are independent, it follows that $2|\widehat{\mu}_1|^2 \sum_{k=0}^{K-1} V_k^2(N, W; 0)/\sigma_{\vartheta}^2$ and $(2K-2)\widehat{\sigma_{\vartheta}^2}/\sigma_{\vartheta}^2$ are independent. The quotient $\frac{P/d_P}{Q/d_Q}$ of two independent random variables P, Q distributed as χ^2 with d_P and d_Q degrees of freedom, respectively, has

an F -distribution with (p, q) degrees of freedom. Thus, we have

$$\frac{(K-1)|\widehat{\mu}_1|^2 \sum_{k=0}^{K-1} V_k^2(N, W; 0)}{\sum_{k=0}^{K-1} |y_k(\mathcal{U}_d; g_1) - \widehat{y}_k(\mathcal{U}_d; g_1)|^2} \stackrel{\text{dist}}{=} F_{2, 2K-2}. \quad (\text{C.19})$$

This quotient, known as the F -variance ratio, can be thought of as representing the ratio of the power “explained” by the (hypothetical) line component at frequency g_1 to the power of the background spectrum, with contributions from the (hypothetical) line component at frequency g_1 “subtracted.”

Appendix D

Coherence Analysis

Let $\mathbf{X} \triangleq \{X_t\}_{t \in \mathbb{Z}}$ and $\mathbf{Y} \triangleq \{Y_t\}_{t \in \mathbb{Z}}$ be two stationary discrete-time real-valued processes. The *coherence* between \mathbf{X} and \mathbf{Y} is the complex-valued function of frequency defined by

$$C_{\mathbf{XY}}(f) = \frac{S_{\mathbf{XY}}(f)}{\sqrt{S_{\mathbf{X}}(f)}\sqrt{S_{\mathbf{Y}}(f)}}, \quad (\text{D.1})$$

where $S_{\mathbf{X}}$ and $S_{\mathbf{Y}}$ are the spectra of \mathbf{X} and \mathbf{Y} , respectively, and $S_{\mathbf{XY}}$ is the cross-spectrum between \mathbf{X} and \mathbf{Y} . The function $S_{\mathbf{X}}$ is also referred to as the *autospectrum* of \mathbf{X} , to sharpen the distinction between cross-spectra and spectra. A related quantity is the *magnitude-squared coherence* (MSC) between \mathbf{X} and \mathbf{Y} , which we denote by $\gamma_{\mathbf{XY}}$. As its name suggests, the MSC between \mathbf{X} and \mathbf{Y} is defined as $\gamma_{\mathbf{XY}}(f) \triangleq |C_{\mathbf{XY}}(f)|^2$, and is clearly nonnegative and bounded above by unity as a consequence of the Cauchy-Schwarz inequality.

In most practical situations, *e.g.*, situations involving physical systems, complete analytical knowledge of the autospectra and cross-spectrum appearing in Eq. (D.1) is unavailable. To compute the coherence between two processes \mathbf{X} and \mathbf{Y} , it must necessarily be estimated from finite realizations of \mathbf{X} and \mathbf{Y} .

Let X_0, X_1, \dots, X_{N-1} and Y_0, Y_1, \dots, Y_{N-1} be realizations of \mathbf{X} and \mathbf{Y} of length N .

Given realizations of \mathbf{X} and \mathbf{Y} as above, the multitaper estimate of the autospectrum of \mathbf{X} (see Appendix B) is given by

$$\widehat{S}_{\mathbf{X}}(f) = \frac{1}{K} \sum_{k=0}^{K-1} y_k(f; \mathbf{X}) \overline{y_k(f; \mathbf{X})}, \quad (\text{D.2})$$

where the overline denotes complex conjugation and $y_k(f; \mathbf{X})$ is the k th eigencoefficient of \mathbf{X} (see Appendix B, Eq. (B.7)).

Analogously, a multitaper estimate of the cross-spectrum of \mathbf{X} and \mathbf{Y} is given by

$$\widehat{S}_{\mathbf{XY}}(f) = \frac{1}{K} \sum_{k=0}^{K-1} y_k(f; \mathbf{X}) \overline{y_k(f; \mathbf{Y})}, \quad (\text{D.3})$$

where $y_k(f; \mathbf{X})$ and $y_k(f; \mathbf{Y})$ are the eigencoefficients of \mathbf{X} and \mathbf{Y} , respectively.

Substituting the multitaper estimators of the spectra and cross-spectrum from Eqs. (D.2) and (D.3) into Eq. (D.1), we obtain a multitaper estimate of complex coherence, $C_{\mathbf{XY}}$, which we denote by $\widehat{C}_{\mathbf{XY}}$:

$$\widehat{C}_{\mathbf{XY}}(f) \triangleq \frac{\sum_{k=0}^{K-1} y_k(f; \mathbf{X}) \overline{y_k(f; \mathbf{Y})}}{\sqrt{\sum_{k=0}^{K-1} |y_k(f; \mathbf{X})|^2} \sqrt{\sum_{k=0}^{K-1} |y_k(f; \mathbf{Y})|^2}}. \quad (\text{D.4})$$

Similarly, a multitaper MSC estimate is $\widehat{\gamma}_{\mathbf{XY}}(f) = |\widehat{C}_{\mathbf{XY}}(f)|^2$.

The coherence estimate from above can be jackknifed to obtain an estimator with improved bias properties. Recall that the jackknife is a general procedure, where minimal distributional assumptions are necessary, to reduce the bias of an arbitrary point estimator to $O(1/K^2)$, where K is the length of an independent sample. Furthermore, the jackknife allows one to nonparametrically estimate the variance of the estimator. For a general reference, see [Efron 1982]. For applications of the jackknife to multitaper estimates of spectra and coherences, see [Thomson and Chave 1991].

The jackknifed multitaper coherence estimate between \mathbf{X} and \mathbf{Y} is given by

$$\tilde{C}_{\mathbf{XY}}(f) \triangleq K\hat{C}(f) - \frac{K-1}{K} \sum_{\iota=0}^{K-1} \hat{C}_{\setminus\iota}(f), \quad (\text{D.5})$$

where $\hat{C}_{\setminus\iota}$, $0 \leq \iota \leq K-1$ are the “leave-one-out” multitaper coherence estimates

$$\hat{C}_{\setminus\iota}(f) = \frac{\sum_{\substack{k=0 \\ k \neq \iota}}^{K-1} y_k(f; \mathbf{X}) \overline{y_k(f; \mathbf{Y})}}{\sqrt{\sum_{\substack{k=0 \\ k \neq \iota}}^{K-1} |y_k(f; \mathbf{X})|^2} \sqrt{\sum_{\substack{k=0 \\ k \neq \iota}}^{K-1} |y_k(f; \mathbf{Y})|^2}}.$$

At this point, it should be noted that jackknifed estimators are known to suffer from inflated variance. This problem can be redressed, in general, by subjecting a jackknifed estimator to certain stabilizing transformations. Various types of transformations have been applied to the magnitude or magnitude-square of sample coherence estimates in the time series literature (see [Thomson and Chave 1991] for an overview). The transformation that interests us here is the inverse-hyperbolic tangent transformation used in [Koopmans 1974],

$$Q_{\setminus\iota} \triangleq \sqrt{2K-2} \tanh^{-1}(|\hat{C}_{\setminus\iota}(f)|), \quad (\text{D.6})$$

where K is now interpreted as the number of independent samples and $0 \leq \iota \leq K-1$. The transformation in Eq. (D.6) converts the distribution of magnitude-squared coherence estimates to be approximately Gaussian, with unit variance and mean given by $\mathbb{E}\{Q_{\setminus\iota}\} = \sqrt{2K-2} \tanh^{-1}(|C_{\mathbf{XY}}(f)|) + (1/\sqrt{2K-2})$ (see [Thomson and Chave 1991] and [Koopmans 1974] for more detail).

In order to estimate the phase of the jackknifed multitaper coherence, the specific approach used in this thesis is to first compute the *phase factors* defined by $e_{\setminus\iota}(f) =$

$\widehat{C}_{\setminus \iota}(f)/|\widehat{C}_{\setminus \iota}(f)|$, for $0 \leq \iota \leq K - 1$. We define the *jackknifed multitaper phase* of coherence estimate at frequency f to be

$$\widehat{\varphi}_{\setminus \cdot}(f) \triangleq \text{phase}\{e_{\setminus \cdot}(f)\}, \quad (\text{D.7})$$

where $e_{\setminus \cdot}(f) = (1/K) \sum_{l=0}^{K-1} e_{\setminus l}(f)$ is the arithmetic average of the $e_{\setminus l}$ at frequency f . The jackknifed estimate of the variance of $\widehat{\varphi}_{\setminus \cdot}(f)$ is then given by

$$\sigma_{\widehat{\varphi}}^2 = 2(K - 1)(1 - |e_{\setminus \cdot}(f)|). \quad (\text{D.8})$$

Further information regarding the jackknifed multitaper phase estimate can be found in [Thomson and Chave 1991] or [Mardia and Jupp 2000].